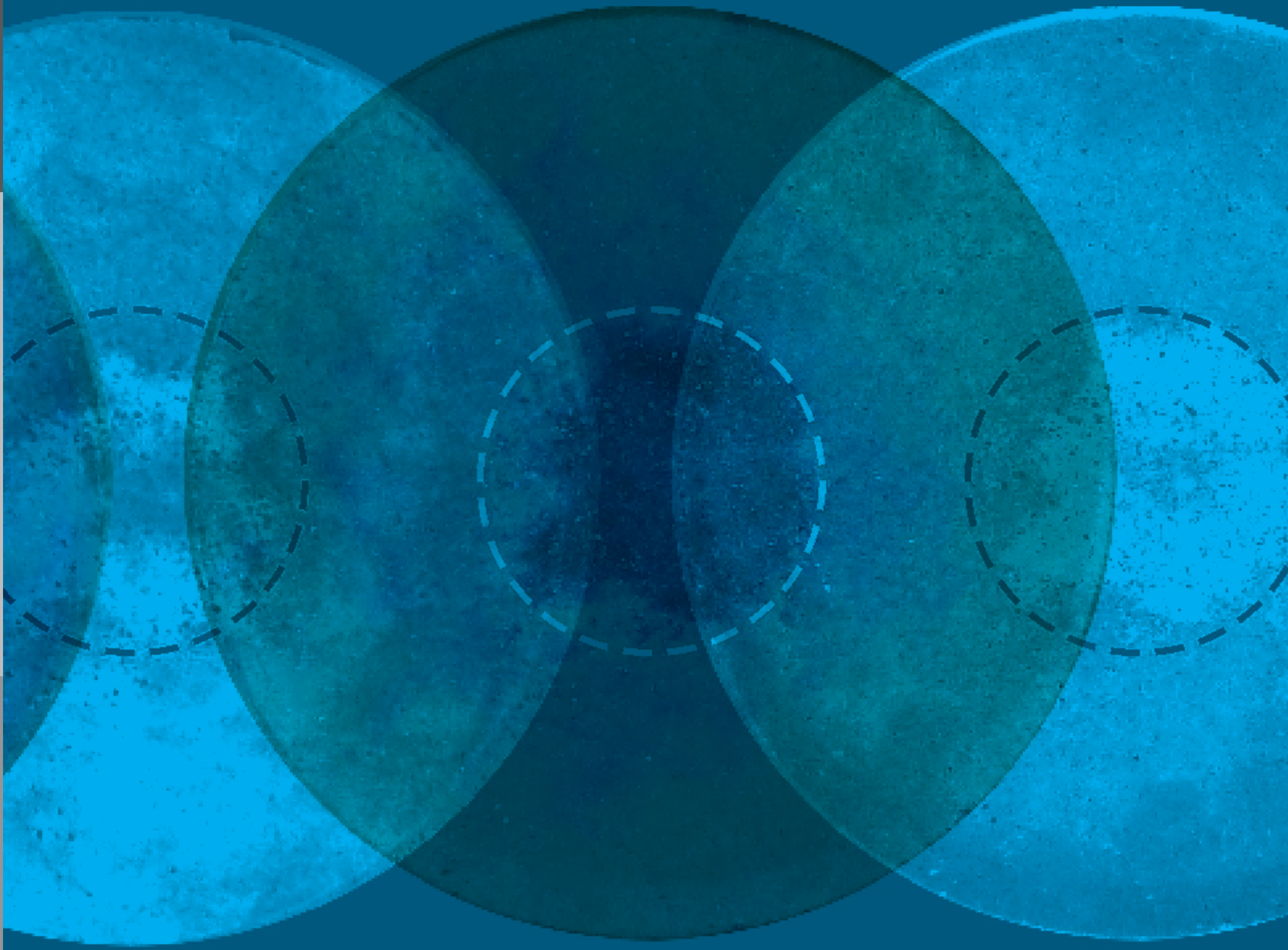

Experimental and numerical studies on solute transport in unsaturated heterogeneous porous media under evaporation conditions

Michel Bechtold

JÜLICH
FORSCHUNGSZENTRUM

Member of the Helmholtz Association

Rheinische
Friedrich-Wilhelms-
Universität Bonn

Mathematisch-
Naturwissenschaftliche
Fakultät

FORSCHUNGSZENTRUM
IBG-3 Agrosphäre

Experimental and numerical studies on solute transport in unsaturated heterogeneous porous media under evaporation conditions

Dissertation

zur

zur Erlangung des Doktorgrades (Dr. rer. nat.)

der

Mathematisch-Naturwissenschaftlichen Fakultät

der

Rheinischen Friedrich-Wilhelms-Universität Bonn

vorgelegt von

Diplom-Geowissenschaftler Michel Bechtold

aus Groß-Gerau

2011

Angefertigt mit Genehmigung
der Mathematisch-Naturwissenschaftlichen Fakultät
der Rheinischen Friedrich-Wilhelms-Universität Bonn

1. Gutachter: Prof. Dr. Harry Vereecken
2. Gutachter: Prof. Dr. Barbara Reichert
3. Kommissionsmitglied: Prof. Dr. Bernd Diekkrüger
4. Kommissionsmitglied: Prof. Dr. Tissa H. Illangasekare
Tag der Promotion: 7. Mai 2012
Erscheinungsjahr: 2012

Schriften des Forschungszentrums Jülich
Reihe Energie & Umwelt / Energy & Environment Band / Volume 143

Forschungszentrum Jülich GmbH
Institute of Bio- and Geosciences (IBG)
Agrosphere (IBG-3)

Experimental and numerical studies on solute transport in unsaturated heterogeneous porous media under evaporation conditions

Michel Bechtold

Schriften des Forschungszentrums Jülich
Reihe Energie & Umwelt / Energy & Environment Band / Volume 143

ISSN 1866-1793 ISBN 978-3-89336-795-5

Bibliographic information published by the Deutsche Nationalbibliothek.
The Deutsche Nationalbibliothek lists this publication in the Deutsche Nationalbibliografie; detailed bibliographic data are available in the Internet at http://dnb.d-nb.de.

Publisher and Distributor:	Forschungszentrum Jülich GmbH Zentralbibliothek 52425 Jülich Phone +49 (0) 24 61 61-53 68 · Fax +49 (0) 24 61 61-61 03 e-mail: zb-publikation@fz-juelich.de Internet: http://www.fz-juelich.de/zb
Cover Design:	Grafische Medien, Forschungszentrum Jülich GmbH
Printer:	Grafische Medien, Forschungszentrum Jülich GmbH
Copyright:	Forschungszentrum Jülich 2012

Schriften des Forschungszentrums Jülich
Reihe Energie & Umwelt / Energy & Environment Band / Volume 143

D 5N (Diss., Bonn, Univ., 2012)

ISSN 1866-1793
ISBN 978-3-89336-795-5

The complete volume is freely available on the Internet on the Jülicher Open Access Server (JUWEL) at http://www.fz-juelich.de/zb/juwel

Paciencia para la ciencia.

Spanish phrase

Acknowledgements

I sincerely thank Prof. Dr. H. Vereecken, director of the Agrosphere Institute at the Forschungszentrum Jülich and first examiner of the thesis, for his manifold support and constant encouragement throughout the course of this work.

I wish to thank Prof. Dr. B. Reichert, professor for hydrogeology at the University of Bonn, for her interest in my work and her contribution as a second examiner of the thesis.

I also wish to thank Prof. Dr. B. Diekkrüger and Prof. Dr. T. H. Illangasekare for serving on my PhD committee.

I would like to express my sincere gratitude to my direct mentor Prof. Dr. J. Vanderborght for teaching me scientific practice and for supporting my work with his profound knowledge and brilliant ideas.

Designing and constructing a complex experimental setup is a lot of fun and heavy burden. I am glad that I could share both with my colleagues at the Agrosphere Institute. I am very grateful to Dr. L. Weihermüller for providing me with many ideas when designing the experimental setup and for his constant scientific advice, and to Dr. M. Herbst and Dr. R. Kasteel for several helpful suggestions and discussions. I highly appreciate the great technical support that I received from N. Hermes, A. Weuthen, J. Höltkemeier, F. Engels, H. Rützel, T. Schuster, J. Heidbüchel, A. Langen and in particular R. Schröder. I gratefully acknowledge O. Esser, S. Bartsch and many more for their help during the packing of the laboratory soil.

I wish to thank Dr. O. Ippisch, University of Heidelberg, for his scientific advice and making his finite-volume code available, and Dr. T. Günther, LIAG Hannover, for his constant support and sharing his enthusiasm for ERT with me.

I would like to express my thanks to Dr. S. Haber-Pohlmeier and Dr. A. Pohlmeier for the exciting collaboration in the course of the MRI experiments.

I am very grateful to Dr. J. A. Huisman for the stimulating scientific advice and the interesting collaboration during the analysis of the technical issue of the TDR100. I wish to thank Dr. E. Zimmermann for assistance with the oscilloscope analysis.

I wish to thank Dr. M. Javaux for providing the MATLAB library for convection-dispersion analytical solutions (CASlib), Dr. J. Koestel for making his MATLAB code for the ERT error estimation available, and H. Hardelauf for programming support and coupling PARTRACE with the finite-volume flow model. I am grateful to the PhD students of the Agrosphere Institute, in particular Dr. S. Garré and Dr. J. Koestel, for constantly sharing the everyday problems at work.

I would like to express my sincere gratitude to Prof. Dr. T. P. A. Ferré, University of Arizona, for his hospitality, the inspiring scientific collaboration and an unforgettable research stay at the Department of Hydrology and Water Resources.

I wish to thank C. Kikuchi and Dr. D. C. Tanner for improving english wording.

I acknowledge the network EOS (www.netzwerk-eos.dlr.de) for funding the PhD project and the DAAD for funding my research stay at the University of Arizona.

Finally, I wish to thank my family and my friends for all their confidence and patience, which has been vital for the success of this thesis.

Contents

List of Figures

List of Tables

List of symbols and abbreviations

a	(Ω)	Absolute component of transfer resistance error
A	(L^{2})	Area of laboratory soil surface
A_c	(L^{2})	Area of a side of a material cube
α	(L^{-1})	Van Genuchten-Mualem shape parameter
α_L	(L)	Longitudinal dispersivity
α_T	(L)	Transversal dispersivity
b	(-)	Relative component of transfer resistance error
β	(-)	Probability that a particle reaches the element interface
$\mathbf{B}$	(L T$^{-0.5}$)	Dispersion displacement matrix
c	(m s^{-1})	Speed of light (3×10^{8} m s^{-1})
C	(M L^{-3})	Solute concentration in water
C_{pol}	(F)	Capacitance associated with electrode polarization
$\mathbf{d}$	(-)	Data vector of log-transformed apparent resistivities
$\mathbf{D}$	(L^{2} T^{-1})	Dispersion tensor
D_{app}	(L^{2} T^{-1})	Apparent dispersion coefficient
D_L	(L^{2} T^{-1})	Apparent longitudinal macrodispersion
D_m	(L^{2} T^{-1})	Effective molecular diffusion coefficient
$D_{m,w}$	(L^{2} T^{-1})	Molecular diffusion coefficient in water
E_a	(L T^{-1})	Actual evaporation rate
$E_{a,tot}$	(L T^{-1})	Total measured evaporation rate
$E_{fine+medium}$	(L T^{-1})	Actual evaporation rate from fine and medium material
ΔE_{osm}	(L T^{-1})	Decrease of evaporation rate due to osmotic potential
E_{pot}	(L T^{-1})	Potential evaporation rate
E_{wat}	(L T^{-1})	Evaporation rate from open water
ε	(-)	Total relative error of transfer resistance measurment
ε_0	(F m^{-1})	Eielectric permittivity of free space (8.854×10^{-12} F m^{-1})
f_{coarse}	(-)	Mass fraction in coarse material
f_{in}	(-)	Molar fraction of water vapor in the inflow air
f_{out}	(-)	Molar fraction of water vapor in the outflow air
f_{ret}	(-)	Retardation factor
$F_{Archie,app}$	(-)	Apparent Archie formation factor
$F_{Archie,material}$	(-)	Material Archie formation factor
γ	(T)	Time constant of a resistor and capacitor in series
G	(L)	Geometric factor
h	(L)	Pressure head
h_{osm}	(L)	Osmotic potential
J_{Hc}	(W m^{-2})	Soil heat flux

J_{lat}	(W m^{-2})	Latent heat flux
J_s	(m^{-2} d^{-1})	Normalized solute flux
k	(-)	Grid refinement factor
K	(L T^{-1})	Hydraulic conductivity
K_p	(L^{-1})	TDR probe constant
K_s	(L T^{-1})	Saturated hydraulic conductivity
κ	(W m^{-1} K^{-1})	Thermal conductivity of the porous medium
l_C	(L)	Cable length of TDR probe
L_p	(L)	Length of TDR probe wires
λ	(-)	Regularization factor in ERT inversion
λ_v	(MJ kg^{-1})	Latent heat of vaporization (2.45 MJ kg^{-1} at 20 °C)
m	(kg)	Mass
m_{par}	(kg)	Particle mass
$\mathbf{m}$	(-)	Model vector in ERT inversion
M_0	(kg)	Zeroth spatial moment, total solute mass
M_x	(L)	First spatial moment, position of center of mass in x-direction
M_{xx}	(L^2)	Second spatial moment, spread of solute mass in x-direction
μ_0	(H m^{-1})	Magnetic permeability of free space ($4\pi \times 10^{-7}$ H m^{-1})
n	(-)	Van Genuchten-Mualem shape parameter
n_{Archie}	(-)	Archie saturation exponent
n_{par}	(-)	Number of particles
$\varPhi$	(-)	Objective function of smoothness constraint ERT inversion
h_{osm}	(L)	Osmotic potential
p_{ch}	(Pa)	Total pressure in the evaporation chamber
P	(-)	Two-sided reflection coefficient
P_{new}	(-)	One-sided reflection coefficient
Q_{air}	(m^3 d^{-1})	Air flow rate through the evaporation chamber
r	(L)	Radius of the TDR probe wire
r_a	(T L^{-1})	Aerodynamic resistance
rH	(-)	Relative humidity
R	(Ω)	Electrical transfer resistance
R_g	(J K^{-1} mol^1)	Gas constant of air(8.314 J K^{-1} mol^1)
R_v	(L K^{-1})	Gas constant of water vapor (4697 cm K^{-1})
R_C	(Ω m^{-1})	Cable resistance
R_L	(Ω)	Load resistance
R_{out}	(Ω)	Output resistance
R_0	(Ω)	Additional series resistance
ρ_{infty}	(-)	TDR reflection coefficient at long times
ρ_b	(g cm^{-3})	Bulk density
ρ_{corr}	(-)	Corrected TDR reflection coefficient
ρ_{open}	(-)	TDR reflection coefficient of an open-circuit measurement
ρ_{vs}	(g cm^{-3})	Saturated water vapor density
ρ_w	(g cm^{-3})	Density of water
s	(L)	Spacing between TDR probe wires
S	(-)	Water saturation of the pore space
S/S_0	(-)	MRI signal intensity
$Surf$	(L^{-2} T^{-1})	Solute flux scaled that leaching surface integrates to unity
σ	(S m^{-1})	Electrical conductivity
σ_0	(S m^{-1})	Background water electrical conductivity

$\sigma_{25°\mathrm{C}}$	(S m^{-1})	Electrical conductivity at 25 °C
σ_b	(S m^{-1})	Bulk electrical conductivity
σ_w	(S m^{-1})	Water electrical conductivity
t	(T)	Time
t_E	(T)	Echo time
t_R	(T)	Repetition time
Δt	(T)	Time step
T	(K)	Temperature
T_{ch}	(K)	Temperature in the evaporation chamber
T_{in}	(K)	Temperature of inflow air
T_{out}	(K)	Temperature of outflow air
T_{surf}	(K)	Temperature at the soil surface
T_1	(T)	Longitudinal relaxation time
θ	(L^3 L^{-3})	Volumetric water content
θ_r	(L^3 L^{-3})	Residual volumetric water content
θ_s	(L^3 L^{-3})	Saturated volumetric water content
τ	(-)	Van Genuchten-Mualem shape parameter
$\mathbf{u}$	(L T^{-1})	Pore water velocity vector
u_{app}	(L T^{-1})	Local apparent velocity
$u_{app,exp}$	(L T^{-1})	Experimental local apparent velocity
$u_{app,mod}$	(L T^{-1})	Modeled local apparent velocity
u_x	(L T^{-1})	Pore water velocity in x-direction
u_y	(L T^{-1})	Pore water velocity in y-direction
u_z	(L T^{-1})	Pore water velocity in z-direction
U	(L T^{-1})	Apparent average velocity
v_p	(L T^{-1})	Relative propagation velocity of electromagnetic waves
V	(L^3)	Volume
V_c	(L^3)	Volume of a material cube
V_m^w	(m^3 mol^{-1})	Molar volume of liquid water
$\mathbf{W_d}$	(-)	Data weighting matrix
$\mathbf{W_s}$	(-)	Smoothness constraint operator
$\mathbf{X}$	(L)	Coordinate vector
$\Delta\mathbf{X}$	(L)	Displacement vector
$\boldsymbol{\xi}$	(-)	Vector of random numbers, normally distributed
$\boldsymbol{\xi_{sub}}$	(-)	Vector of a subset of $\boldsymbol{\xi}$
χ^2	(-)	Error-weighted data misfit
$\mathbf{Z}$	(-)	Vector of random numbers, uniformly distributed
Z_0	(Ω)	Characteristic impedance of TDR probe

ADE	Advection-dispersion equation
BB	Brilliant Blue
BTC	Breakthrough curve
DT0	No dispersive transformation applied
DT1	Dispersive transformation applied
ERT	Electrical resistivity tomography
FV	Finite-volume
GSDE	Generalized stochastic differential equations
IR	Infrared
MRI	Magnetic resonance imaging

RE	Richards' equation
R1	Two-sided reflection coefficient with water content
R2	One-sided reflection coefficient
RMSE	Root mean square error
RWPT	Random walk particle tracking
TDR	Time domain reflectometry
TS1	Linear time splitting
TS2	Non-linear time splitting
vGM	Van Genuchten-Mualem
WavAvg	Number of waveform average

Abstract

Groundwater level rise, root water uptake, or evaporation induces local upward water and solute fluxes in soils, causing soil salinization and rise of contaminants to the soil surface, and influencing the migration of solutes to the groundwater. It is known that soil heterogeneity strongly controls transport under infiltration conditions, but its effect on transport under upward flow conditions has barely been investigated. In this thesis, laboratory tracer experiments were conducted in artificial porous media with known heterogeneity under evaporation conditions and observations were compared with numerical simulations in order to improve the understanding of upward flow and transport processes.

High concentration gradients due to solute accumulation at the soil surface caused by evaporation are posing very high demands on Eulerian schemes for solving the advection-dispersion equation (ADE), while they have no negative effect on the stability of random walk particle tracking (RWPT) schemes. However, RWPT loses accuracy when the dispersion tensor or the water content is spatially discontinuous, a topic that is frequently-debated in RWPT literature. In this thesis, a new RWPT algorithm is presented that builds on the former concept of representing the discontinuities by partially reflecting barriers. Three improvements were developed that enhance the accuracy and efficiency of this concept by orders of magnitude.

In a composite porous medium, consisting of a cylindrical inner core with coarse sand that was surrounded by fine sand, dye and salt tracer experiments were conducted under constant evaporation conditions, and a Gd-DTPA^{2-} tracer experiment was monitored with magnetic resonance imaging (MRI) during a cycle of infiltration and evaporation. The key finding of these experiments was the formation of high solute concentration spots at the surface of the coarse material, which is contrary to the general expectation that solutes accumulate and precipitate in regions with finer texture and higher evaporation fluxes. Flow and transport simulations showed that molecular diffusion, which moves solutes away from the evaporating surface back into the porous medium, in combination with lateral water flow redistributes solutes towards locations with the lowest hydraulic head. The formation of high solute concentration spots at the surface of coarser regions, which usually represent preferential flow pathways during strong precipitation, may have an accelerating effect on the leaching of solutes.

In a three-dimensional spatially correlated heterogeneous laboratory soil composed of three different materials a salt tracer experiment was conducted under constant evaporation conditions and monitored with electrical resistivity tomography (ERT). The detailed comparison of monitored and modeled solute transport demonstrated that (1) the accuracy of the ERT observations was high enough to analyze errors of the flow and transport model, (2) a weak point of commonly-applied flow and transport models is the simplified representation of the evaporation boundary condition, in which mechanisms of lateral compensation of low evaporation zones are neglected, and (3) despite the deviations between monitored and modeled solute transport, there was a consistent and systematic transition of preferential upward transport pathways over the height of the laboratory soil.

Zusammenfassung

Ein Anstieg des Grundwasserspiegels, die Bodenwasseraufnahme durch Wurzeln oder Evaporation führen dazu, dass Wasser- und Stofftransport in Teilen des Bodens aufwärtsgerichtet sind. Aufwärtsgerichteter Wassertransport ist die Ursache für die Versalzung von Böden und den Aufstieg von Schadstoffen zur Oberfläche, und er beeinflusst den Stofftransport durch die Bodenzone ins Grundwasser. Es ist bekannt, dass die Heterogenität des Bodens entscheidend den Stofftransport unter Infiltrationsbedingungen kontrolliert, dagegen ist ihr Einfluss auf den Stofftransport unter Aufwärtsflussbedingungen nur wenig erforscht. In dieser Arbeit wurden Stofftransportexperimente im Labor in künstlichen porösen Medien mit definierter Heterogenität unter Verdunstungsbedingungen durchgeführt und anschließend mit numerischen Simulationen verglichen, mit dem Ziel das Prozessverständnis von aufwärtsgerichtetem Wasser- und Stofftransport zu verbessern.

Hohe Konzentrationsgradienten, die durch die unter Verdunstung stattfindende Stoffanreicherung an der Bodenoberfläche hervorgerufen werden, stellen hohe Ansprüche an Eulersche Ansätze zur Lösung der Advektions-Dispersionsgleichung, während die Stabilität der "Random Walk Particle Tracking"-Methode (RWPT) von ihnen nicht beeinflusst wird. An räumlichen Diskontinuitäten des Dispersionstensors oder des Wassergehalts verliert die RWPT-Methode allerdings an Genauigkeit, welches ein vielfach diskutiertes Thema in der Literatur über RWPT ist. In der vorliegenden Arbeit wird ein neuer RWPT-Algorithmus, der auf einem früheren Konzept die Diskontinuitäten mit Hilfe von teilweise reflektierenden Wänden zu behandeln basiert, vorgestellt. Dabei wurden drei Verbesserungen entwickelt, die die Genauigkeit und Effizienz dieses Konzepts um Größenordnungen verbessert.

In einem zusammengesetzten porösen Medium, bestehend aus einem zylinderförmigen inneren grobkörnigen Kern und einem feinkörnigen Mantel, wurden Farbstoff- und Salztracer-Experimente durchgeführt und ein Gd-DTPA^{2-}-Tracer-Experiment während eines Zyklus von Infiltration und Evaporation mit Magnetresonanztomographie beobachtet. Die größte Erkenntnis dieser Experimente war die Bildung von Zentren hoher Stoffkonzentration an der Oberfläche des grobkörnigen Materials. Dieses Resultat steht im Widerspruch zur generellen Erwartung, dass Stoffe in Regionen mit feinerer Textur und höheren Verdunstungsraten angereichert werden und auskristallisieren. Wasser- und Stofftransportsimulationen zeigten, dass molekulare Diffusion, die die Stoffe gegen die Advektion nach unten verlagert, zusammen mit lateralen Wasserflüssen die Stoffe zu den Regionen des geringsten hydraulischen Potentials verlagern. Die Anreicherung von Stoffen an der Oberfläche von grobkörnigen Bereichen, die im allgemeinen bei stärkeren Niederschlägen präferentielle Infiltrationspfade darstellen, beschleunigt vermutlich den Transport von Stoffen ins Grundwasser.

In einem drei-dimensionalen räumlich korrelierten heterogenen Laborboden bestehend aus drei verschiedenen Materialien wurde ein Salztracer-Experiment unter konstanten Verdunstungsbedingungen durchgeführt und mit elektrischer Widerstandstomographie (ERT) beobachtet. Der detaillierte Vergleich zwischen beobachtetem und modelliertem Aufstieg des Tracers zeigte dass (1) die Genauigkeit der ERT groß genug war, um Fehler des Wasser- und Stofftransportmodels zu untersuchen, (2) ein Schwachpunkt der gängigen Wasser- und Stofftransportmodelle die vereinfachte Repräsentation der Verdunstungsrandbedingung, in der Mechanismen der lateralen Kompensation von gering verdunstenden Bereichen vernachlässigt werden, ist, und (3) trotz der Abweichungen zwischen experimentell beobachtetem und modelliertem Stofftransport sich ein konsistenter und systematischer Übergang von präferentiellen Aufwärtstransportpfaden über die Höhe des Laborbodens darstellt.

Chapter 1

Introduction

The search for robust and integrated numerical models that accurately reproduce and predict water flow and solute transport in hydrological systems at different spatial and temporal scales drives research projects all over the world. In these models, the soil plays a key role because it links the atmosphere, surface water, vegetation, and human activities at the soil surface with subsurface hydrology. Quantitative understanding of flow processes in soils is crucial to estimate mass and energy fluxes and feedback mechanisms between hydrologic and atmospheric compartments (Seneviratne et al., 2006; Maxwell and Kollet, 2008). Accurate predictions of flow and transport processes are essential for the development of efficient and sustainable land management strategies that protect soil and groundwater resources (Vanclooster et al., 2005). Practical applications are, for example, the implementation of sustainable agricultural irrigation, the optimized application of fertilizers and pesticides, and the remediation of saline or contaminated soils.

The soil layer is thin, compared to its horizontal extent, and in most cases the net one-dimensional vertical fluxes within the soil and at its upper and lower boundaries are of interest (Harter and Hopmans, 2004). These one-dimensional fluxes are sought for at a large scale, like the field or catchment scale. However, field or catchment-scale flow and transport processes are strongly controlled by small-scale vertical and horizontal soil variability (Feyen et al., 1998). For a long time, one of the main challenges of research on flow and transport in soils has been the development of ‘upscaling’ concepts that transfer the small-scale process understanding to effective parameterizations and model approaches at the larger scale (National Research 1991; Vogel and Roth, 2003; Vereecken et al., 2007).

In this context, two- or three-dimensional process models that use a fully-deterministic approach to describe soil heterogeneity at the small scale represent an important tool. Regarding the flow and transport problem, they provide the opportunity to numerically analyze the complex effects that arise from the superposition of the non-linear soil hydraulic functions, the spatially and temporally variable boundary conditions, and the spatial heterogeneity of soil hydraulic properties. For example, Russo and Fiori (2008) used three-dimensional (3-D) flow and transport simulations of a realistic field scenario with spatially heterogeneous hydraulic properties and natural boundary conditions including root water uptake, to test the applicability of steady-state flow models for predicting solute transport under transient conditions. Recently, Samouelian et al. (2011) determined the effective unsaturated hydraulic conductivity of a natural soil structure by means of steady-state flow simulations at different pressure conditions. They used the results as benchmark to evaluate the accuracy of analytically-derived bounds of effective hydraulic conductivity. In numerical studies like these, the use of process models for the evaluation and derivation of upscaling approaches is based on the assumption that the model is a good approximation of reality. Whether this is true can only be evaluated with experimental data.

Several studies demonstrated the potential and limitations of numerical simulations based on the commonly-applied continuum theory for liquid flow and solute transport in unsaturated porous media, namely Richards' equation (RE) and advection-dispersion equation (ADE), to reproduce experimental observations under infiltration conditions (e. g., Wildenschild, 1999a; Kasteel et al., 2000; Coquet et al., 2005; Javaux et al., 2006; Vogel et al., 2006; Rossi et al., 2008). Reported deviations are often attributed to (1) the violation of underlying assumptions of RE (e. g., continuity of the air phase, rigidity of the porous medium) that may become critical under certain field and boundary conditions, (2) processes that were neglected in the parameterization of the hydraulic properties (e. g., water repellency, hysteresis, or non-equilibrium flow), and (3) the incomplete description of soil heterogeneity, in particular the macropore and fracture network.

When the groundwater level rises, plants take up water, or water evaporates from the soil surface, water flows locally upwards against gravity due to capillary forces. Upward water flow carries solutes towards the soil surface and is a key process in soil salinization and the transport of contaminants to the soil surface (Jury et al., 1990; Nassar and Horton, 1999; Ozturk and Ozkan, 2004). The increasing soil salinization is considered as one of the global issues of the 21st century (Seitz, 2002). According to the Food and Agricultural Organization, salinization affects approximately one tenth of the world's 2,600,000 km^2 of irrigated land (FAO, 2000). The remediation of soils that have become infertile due to salinization is very expensive and time-consuming, and in arid and semiarid regions often not realized because of the excessive need of fresh water (Abu-Zreig et al., 2006). Adequate drainage of the soil and sufficient water application are essential to prevent increasing soil salinity and are thus prerequisites for a sustainable management of arable land. Especially in arid and semiarid regions, money and fresh water are scarce so that the water management needs to be optimized to make sustainable agricultural practices possible. Detailed process understanding of water flow and solute transport within the soils is crucial to optimize this management. Here, the influence of soil heterogeneity plays again a key role and requires further investigation. Soil heterogeneity influences the evaporative water losses from and the lateral solute redistribution within the soil (Lehmann and Or, 2009) and thus also the rate of the salinization process. In the remediation process when water is applied to leach the salts, soil heterogeneity and preferential infiltration increase percolation water losses, while decreasing the salt leaching rate (Smets et al., 1997). In non-arid climates the net solute flux is downwards, but upward flow periods also occur under these climatic conditions. Therefore, upward flow and transport are relevant for solute migration also under such climatic conditions (Russo et al., 1998; Vanderborght et al., 2006).

Despite the significance of upward transport for groundwater quality management and sustainable agricultural practice, little effort has been made to experimentally measure upward transport at given boundary conditions with the goal to test existing numerical models. For a homogeneous porous medium, Mohamed et al. (2000) demonstrated that one-dimensional numerical modeling based on RE and ADE can accurately reproduce experimental observations of solute transport under liquid flow dominated (‘stage-1’) evaporation conditions. Recent experiments in composite porous media with vertical textural contrasts demonstrated that the coupling between different materials can lead to flow and transport that strongly deviate from what is expected from the homogeneous equivalents (Lehmann and Or, 2009; Nachshon et al., 2011). These studies pointed out that soil heterogeneity has an important influence on flow and transport under evaporations conditions. However, their experimental observations were not compared with numerical simulations. The fact that there is lack of combined experimental and numerical studies that focus on the effect of heterogeneity on flow and transport under upward flow conditions gives rise to the question whether the commonly-applied continuum models based on RE and ADE are a good approximation of reality under these conditions.

In the course of this thesis, this lack was addressed by comparing observations of tracer experiments in artificial porous media with known heterogeneity and under well-controlled evaporation conditions with numerical simulations based on RE and ADE. The general objective of the combined experimental and numerical studies was to contribute to the process understanding of solute transport in unsaturated heterogeneous porous media under evaporation conditions. The specific objectives of this thesis were:

1. to develop a numerical scheme that provides stable and accurate solutions of RE and ADE in unsaturated heterogeneous porous media under evaporation conditions,

2. to monitor and analyze solute redistribution processes that occur during evaporation periods after infiltration events,

3. to monitor and analyze the pattern of preferential upward solute transport

through a complex laboratory soil under constant evaporation conditions,

4. to evaluate the potentials and limitations of commonly-applied continuum flow and transport theory to reproduce the observed transport processes.

In this thesis, tracer experiments were performed in artificial porous media. This type of experiment is briefly introduced in the next section.

1.1 Laboratory soils as an intermediate step

When fully-deterministic two- or three-dimensional numerical models are used to reproduce observed transport in field soils or columns of undisturbed soil, results are often not satisfying and deviations between modeled and observed data occur (Kasteel et al., 2000; Coquet et al., 2005; Javaux et al., 2006; Vogel et al., 2006). Researchers have recognized that unresolved horizontal and vertical soil heterogeneity is a main contributor to these deviations. The uncertainty in the description of the soil heterogeneity and its effect on the modeled results are very difficult to quantify. One drawback is that this uncertainty masks researchers' views on further issues of the flow and transport model.

A method to study fundamental flow and transport processes and to verify numerical models is to perform experiments in laboratory soils with known heterogeneity under well-defined boundary conditions. The experiments in these porous media, in the following called 'laboratory soils', can be considered as intermediate step between pure numerical experiments and experiments in natural soils (Fig. 1.1). Laboratory soils are drastically simplified and in most cases designed to be conform to the underlying assumptions of the process model. Thus, many complexities, such as shrinkage and swelling, or macropore and fracture flow, that need to be addressed in natural soils are often excluded in laboratory soils. However, with regards to pure numerical studies, laboratory soil experiments are a step forward because the porous medium is physically real and numerical simulations can be fundamentally verified with real observations. The concept of creating artificial heterogeneous porous media allows studying the effect of soil heterogeneity on transport processes, because the hydraulic structure is perfectly known. It has been extensively applied to investigate migration of non-aqueous phase liquids in unsaturated and saturated porous media (e. g., Illangasekare et al., 1995; Hofstee et al., 1998; Nambi and Powers, 2000), and of dissolved substances in saturated (e. g., Sudicky et al., 1985; Silliman and Simpson, 1987; Silliman et al., 1998; Levy and Berkowitz, 2003; Yoon et al., 2008) and unsaturated porous media (e. g., Wildenschild, 1999b; Wildenschild, 1999a; Ursino et al., 2001; Ursino and Gimmi, 2004; Rossi et al., 2008).

For two decades, geophysical techniques have provided new opportunities for non-invasively monitoring solute migration in three-dimensional heterogeneous porous media (Binley et al., 2010, and references therein). The application of these 'hydrogeo-

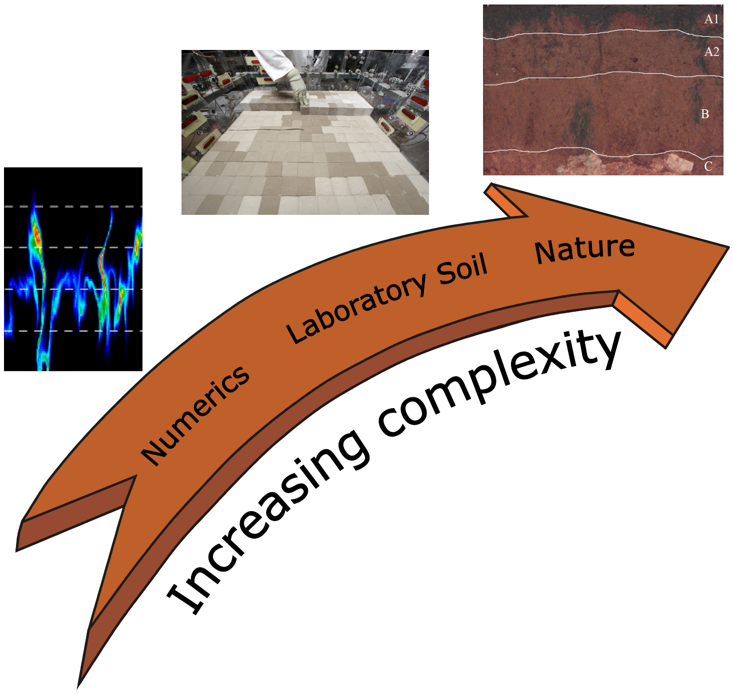

Figure 1.1: Increasing complexity of occurring physical processes. Left: Numerical simulations (adapted from Vanderborght et al., 2006), Center: Laboratory soil studies, Right: Observations in natural soils (adapted from Vogel et al., 2006).

physical' methods to well-controlled solute transport experiments in laboratory soils can be used to evaluate the quality of the obtained data because observations can be compared to well-constrained numerical simulations of the monitored process (Slater et al., 2002). Agreement between model simulations and the derived geophysical images indicates that the geophysical technique accurately monitors the spatially heterogeneous transport. From disagreements, deficiencies in the geophysical imaging and/or in the model concepts can be inferred. With respect to the laboratory soil experiment of this thesis, a specific objective was to evaluate the applicability and accuracy of electrical resistivity tomography (ERT) to monitor solute transport under upward flow conditions.

1.2 Thesis outline

Chapters 2 to 4 and Appendix C are based on four manuscripts that are published in or were submitted to international peer-reviewed journals. Since the chapters deal with different aspects of upward transport, each of them has an individual abstract, introduction and literature review, material and methods, results and discussions, and conclusions section. In the following paragraphs, an overview of each chapter is given:

The work in Chapter 2 was motivated by the numerical instabilities encountered when using existing Eulerian, finite-element approaches to simulate the high concentration gradients at the soil surface that occur during evaporation. The accuracy of random walk particle tracking (RWPT) simulations is not affected by these conditions. Instead, RWPT loses accuracy in the presence of discontinuities of the dispersion tensor and water content, a topic that is under controversial discussion in RWPT literature. In Chapter 2, a RWPT algorithm that efficiently and accurately handles these discontinuities is presented. The new RWPT algorithm was coupled with a cell-centered finite-volume flow model (Ippisch et al., 2006) and provides accurate solutions to transport problems under evaporation conditions. The coupled code was the basis for all simulations presented in this thesis.

In Chapter 3, a solute redistribution process that occurs close to the evaporating surface of heterogeneous porous media is introduced. The 'near-surface' solute redistribution is demonstrated with dye and salt tracer experiments in simple composite porous media. In a second experiment, the migration of the tracer Gd-DTPA^{2-} was monitored with magnetic resonance imaging (MRI), and near-surface solute redistribution is demonstrated in the context of a cycle of infiltration and evaporation. The experimental observations of the near-surface solute redistribution are compared to numerical simulations based on common continuum theory for flow and transport.

In Chapter 4, results of the first tracer experiment in a laboratory soil under upward flow conditions are presented. ERT-derived observations of the tracer migration are compared with numerical simulations. The deviations are analyzed and attributed to ERT and modeling errors by means of a detailed error analysis. ERT errors are constrained by inversion of synthetic ERT data. With respect to modeling errors, the spatial pattern of evaporation rates at the soil surface is identified as one of the major issues in simulating upward transport. The three-dimensional observation of the transport process highlights the pattern of preferential pathways that develops under upward flow conditions.

In Chapter 5, summarizing conclusions and perspectives on future research are given.

In Appendix A, the reference root mean square error of a RWPT verification scenario in Chapter 2 is derived. Appendix B provides photographic documentation of the experimental setup and the packing of the laboratory soil in Chapter 4. In Appendix C, the accuracy of bulk electrical resistivity measurements with the TDR100 cable tester of Campbell Scientific (Logan, UT) is critically evaluated. The device was used in the laboratory soil experiment of Chapter 4. Technical shortcomings of the device are discussed and it is shown that in the past these deficiencies led to the wrong conclusion that the series resistor model is not suitable for calibrating a TDR setup. The opposite is demonstrated here. Further, a method is proposed to overcome the technical issues of the TDR100.

Chapter 2

Efficient random walk particle tracking algorithm for modeling advective dispersive transport in heterogeneous porous media*

Abstract

Random walk particle tracking (RWPT) is a well established and efficient alternative to grid-based Eulerian approaches when simulating the advection-dispersion transport problem in highly heterogeneous porous media. However, RWPT methods lose accuracy when the dispersion tensor or the water content is spatially discontinuous. We present improvements to the concept of a partially reflecting barrier used to account for these discontinuities: (1) the non-linear time splitting with $\sqrt{\Delta t} = \sqrt{\Delta t_1} + \sqrt{\Delta t_2}$ that corrects for the systematic overestimation of the second dispersion displacement across an element interface when linear time splitting is used, (2) the one-sided reflection coefficient that correctly represents the effect of discontinuous dispersion coefficients and water content but eliminates redundant reflections of the two-sided reflection coefficient and limits the error for discrete Δt, and (3) the transformation of the dispersive displacement across element interfaces for complex multidimensional transport problems. The proposed improvements are verified numerically by comparison with an analytical solution and a reference RWPT method. Results indicate an increased efficiency and accuracy of the new RWPT algorithm. Because the new algorithm efficiently simulates both advection- and dispersion-dominated transport conditions, it enhances the applicability of RWPT to scenarios in which both conditions occur, as for example in the highly-transient unsaturated zone. The algorithm is easily implemented and it is shown that computational benefit increases with increasing variability of the hydraulic parameter field.

---

[*] adapted from: Bechtold, M., J. Vanderborght, O. Ippisch and H. Vereecken. 2011b. Efficient random walk particle tracking algorithm for advective dispersive transport in media with discontinuous dispersion coefficients and water contents. Accepted for publ. in Water Resour. Res.

2.1 Introduction

The increasing knowledge about subsurface heterogeneity and its crucial effects on water flow and solute transport led to highly-resolved numerical models at different scales (Coquet et al., 2005; Javaux et al., 2006; Kasteel et al., 2007). This development increased the computational costs of numerical simulations. At the same time, inverse modeling studies of multidimensional flow and transport problems, like geostatistical inversions, become more frequent (e. g., Kowalsky et al., 2004; Nowak et al., 2010). These studies require multiple forward runs of computationally expensive simulations. Both developments result in an ongoing demand for efficient modeling codes, despite the availability of more powerful computers.

There is a long discussion about the most efficient and robust concepts for modeling solute transport in highly heterogeneous porous media (Delay et al., 2005). Two different concepts are mostly used to numerically solve the advection-dispersion equation (ADE): (1) grid-based Eulerian and (2) Lagrangian approaches. Among the Lagrangian approaches, the most common one is Random Walk Particle Tracking (RWPT). This method is based on the analogy between stochastic processes and diffusion theory (Kinzelbach and Uffink, 1991). Applied to solute transport problems, the solute mass is represented by a large number of particles. Fundamental works in stochastic physics demonstrated the similarity between ADE and Fokker-Planck equation, which describes the temporal evolution of the probability density function of the particle velocity (Delay et al., 2005). Based on this similarity, in RWPT, particles perform displacements that are composed of an advective (deterministic) and a dispersive (stochastic) component, whereby the advective movement is the sum of the fluid flow velocity and the velocity that originates from the spatial continuous variation of the dispersion tensor and water content (LaBolle et al., 1996). In the limit of an infinite number of particles, the resulting frequency distribution equals a solution of the Fokker-Planck equation, and thus also a solution of the ADE.

In subsurface hydrology, RWPT methods were first applied to groundwater flow problems (Ahlstrom et al., 1977; Prickett et al., 1981). For advection-dominated transport problems, in which grid-based Eulerian methods suffer from numerical diffusion, they became a well established alternative for modeling subsurface transport (e. g., Tompson and Gelhar, 1990; LaBolle et al., 1996; Fernandez-Garcia et al., 2005; Maxwell et al., 2007; Park et al., 2008). For these conditions, RWPT is considered to be more efficient in providing accurate results because the grid-based Eulerian approaches require a computational expensive grid refinement and time step reduction to overcome numerical diffusion (Lichtner et al., 2002; Salamon et al., 2006).

Recently, Delay et al. (2005) pointed out that RWPT has been rarely used in vadose zone hydrology, although high variations in water content and flow velocity are very common for the vadose zone and RWPT is supposed to efficiently model transport under these conditions. RWPT can also be an attractive alternative for handling high concentration gradients due to solute accumulation either at the soil surface caused by evaporation or at roots caused by root water uptake, scenarios which are posing very high demands on the numerical solution scheme. Recently, it has been shown that RWPT can be used to efficiently simulate large scale contaminant transport problems in coupled unsaturated/saturated domains (Maxwell et al., 2009).

RWPT methods are by definition globally mass conservative, which is an important advantage of the method compared to most Finite-Element and Finite-Difference schemes. However, a difficulty of the RWPT method is that locally, the particle displacements are erroneous when the dispersion tensor or the water content is spatially discontinuous. Such discontinuities result from abrupt changes of the physical properties of the porous material (e. g., at abrupt facies changes or local compaction zones) or from characteristics of the computed velocity field obtained from a numerical model such as cell-centered finite volume based flow models (Delay et al., 2005; Salamon et al., 2006). When neglecting these discontinuities, RWPT simulations may provide transport results with considerable errors (LaBolle et al., 1996).

Methods that reduce the errors related to the discontinuities are frequently debated in RWPT literature and are the topic of this chapter. There were three conceptually different methods proposed: the interpolation method (LaBolle et al., 1996), the generalized stochastic differential equations (GSDE) method (LaBolle et al., 2000) and the concept of a partially reflecting barrier (Hoteit et al., 2002; Lim, 2006). In these methods, algorithmic modifications were introduced to the performance of the advective and dispersive displacements. The modified algorithms lead to different particle frequency distributions in the presence of discontinuities and to a better approximation of the true solution of the ADE.

While the interpolation method and the GSDE method were successfully applied to complex three-dimensional transport problems (e. g., Weissmann et al., 2002; Fernandez-Garcia et al., 2005; Seeboonruang and Ginn, 2006; Salamon et al., 2007), the general applicability of the reflection barrier method and its convergence to the true solution is controversially discussed (Salamon et al., 2006). Based on a comparison study, Salamon et al. (2006) proposed that the interpolation method presented the most efficient alternative for most of the complex three-dimensional flow problems, especially with respect to scenarios characterized by low fluid velocities and abrupt contrasts.

However, it is well known that the interpolation method needs a very high spatial resolution of the interpolation grid close to the interface and small time steps (LaBolle et al., 1996), which is computationally expensive. The reflection barrier method does not require grid refinement to represent discontinuous dispersion tensors or abrupt changes in the water content. This advantage can reduce computational costs considerably. It is therefore promising to improve the accuracy of the reflection barrier method and to prove its general applicability.

This manuscript is organized as follows. In the second section of the manuscript, we will briefly review the interpolation and reflection barrier method as they are currently implemented in transport codes. For the reflection barrier method, we identify some problems and inconsistencies with respect to its implementation, which may explain why the reflection barrier method was outperformed by other methods in the comparison study of Salamon et al. (2006). Based on the identified inconsistencies, we will propose improvements to the reflection barrier method. In the third section, we discuss details about the numerical implementation of the reflection barrier method and describe and motivate the test scenarios used for the numerical verification of the proposed RWPT algorithm. In the forth section, we use the numerical results to evaluate the benefit of the improved algorithm. The improved reflection barrier method is compared with the interpolation method (LaBolle et al., 1996). In the fifth section convergence and efficiency issues are discussed and we will provide practical application aspects of the new algorithm. Conclusions are provided in the sixth section.

2.2 Theory

2.2.1 Reflection barrier and interpolation method

In porous media, the mass balance equation of a conservative solute is described by the advection-dispersion equation (ADE),

$$\theta\frac{\partial C}{\partial t} = -\theta\mathbf{u}\cdot\nabla C + \nabla\cdot(\theta\mathbf{D}\cdot\nabla C) \tag{2.1}$$

where θ is the volumetric water content (L^3 L^{-3}), C is the concentration (M L^{-3}), t is time (T), $\mathbf{u}$ is the velocity vector (L T^{-1}), and $\mathbf{D}$ is the local-scale dispersion tensor (L^2 T^{-1}), here given for a three-dimensional isotropic porous medium (Bear, 1972),

$$\begin{aligned}\mathbf{D} &= (\alpha_T\|\mathbf{u}\|+D_m)\mathbf{I} + (\alpha_L-\alpha_T)\frac{\mathbf{u}\mathbf{u}^T}{\|\mathbf{u}\|}\\ &= \begin{pmatrix} \alpha_T\|\mathbf{u}\|+D_m+(\alpha_L-\alpha_T)\frac{u_x^2}{\|\mathbf{u}\|} & (\alpha_L-\alpha_T)\frac{u_xu_y}{\|\mathbf{u}\|} & (\alpha_L-\alpha_T)\frac{u_xu_z}{\|\mathbf{u}\|}\\ (\alpha_L-\alpha_T)\frac{u_yu_x}{\|\mathbf{u}\|} & \alpha_T\|\mathbf{u}\|+D_m+(\alpha_L-\alpha_T)\frac{u_y^2}{\|\mathbf{u}\|} & (\alpha_L-\alpha_T)\frac{u_yu_z}{\|\mathbf{u}\|}\\ (\alpha_L-\alpha_T)\frac{u_zu_x}{\|\mathbf{u}\|} & (\alpha_L-\alpha_T)\frac{u_zu_y}{\|\mathbf{u}\|} & \alpha_T\|\mathbf{u}\|+D_m+(\alpha_L-\alpha_T)\frac{u_z^2}{\|\mathbf{u}\|} \end{pmatrix}\end{aligned} \tag{2.2}$$

where α_T (L) and α_L (L) are the transversal and longitudinal dispersivities, D_m is the effective molecular diffusion coefficient (L^2 T^{-1}), and $\mathbf{I}$ is the identity matrix. The stochastic differential equation equivalent to the ADE can be written as (Tompson and Gelhar, 1990),

$$\mathbf{X}(t+\Delta t) = \mathbf{X}(t)+\left[\mathbf{u}[\mathbf{X}(t)] + \nabla\cdot\mathbf{D}[\mathbf{X}(t)] + \frac{\mathbf{D}[\mathbf{X}(t)]}{\theta[\mathbf{X}(t)]}\cdot\nabla\theta[\mathbf{X}(t)]\right]\Delta t+\mathbf{B}[\mathbf{X}(t)]\boldsymbol{\xi}\sqrt{\Delta t}$$

(2.3)

where $\mathbf{X}$ is the coordinate vector (L), $\boldsymbol{\xi}$ is a vector of three random numbers normally distributed with zero mean and unit variance, and $\mathbf{B}$ is the dispersion displacement matrix (Lichtner et al., 2002),

$$\mathbf{B} = \begin{pmatrix} \frac{u_x}{\|\mathbf{u}\|}\sqrt{2(\alpha_L\|\mathbf{u}\|+D_m)} & -\frac{u_x u_z}{\|\mathbf{u}\|\sqrt{u_x^2+u_y^2}}\sqrt{2(\alpha_T\|\mathbf{u}\|+D_m)} & -\frac{u_y}{\sqrt{u_x^2+u_y^2}}\sqrt{2(\alpha_T\|\mathbf{u}\|+D_m)} \\ \frac{u_y}{\|\mathbf{u}\|}\sqrt{2(\alpha_L\|\mathbf{u}\|+D_m)} & -\frac{u_y u_z}{\|\mathbf{u}\|\sqrt{u_x^2+u_y^2}}\sqrt{2(\alpha_T\|\mathbf{u}\|+D_m)} & \frac{u_x}{\sqrt{u_x^2+u_y^2}}\sqrt{2(\alpha_T\|\mathbf{u}\|+D_m)} \\ \frac{u_z}{\|\mathbf{u}\|}\sqrt{2(\alpha_L\|\mathbf{u}\|+D_m)} & \frac{\sqrt{u_x^2+u_y^2}}{\|\mathbf{u}\|}\sqrt{2(\alpha_T\|\mathbf{u}\|+D_m)} & 0 \end{pmatrix} \tag{2.4}$$

where u_x, u_y and u_z are the velocities in x-, y-, and z-direction and $\|\mathbf{u}\|$ is the Euclidean norm of the velocity. For diffusion-only problems or when $u_x = u_y = 0$, $\mathbf{B}$ is obtained by taking the limit of $\mathbf{B}$ for the respective velocity components going to zero, which is well defined. Using the central limit theorem, the normal random vector $\boldsymbol{\xi}$ of Eq. 2.3 can be replaced by $\sqrt{3}\mathbf{Z}$ where $\mathbf{Z}$ is a random vector uniformly distributed between -1 and 1, which has been shown to be computationally more efficient (Uffink, 1985). The term $\left[\mathbf{u}[\mathbf{X}(t)] + \nabla\cdot\mathbf{D}[\mathbf{X}(t)] + \frac{\mathbf{D}[\mathbf{X}(t)]}{\theta[\mathbf{X}(t)]}\cdot\nabla\theta[\mathbf{X}(t)]\right]$ of Eq. 2.3 is responsible for the advective (deterministic) movement of a particle, which is the sum of the fluid velocity and a velocity that originates from the spatial variation of $\mathbf{D}$ and θ (LaBolle et al., 1996). The term $\mathbf{B}[\mathbf{X}(t)]\boldsymbol{\xi}\sqrt{\Delta t}$ represents the dispersive (stochastic) movement.

When Eq. 2.3 is applied to a large number of particles, the resulting particle distributions mimic the Fokker-Planck equation and thus provide a solution to the ADE (Delay et al., 2005). However, RWPT algorithms need an additional adaptation when the terms of Eq. 2.3 accounting for continuous spatial variations of the dispersion tensor and water content are not defined, i. e. the dispersion tensor or the water content are discontinuous (LaBolle et al., 1996; LaBolle et al., 1998). Linear parabolic partial differential equations like the ADE should obey a maximum principle when a mass-conservative flow field is used. This means that the maxima (and minima) of concentration are either at the inflow boundaries or in the initial condition. Over time no new extremes are created, as the linear transport conserves the shape of a concentration pulse and diffusion tends to diminish extreme values. This property should be retained by any reasonable numerical scheme. Of course for RWPT methods this can only be true in a statistical sense, i. e. no new extremes larger than the pure statistical fluctuations due to the discretization error should be introduced. If discontinuities of the dispersion tensor and/or the water content are neglected, this is no longer guaranteed, resulting in potentially very large solute concentrations in low dispersion regions. This effect has been previously reported as ‘local mass conservation error’ (Semra et al., 1993; LaBolle et al., 1996). However, as particle tracking methods are by definition mass conservative, we prefer to call it 'monotonicity preservation error' in this paper, in reference to the potential violation of the maximum principle.

Before introducing the interpolation and reflection barrier method, which were both developed to avoid 'monotonicity preservation errors' due to discontinuities in $\mathbf{D}$ or θ, it is necessary to define the use of grids in RWPT. Primarily, RWPT is a grid-free method. For purely advective transport, convergence to the true solution is achieved by accurately integrating the velocity along the trajectory of each particle and by decreasing the mass of the individual particles representing the total solute mass, while increasing the total number of particles. For advective-dispersive transport, convergence also requires a sufficiently small time step. However, numerical grids are required when the spatially varying variables governing the particle displacements (in this study: velocity, dispersion tensor and water content) cannot be described analytically at each location, but must be obtained from a grid-based numerical solution of the flow problem. Numerical grids are used in RWPT algorithms to obtain the variables at the particle location by adequate interpolation functions (LaBolle et al., 1996). Grids are also often used to derive solute concentrations from the particle distributions. However, in the following, we refer to the first type of grids when we discuss the effect of grid refinement on the numerical solution of RWPT.

In the interpolation method, the discontinuity in the dispersion tensor or the water content is replaced by a smooth transition interpolating the discontinuous values. This introduces an error which gets smaller, with decreasing size of the interpolation region. The interpolation method is commonly used as 'hybrid' scheme (LaBolle et al., 1996). In this scheme, the term $\mathbf{u}\Delta t$ is calculated from the flow solution in the same way as in a standard particle tracking scheme. Bilinear interpolation is used for the calculation of the terms $\left[\nabla\cdot\mathbf{D}[\mathbf{X}(t)] + \frac{\mathbf{D}[\mathbf{X}(t)]}{\theta[\mathbf{X}(t)]}\cdot\nabla\theta[\mathbf{X}(t)]\right]\Delta t$ and $\mathbf{B}[\mathbf{X}(t)]\boldsymbol{\xi}\sqrt{\Delta t}$ of Eq. 2.3. This scheme maintains the local fluid mass balance from the flow solution, while the smoothed field allows the approximation of the divergence of the dispersion tensor and of the gradient of the water content in the vicinity of the discontinuity. Any smoothing error by the bilinear interpolation of the velocities and water contents affects the terms with $\mathbf{D}$, $\mathbf{B}$ and θ. Convergence is achieved by refinement of the interpolation grid to reduce the smoothing zone at the discontinuity. This requires also a simultaneous time step reduction to allow particles to explore the smoothing zone.

Another approach to account for discontinuous dispersion tensors and water contents is the concept of a partially reflecting barrier, first introduced by Uffink (1985). The advective displacement is calculated from the flow solution and performed in the same way as in a standard RWPT scheme that accounts for continuous changes of $\mathbf{D}$ and θ. Subsequently, the dispersive displacement accounts for the discontinuous changes of $\mathbf{D}$ and θ. The fundamental principle of the reflection barrier concept is to partially reflect particles that cross the discontinuity during the dispersive displacement. The difficulty is to design this reflection barrier in such a way that the correct solution of the ADE is obtained. This concept is basically implemented by generating an additional random number when a particle reaches an interface during a specific displacement. If the random number is greater than the reflection coefficient, the particle crosses the interface; otherwise, it is reflected. An important advantage of the reflection barrier method is that it does not require a finer spatial discretization close to the interface and thus can operate with larger time steps.

After the reflection barrier method was introduced by Uffink (1985) several concepts were proposed (e. g., Cordes et al., 1991; Semra et al., 1993; LaBolle et al., 1998) which differ in the definition of (1) the reflection coefficient and (2) the length of the displacement for a particle which crosses the interface (Ackerer and Mose, 2000). The reflection scheme that is now generally considered as the only one that preserves monotonicity was first presented by Semra et al. (1993). It was validated by Hoteit et al. (2002) and is now mostly known as the reflection scheme of Hoteit et al. (2002). Recently, Ramirez et al. (2008) referred to this scheme as the Hoteit-Mose-Younes-Lehmann-Ackerer reflection (HMYLA-reflection).

In the scheme of Hoteit et al. (2002), which was developed for a medium with a homogeneous water content, the probability that a particle that reached, during a dispersive displacement, the interface between two elements E_1 and E_2 with dispersion coefficients D_1 and D_2 goes into E_1 is $P_1 = \frac{\sqrt{D_1}}{\sqrt{D_1}+\sqrt{D_2}}$ and the probability that a particle goes into E_2 is $P_2 = 1 - P_1 = \frac{\sqrt{D_2}}{\sqrt{D_1}+\sqrt{D_2}}$. P_1 can also be interpreted as the probability that a particle that reaches the interface during a dispersive displacement from E_2 will enter E_1 and vice versa for P_2. The reflection coefficient has to be applied for particles coming to the interface from both directions (Fig. 2.1). Recently, Ramirez et al. (2008) provided a physical foundation for the reflection coefficients of Hoteit et al. (2002) on the basis of the α-skew Brownian motion theory. Lim (2006) determined from the analytical solution for diffusion in a composite porous medium an extended reflection coefficient for heterogeneous effective porosities or water contents θ, where:

$$P_1 = \frac{\theta_1\sqrt{D_1}}{\theta_1\sqrt{D_1} + \theta_2\sqrt{D_2}} \text{ and } P_2 = 1 - P_1 = \frac{\theta_2\sqrt{D_2}}{\theta_1\sqrt{D_1} + \theta_2\sqrt{D_2}} \tag{2.5}$$

In the case of reactive transport, where E_1 and E_2 are characterized by retardation factors $f_{ret,1}$ and $f_{ret,2}$ ($f_{ret} \geq 1$), D_1 and D_2 can be replaced by $D_1/f_{ret,1}$ and $D_2/f_{ret,2}$, respectively (Lim, 2006).

When the particle crosses an interface by a dispersive displacement during a time step having the size Δt, the particle displacement needs to be split up in two steps. As proposed by Hoteit et al. (2002) and presented in subsequent studies (e. g., Delay et al., 2005; Lim, 2006; Salamon et al., 2006), Δt is split linearly with $\Delta t = \Delta t_1 + \Delta t_2$, where Δt_1 is the time needed for the particle to reach the interface. At the element

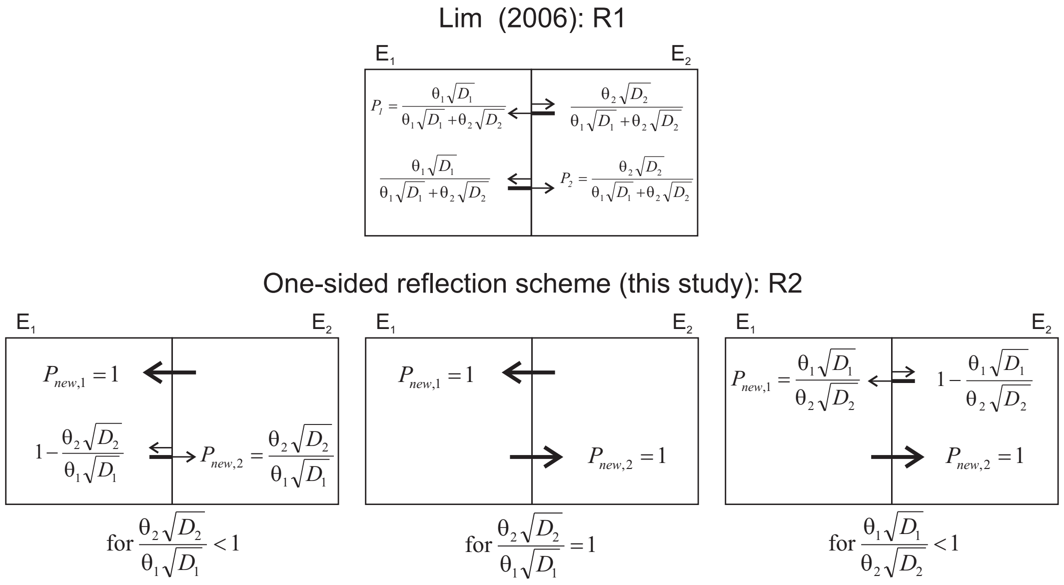

Figure 2.1: Summary of the reflection coefficients, R1: Lim (2006) and R2 (one-sided reflection scheme, this study), used in the numerical simulations. The fraction of the particles that is passed or reflected is indicated at the tip of each arrow. P_1 and $P_{new,1}$ are interpreted as the probability that a particle that reaches the interface from E_2 will enter E_1 and vice versa for P_2 and $P_{new,2}$.

interface, the reflection coefficient is calculated and if the random number allows the particle to pass, the displacement in the next element is calculated based on the dispersion and velocity of E_2 using Δt_2. This splitting of the displacement is considered as an important precondition for preserving monotonicity (Ackerer and Mose, 2000). However, we will show that a linear time splitting, which is correct for an advective displacement, causes a systematic overestimation of the second dispersive displacement. In the next section, we derive the correct equation for determining Δt_2.

A second problem of the reflection barrier method as proposed by Hoteit et al. (2002) and Lim (2006) is that even in homogeneous media, i. e. $D_1 = D_2$ and $\theta_1 = \theta_2$, particles are reflected at element interfaces. We will show that these reflections slow down the dispersive spreading of a solute pulse and that the reflection barrier method only leads to correct results when the ratio of particle displacements with reflection to the particle displacements without reflection goes to 0. This is the case when the distance between partially reflecting element interfaces $\Delta L \to \infty$ or the time step $\Delta t \to 0$. We will present an alternative reflection scheme that reduces the number of particle reflections and therefore leads to more accurate results for larger values of Δt or smaller values of ΔL.

Finally, we propose a third improvement to the reflection barrier method: the transformation of the dispersive displacement when a particle crosses the interface during a dispersive displacement. We show that the transformation improves the application of the reflection barrier method in complex multidimensional transport problems with spatially varying anisotropic dispersion tensors.

2.2.2 Improvements to the reflection barrier method

All displacement and reflection probabilities considered in the following refer only to purely dispersive, i. e. stochastic, displacements. This implies that the advective and dispersive displacement must be performed in two subsequent displacement steps, i. e. the dispersive displacement is calculated at the new particle location at the end of the advective movement.

2.2.2.1 Correct time splitting for dispersion

If a particle is allowed to cross the interface of two elements with different dispersion tensor or water content, the dispersive displacement in the new element has to be recalculated consistent with the reflection coefficient to obtain a correct solution of the ADE (Ackerer and Mose, 2000; Hoteit et al., 2002). To be consistent with the reflection coefficient, the ratio of the mean lengths of the dispersive displacements towards and away from the interface must be equal to the ratio of the square root of the dispersion coefficients according to the reflection barrier theory of Hoteit et al. (2002). If this is not the case, particles end up at an erroneous distance to the interface and the probability of a back jump in the next step would be too high or too low, with the consequence that the dispersive displacements across the element interface are not balanced accurately. In case of a particle reflection, there is no need for recalculating the dispersive displacement. The remaining displacement is performed in the opposite direction.

There are two reasons that indicate that the same random number must be used for the second displacement. Both reasons are related to the fact that the subset of random numbers that cause a displacement to the interface describes a frequency distribution that differs from the original one. First, the numbers of this subset are either all positive or all negative. If a new random number would be drawn at the element interface, 50 % of the random numbers would cause an immediate back jump, which is inconsistent with the reflection barrier. In contrast, using the same number ensures a displacement in the same direction like the first displacement and thus away from the interface into the new element. Second, there is higher probability that particles with higher random numbers are displaced to the interface. At the interface, however, only part of the individual random number took already effect. By drawing a new random number, the remaining fraction would be ignored. This would lead to an average of $\boldsymbol{\xi}\sqrt{\Delta t}$ that is unequal to 0, because the Δt of high random numbers would be inevitably smaller in the respective direction. This would introduce an undesired bias, because, in this case, $\boldsymbol{\xi}$ would contain a part that could be added to the deterministic movement.

However, keeping the random number has important consequences for the splitting of the time step at the interface. The total dispersive displacement ΔX across an element interface can be split in two displacements: ΔX_1 and ΔX_2, where ΔX_1 is the displacement to, and ΔX_2 is the displacement from the element interface with:

$$\Delta X_1 = \xi\sqrt{2D_1\Delta t_1} \text{ and } \Delta X_2 = \xi\sqrt{2D_2\Delta t_2} \tag{2.6}$$

For the homogeneous case with $D = D_1 = D_2$ a reflection barrier is in fact not necessary, but can be used to evaluate the effect of a time splitting. Obviously ΔX is overestimated when we recalculate the dispersion step at the interface by splitting up the time step linearly with $\Delta t = \Delta t_1 + \Delta t_2$, as it is done up to now in the reflection barrier method, as

$$\Delta X = \xi\sqrt{2D(\Delta t_1 + \Delta t_2)} < \xi\sqrt{2D\Delta t_1} + \xi\sqrt{2D\Delta t_2} \tag{2.7}$$

To be consistent with the definition of the reflection coefficient in the homogenous case, the total dispersive displacement calculated at the starting location, however, must be equal to the sum of the split dispersive displacements:

$$\xi\sqrt{2D\Delta t} = \xi\sqrt{2D\Delta t_1} + \xi\sqrt{2D\Delta t_2} \tag{2.8}$$

This simplifies to the non-linear time splitting equation,

$$\sqrt{\Delta t} = \sqrt{\Delta t_1} + \sqrt{\Delta t_2} \tag{2.9}$$

As Δt_1 is an unknown but ΔX_1 a known variable, we insert $\sqrt{\Delta t_1} = \frac{\Delta X_1}{\xi\sqrt{2D_1}}$ in Eq. 2.9 and solve for Δt_2,

$$\Delta t_2 = \left(1 - \frac{\Delta X_1}{\xi\sqrt{2D_1\Delta t}}\right)^2 \Delta t \tag{2.10}$$

This new time splitting scheme is straightforward to implement in a particle tracking code. Eq. 2.10 is equally applicable for the heterogeneous case.

2.2.2.2 One-sided reflection coefficient

Let us assume that the pore water concentrations of two elements E$_1$ and E$_2$ are equal, but the volumetric water contents are different (e. g., 10 particles in E$_1$ with a water content of 0.25, and 20 particles in E$_2$ with a water content of 0.5). To preserve monotonicity, the number of particles that cross the element interface from E$_1$ into E$_2$ by dispersive displacements should, on average, be equal to the number of particles that cross from E$_2$ into E$_1$, independent of the dispersion coefficients and water contents in the two elements. If the dispersion coefficients and volumetric water contents in E$_1$ and E$_2$ are different, the probability β_1 that a particle from E$_1$ reaches the interface is different from the probability β_2 that a particle from E$_2$ reaches the interface, which is the case also for identical pore water concentrations in E$_1$ and E$_2$. The reflection coefficients P_1 and P_2 (see above) correct for the difference in probability β_1 and β_2 so that for the same pore water concentrations in E$_1$ and E$_2$, the same amount of particles cross from E$_2$ into E$_1$ as from E$_1$ to E$_2$,

$$P_2\beta_1 = \frac{\theta_2\sqrt{D_2}}{\theta_1\sqrt{D_1}+\theta_2\sqrt{D_2}}\beta_1 = \frac{\theta_1\sqrt{D_1}}{\theta_1\sqrt{D_1}+\theta_2\sqrt{D_2}}\beta_2 = P_1\beta_2 \tag{2.11}$$

In this two-sided reflection scheme, particles coming from both E$_1$ and E$_2$ are reflected at the interface with different reflection probabilities P_1 and P_2. Note that even in a homogeneous medium ($D_1 = D_2$ and $\theta_1 = \theta_2$) 50 % of the particles are reflected at any interface between two elements, though no reflections would be needed at all to preserve monotonicity. Instead of always reflecting a fraction of the particles at both sides of the interface, it is possible to obtain the same result by reflecting an adjusted portion of particles at one side only. The reflection coefficients can be redefined by rewriting equation Eq. 2.11 as

$$\beta_2 = \frac{\theta_2\sqrt{D_2}}{\theta_1\sqrt{D_1}}\beta_1 \text{ or } \beta_1 = \frac{\theta_1\sqrt{D_1}}{\theta_2\sqrt{D_2}}\beta_2 \tag{2.12}$$

The reflection probabilities are then given as

$$P_{new,1} = 1 \text{ and } P_{new,2} = \frac{\theta_2\sqrt{D_2}}{\theta_1\sqrt{D_1}} \text{ for } \frac{\theta_2\sqrt{D_2}}{\theta_1\sqrt{D_1}} < 1 \tag{2.13}$$

or

$$P_{new,2} = 1 \text{ and } P_{new,1} = \frac{\theta_1\sqrt{D_1}}{\theta_2\sqrt{D_2}} \text{ for } \frac{\theta_1\sqrt{D_1}}{\theta_2\sqrt{D_2}} \leq 1 \tag{2.14}$$

where $P_{new,1}$ is the probability that a particle that reaches the interface coming from E$_2$ crosses into E$_1$, and $P_{new,2}$ the probability that a particle that reaches the interface coming from E$_1$ crosses into E$_2$ (see also Fig. 2.1).

The elimination of the reflection coefficient at one of the sides is balanced by a reduction of the reflected particles at the other side. Thus, the number of particles affected by the reflection is always smaller when applying the one-sided reflection scheme compared to the two-sided reflection coefficients of Hoteit et al. (2002) and Lim (2006). The elimination of the redundant reflections is beneficial as each reflection causes a numerical error. The reason for the error can be easily understood considering the case of a medium with a homogeneous dispersion but with an interface between two elements. When initially all particles are at one side of the interface, the two-sided reflection scheme will reduce the portion of particles that moves into the other side of the interface (because 50 % are reflected) and will therefore reduce the effective dispersion, resulting in a slow convergence with decreasing time step size. The one-sided reflection scheme does not introduce reflections at the interface between two elements in a homogeneous medium and therefore does not lead to errors in the prediction of the spreading of particles in such a medium. Therefore, it is more efficient to use the one-sided reflection scheme. We will show that the one-sided reflection scheme can reduce modeling errors tremendously, especially for large time steps.

2.2.2.3 Transformation of the dispersive displacement

If the dispersion coefficient is not a scalar but a tensor, a more elaborate transformation of the dispersive displacement in the second element, $\Delta\mathbf{X_2}$, than $\Delta\mathbf{X}_2 = \xi\mathbf{B}_2\sqrt{\Delta t_2}$, which would be expected for a scalar dispersion coefficient according to Eq. (6), is necessary. This can be illustrated by a simple two-layer example. This scenario can be considered as a soil above an aquifer. In the upper layer (soil), the velocity, u_z, is directed vertically downwards equal to -1 m d^{-1} and in the lower layer (aquifer), the velocity, u_x, is parallel to the x-axis with a value equal to 1 m d^{-1}. Both layers have a longitudinal dispersivity $\alpha_L = 10$ m and a transverse dispersivity $\alpha_T = 1$ m. The corresponding dispersive displacement matrices $\mathbf{B_1}$ (soil) and $\mathbf{B_2}$ (aquifer) are given for the three-dimensional case according to Eq. 2.4, as

$$\mathbf{B}_1 = \begin{pmatrix} 0 & 1 & -1 \\ 0 & 1 & 1 \\ -\sqrt{20} & 0 & 0 \end{pmatrix} \text{ and } \mathbf{B}_2 = \begin{pmatrix} \sqrt{20} & 0 & 0 \\ 0 & 0 & \sqrt{2} \\ 0 & \sqrt{2} & 0 \end{pmatrix}. \tag{2.15}$$

In this example, we only consider the interface between the two layers, thus, dimensions and boundary conditions are not relevant. Dispersive displacements in the direction perpendicular to the interface of particles in the upper layer depend only on the first entry of the random vector $\boldsymbol{\xi}$, ξ_1 (Eq. 2.3). Because the probability that a particle reaches the interface by a dispersive displacement during a single time step Δt is increased with positive, high random number, the subset of random vectors $\boldsymbol{\xi_{sub}}$ leading to a displacement to the interface will be characterized by $\bar{\xi}_{sub,1} > \bar{\xi}_{sub,2} = \bar{\xi}_{sub,3} = 0$, where the overbar refers to the mean value of the subset of random numbers. Dispersive displacements perpendicular to the interface of particles in the lower layer depend only on the second entry of $\boldsymbol{\xi}$, ξ_2. Since the dispersive displacement in the z-direction in the upper layer does not depend on ξ_2, $\bar{\xi}_{sub,2}$ is 0. Using the same set of random numbers for the second part of the displacement in the lower layer halve of the particles that are allowed to pass, i. e. the ones with $\bar{\xi}_{sub,2} > 0$, will be displaced back into the upper layer resulting in a bias of the particle distribution. Additionally $\bar{\xi}_{sub,1} > 0$ will lead to a positive mean of dispersive displacements in the horizontal direction in the lower layer, which is implausible because the mean of these dispersive displacements is supposed to be 0.

This simple example illustrates that the set of random numbers that led to a displacement to the interface in the first layer needs to be modified in order to calculate the dispersive displacement in the second layer in a correct manner. A better solution is obtained if the total displacements resulting form the random numbers in the first element are used as a basis to calculate the displacements in the second element. We first treat the displacements in the direction perpendicular, $i = j$, to the interface and afterwards the displacements parallel to the interface, $i \neq j$ (with $i = x, y, z$ and $j = x, y, z$; the direction j is perpendicular to the interface).

With $\Delta\mathbf{X}_1^*$ we denote the remaining dispersive displacement vector after the

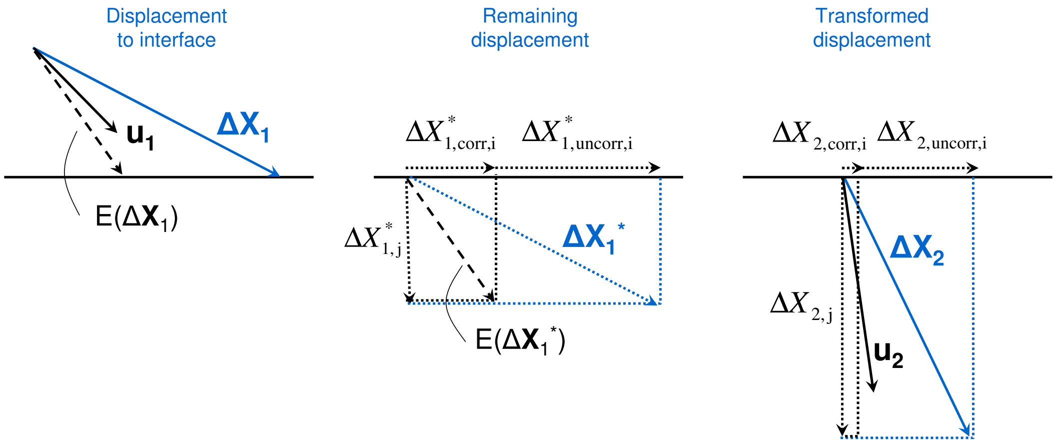

Figure 2.2: Transformation of dispersive displacement, schematically shown in two-dimensional for $\alpha_L > \alpha_T > 0$. Left: A particle performs the random dispersive displacement $\Delta\mathbf{X}_1$ and reaches the interface after $0.5\Delta t$. Note that the expected direction of dispersive displacements reaching the interface during a single Δt, E($\Delta\mathbf{X}_1$), is not parallel to the direction of the velocity $\mathbf{u}_1$. Center: The remaining displacement based on the properties of the first element, $\Delta\mathbf{X}_1{}^*$, has a component perpendicular and components parallel to the interface. The latter can be split into a correlated and uncorrelated part. Right: The individual components of $\Delta\mathbf{X}_1{}^*$ are transferred to a dispersive displacement in the second element, $\Delta\mathbf{X}_2$, applying Eq. 2.16 to 2.25. For further details see Section 2.2.2.3.

particle already performed the displacement $\Delta\mathbf{X}_1$ to reach the element interface (Fig. 2.2). It can be calculated from

$$\Delta X^*_{1,i} = \Delta X^*_{total,i} - \Delta X_{1,i} \tag{2.16}$$

where $\Delta X^*_{total,i}$ is the total dispersive displacement calculated using the full time step Δt at the starting location of the particle with the random number vector $\boldsymbol{\xi}$. $\Delta X^*_{1,i}$ and $\Delta X_{1,i}$ are related to the correct, non-linearly split times Δt_1 and Δt_2, as:

$$\Delta X^*_{1,i} = \Delta X_{1,i} \frac{\sqrt{\Delta t_2}}{\sqrt{\Delta t_1}} \tag{2.17}$$

For the direction $i = j$, the displacement in the second element, $\Delta X_{2,j}$, is calculated using a simple scaling according to Eq. 2.6,

$$\Delta X_{2,j} = \frac{\sqrt{D_{2(j,j)}}}{\sqrt{D_{1(j,j)}}} \Delta X^*_{1,j} \tag{2.18}$$

where $\mathbf{D}_1$ and $\mathbf{D}_2$ are the dispersion tensors in the first and second element according to Eq. 2.2. Note that Eq. 2.18 describes a particle displacement away from the element interface into the second element which is consistent with the definition of the reflection coefficient.

As stated above, the probability that a particle reaches the interface during Δt increases with higher values for the displacement in the direction j. As a consequence, the expected value of all displacements in direction j of all particles that reach the interface within time step Δt is larger than zero in the first, $\mathrm{E}(\Delta X_{1,j}) > 0$, and second, $\mathrm{E}(\Delta X_{2,j}) > 0$, element. Due to off-diagonal terms in the dispersion tensor $\mathbf{D}$ (Eq. 2.2) that are different from zero, the displacements in the direction parallel to the interface are correlated to the displacements in the direction perpendicular to the interface; thus, $\mathrm{E}(\Delta X_{1,i}) \neq 0$ and $\mathrm{E}(\Delta X_{2,i}) \neq 0$. Because the direction of the flow vector and the dispersivities change across the interface, the off-diagonal terms in $\mathbf{D}$ and hence the correlation between the displacement in the direction perpendicular and parallel to the interface changes across the interface.

To avoid a bias in the particle movements in the second element the correlation between the dispersive displacements parallel and perpendicular to the interface in the two elements must be accounted for appropriately. For any displacement, the expected value of the displacement in direction i, $\Delta X_{1,corr,i}$ that is conditioned on the displacement in direction j, $\Delta X_{1,j}$ is obtained as

$$\Delta X_{1,corr,i} = \frac{D_{1(i,j)}}{D_{1(j,j)}} \Delta X_{1,j} \tag{2.19}$$

Thus the remaining correlated displacement $\Delta X^*_{1,corr,i}$ is

$$\Delta X^*_{1,corr,i} = \frac{D_{1(i,j)}}{D_{1(j,j)}} \Delta X^*_{1,j} \tag{2.20}$$

Similarly, $\Delta X_{2,corr,i}$ is the expected displacement in direction i in the second element that is conditioned on the displacement in direction j, and can be obtained as,

$$\Delta X_{2,corr,i} = \frac{D_{2(i,j)}}{D_{2(j,j)}} \Delta X_{2,j} \tag{2.21}$$

Using Eq. 2.18, we obtain:

$$\Delta X_{2,corr,i} = \frac{D_{2(i,j)}}{\sqrt{D_{2(j,j)}}\sqrt{D_{1(j,j)}}} \Delta X^*_{1,j} \tag{2.22}$$

Note that for $i = j$, Eq. 2.22 simplifies to Eq. 2.18.

After passing the correlated components, the uncorrelated components of the displacements in the different directions are transferred to the second element. The expected value of the uncorrelated displacement for $i \neq j$ is zero. The uncorrelated component, $\Delta X^*_{1,uncorr,i}$, is the difference between the total remaining displacement in direction i and the displacement that is correlated to the displacement in direction j,

$$\Delta X^*_{1,uncorr,i} = \Delta X^*_{1,i} - \Delta X^*_{1,corr,i} \tag{2.23}$$

As the uncorrelated displacement $\Delta X_{2,uncorr,i}$ is only a part of the total displacement in direction i, the scaling from Eq. 2.18 has to be corrected for the already treated correlated displacement. According to conditional statistics, $\Delta X^*_{1,uncorr,i}$ is scaled by the ratio of the standard deviations of the uncorrelated displacements,

$$\Delta X_{2,uncorr,i} = \Delta X^*_{1,uncorr,i} \frac{\sqrt{D_{2(i,i)} - \left(\frac{D_{2(i,j)}}{\sqrt{D_{2(j,j)}}}\right)^2}}{\sqrt{D_{1(i,i)} - \left(\frac{D_{1(i,j)}}{\sqrt{D_{1(j,j)}}}\right)^2}} \tag{2.24}$$

For the direction j, it follows that $\Delta X_{2,uncorr,j} = 0$. The displacement in direction $i \neq j$ in the second element is the sum of the correlated and uncorrelated displacement components,

$$\Delta X_{2,i} = \Delta X_{2,corr,i} + \Delta X_{2,uncorr,i} \tag{2.25}$$

If the transport problem is one-dimensional or if the $\mathbf{B_2}$ is linearly related to $\mathbf{B_1}$, the proposed transformation scheme coincides with a solution using the same set of random numbers for displacements in the first and second element and the new non-linear time splitting with $\Delta\mathbf{X}_2 = \xi\mathbf{B}_2\sqrt{\Delta t_2}$ (see Eq. 2.9 and 2.17).

When a particle is reflected at an interface or domain boundary a point reflection at the interception point of displacement vector and interface must be performed (the whole remaining displacement vector is inverted). When reflecting solely the displacement component perpendicular to the interface (surface reflection), anisotropic dispersion tensors would be systematically distorted which leads to significant errors.

2.3 Materials and methods

2.3.1 Numerical implementation of the improved reflection barrier method

For the calculation of the reflection probabilities, the dispersion coefficients and water contents on both sides of the interface are necessary. In the case of anisotropic dispersion tensors, the component corresponding to the direction orthogonal to the interface has to be used, as it determines the probability that a particle reaches the interface. As our implementation was restricted to rectilinear grids we used the corresponding diagonal component of $\mathbf{D}$. However, other choices are possible (e. g. a vector norm for the corresponding row vector of the dispersion tensor). For simulated flow field solutions, in which the velocity vector is continuously changing in space, it is important to calculate the reflection coefficient by taking the limits of the properties (velocity, dispersivity, diffusion coefficient and water content) from both sides directly at the interface to guarantee that there is no reflection when the dispersion tensor and the water content is steady over the interface. Continuous changes of the dispersion tensor are considered already in the advective term of Eq. 2.3 and should not affect the value of the reflection coefficient.

In previous studies, it has been reported that particles crossing different interfaces by dispersive displacements during the same time step Δt is a major problem for the application of the reflection barrier method to complex multidimensional transport problems (e. g., LaBolle et al., 1996; Salamon et al., 2006). We used the simplest approach to treat particles which cross multiple interfaces during one time step. At each interface a particle reaches by dispersive movement, the reflection coefficient is calculated and a new random number is generated to decide whether the particle is reflected or allowed to pass. The subsequent dispersive displacement is then calculated based on the proposed transformation of the dispersive displacement. Following this procedure the dispersive displacements are performed until the particle does not reach another interface within the remaining time. In this simple approach we do not superimpose multiple reflections to calculate the transition probability at a single interface, which has been considered to be the main reason for the problems with the application of the reflection barrier method to complex multi-dimensional scenarios. As will be demonstrated later, this works well as the proposed new transformation of the dispersive displacement allows a transfer of the remaining dispersive displacement from the first element to the second element at each interface without introducing a significant bias to the displacement in the second element.

For the reflection barrier method in general, a splitting approach has to be used for the advective and dispersive displacements across discontinuities. First the advective displacement is calculated with a linear time splitting $\Delta t = \Delta t_1 + \Delta t_2$, then the dispersive displacement is applied with the non-linear time splitting $\sqrt{\Delta t} = \sqrt{\Delta t_1} + \sqrt{\Delta t_2}$ for scalar dispersion coefficients or the transformation of the dispersive displacement for dispersion tensors. The reflection principle must only be applied when a particle reaches an interface in the dispersion step.

The different types of reflection coefficients and time splitting schemes, the transformation procedure of the dispersive displacement, and the interpolation method were implemented in the RWPT code PARTRACE (Neuendorf, 1997). PARTRACE simulates three-dimensional transport of conservative and reactive solutes in saturated and unsaturated porous media for given velocity fields by applying the stochastic differential equation given in Eq. 2.3 to a high number of particles. The dispersive displacement matrix $\mathbf{B}$ of Eq. 2.3 is calculated as given in Eq. 2.4. PARTRACE is a modular c++ code, capable of handling regular and irregular grids, and parallelized for the use on massive parallel supercomputers.

2.3.2 Numerical verification of improved reflection barrier method

To verify the three improvements of the proposed RWPT algorithm, we performed numerical simulations of conservative solute transport in specific test scenarios. Two different test scenarios are considered. The first scenario, S1, is a simplified transport problem for which an analytical solution exists. For this test scenario a basic version of the proposed algorithm can be used that only uses the first two improvements (non-linear time splitting and one-sided reflection scheme). Although this test case

Table 2.1: Overview of options of the reflection barrier method applied to the scenarios S1 to S2.

Option		Abbreviation
Reflection Coefficient		
Lim (2006)	two-sided (with water content)	R1
This study	one-sided (with water content)	R2
Time Splitting		
Hoteit et al. (2002)	$\Delta t = \Delta t_1 + \Delta t_2$	TS1
This study	$\sqrt{\Delta t} = \sqrt{\Delta t_1} + \sqrt{\Delta t_2}$	TS2
Transformation of Dispersive Displacement		
Hoteit et al. (2002)	no transformation applied	DT0
This study	transformation, Eq. 2.16 to 2.25	DT1

seems very simple, it is absolutely essential, as it is not possible to clearly differentiate between the effects of the individual improvements in complex three-dimensional test cases.

In the second scenario, S2, we applied the improved reflection barrier method to a complex three-dimensional, unsaturated transport problem based on a computed velocity field and compared the results with the ones obtained from the interpolation method, abbreviated by I (Table 2.1). We used a material distribution created by a Sequential Indicator Algorithm, which is the most demanding type of parameter heterogeneity for RWPT algorithms according to Salamon et al. (2006). The finite volume or finite difference solution of the water flow problem computed for such a scenario is characterized by many abrupt changes of the dispersion tensor and of the water contents that occur at element interfaces.

All scenarios were simulated using the two different reflection coefficients, R1 and R2 (see Fig. 2.1), and using the linear, TS1 as well as the corrected time splitting, TS2. Scenario S2, where a transformation of the dispersive displacement is required, was additionally simulated without (DT0), i. e. $\Delta \mathbf{X}_2 = \xi \mathbf{B}_2 \sqrt{\Delta t_2}$, and with (DT1) performing the proposed dispersive displacement transformation (for overview of options see Table 2.1).

The amount of particles used are indicated for each scenario and were chosen to minimize the fluctuations of the solution to an acceptably low value while obtaining a computational speed high enough for a spatial and temporal convergence analysis on the available computation cluster. For scenario S2 an analysis of the convergence as function of the particle number was performed as well.

2.4 Test scenarios

2.4.1 Test scenario S1

2.4.1.1 Problem description

This two-dimensional scenario of transport in a two-layer stratified aquifer was adopted from Salamon et al. (2006). Using this scenario, they compared the interpolation method, the GSDE method and the reflection barrier method. The results indicated significant discrepancies between the methods and the analytical solutions for this test scenario which are given by Marle et al. (1967). We kept the settings as presented in Salamon et al. (2006) to maintain comparability with their results (see also Fig. 2.3 for a schematic overview). The domain size was 10000 m in x-direction (horizontal) and 0.3 m in y-direction (vertical) with a regular discretization of 100×30 elements and reflection boundary conditions at the top and bottom domain boundary. The extreme ratio of horizontal to vertical extent was chosen by Salamon et al. to highlight the differences between the methods. Both layers had a thickness of 0.15 m and a porosity of $\theta = 0.2$. Steady-state water flow was horizontal from left to right. The velocity in the lower layer was $u_{x,2} = 43.2$ m d^{-1}, and the velocity in the upper layer, $u_{x,1}$, ranged in different scenarios from 43.2 m d^{-1} to 0.043 m d^{-1} covering ratios $u_{x,2}/u_{x,1}$ between 1 and 1000. The dispersion in the layers was assumed to be isotropic and the dispersion coefficient was calculated from the pore water velocity using $D = \alpha u$ with α being the dispersivity (0.01 m). A Dirac pulse was uniformly injected in y-direction at time $t = 0$ d (6×10^3 particles), sufficiently far away from the left domain boundary to assure that no particles would be affected by the left boundary condition. We analyzed the transport results by applying the method of moments (Aris, 1956) as done in Salamon et al. (2006). The first three spatial moments were calculated for the x-direction directly from the particle locations by the equations:

$$M_0(t) = n m_{par} \tag{2.26}$$

$$M_x(t) = \frac{m_{par}}{M_0(t)} \sum_{i=1}^{n} X_{x,i}(t) \tag{2.27}$$

$$M_{xx}(t) = \frac{m_{par}}{M_0(t)} \sum_{i=1}^{n} X_{x,i}^2(t) - M_x^2(t) \tag{2.28}$$

where n is the number of particles, m_{par} is the particle mass, $X_{x,i}(t)$ is the position of the particle i in the x-direction at time t. M_0 represents the total solute mass (kg), M_x represents the position of the center of mass in the x-direction (L) and M_{xx} represents the spreading of the plume in the x-direction (L^2). The location of the

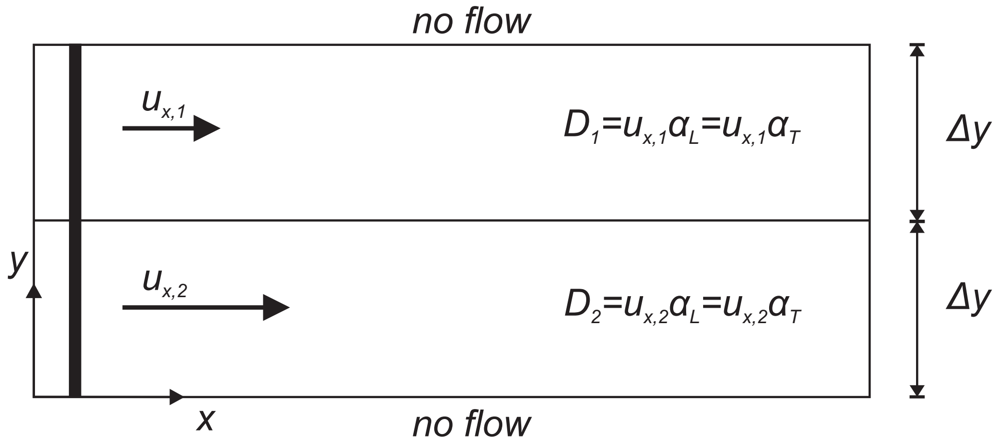

Figure 2.3: Schematic overview of scenario S1 which was adopted from Salamon et al. (2006). Details and parameters are presented in the scenario description.

center of mass and the plume spreading in the y-direction are obtained by replacing the $x-$ by the y-coordinate in the equations above.

The apparent average velocity $U(t)$ and the apparent longitudinal macrodispersion $D_L(t)$ can be derived from the moments,

$$U_x(t) = \frac{M_x(t) - M_x(0)}{t} \tag{2.29}$$

$$D_L(t) = \frac{1}{2}\frac{M_{xx}(t) - M_{xx}(0)}{t} \tag{2.30}$$

Numerical results of the location of the center of mass in z-direction and longitudinal macrodispersion $D_L(t \to \infty)$ were compared with analytical solutions (Marle et al., 1967). The only differences to the simulations of Salamon et al. (2006) is that we extended the domain in the x-direction from 1000 to 10000 m and that we calculated the longitudinal macrodispersion for $t = 200$ d. The reason for these modifications is that the spatial and time dimensions used in Salamon et al. (2006) were not sufficient to assume $D_L(t \to \infty)$ for the most extreme scenario with the velocity ratio $u_{x,2}/u_{x,1} = 1000$.

2.4.1.2 Results and discussion

Existing reflection schemes can lead to deviations between numerical results and analytical solutions in well-defined test scenarios (e. g., Salamon et al., 2006). The results for test scenario S1 demonstrate that the non-linear time splitting already corrects for part of these deviations (Fig. 2.4a). We reproduced similar deviations as observed in Salamon et al. (2006) by applying the wrong time splitting and the two-sided reflection scheme which shifted the center of mass in y-direction to the low dispersion layer.

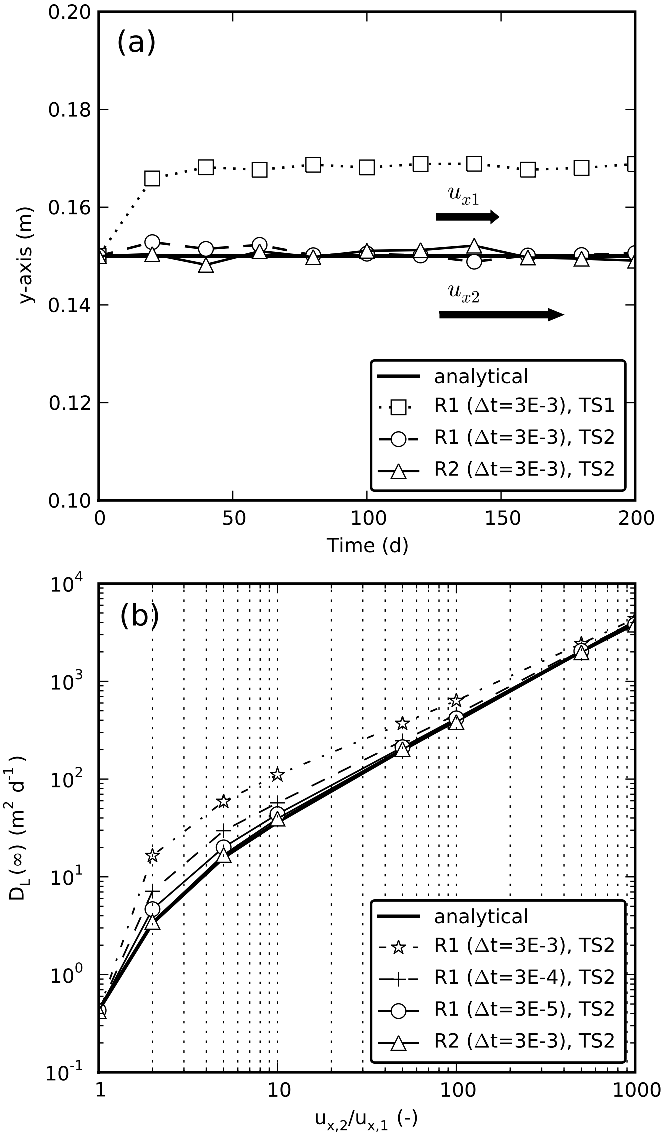

Figure 2.4: Scenario S1. (a) Location of the center of mass in y-direction (m) vs. time (d) for $u_{x,2}/u_{x,1} = 1000$. (b) Longitudinal macrodispersion $D_L(t \rightarrow \infty)$ as a function of increasing heterogeneity $u_{x,2}/u_{x,1}$. Reflection coefficients R1: Lim (2006) and R2: one-sided reflection scheme; Time Splitting TS1: $\Delta t = \Delta t_1 + \Delta t_2$ and TS2: $\sqrt{\Delta t} = \sqrt{\Delta t_1} + \sqrt{\Delta t_2}$.

The application of the non-linear time splitting TS2 is sufficient to predict the center of mass in y-direction correctly; however the spreading in the x-direction, i. e. the longitudinal macrodispersion, is not accurately simulated for higher Δt when applying TS2 in combination with the two-sided reflection scheme R1. Redundant reflections in the two-sided reflection scheme cause two errors: (1) they decrease the exchange between the two layers and (2) cause a retarded transversal spreading of the particles entered in layer 1 or 2. Both biases affect the accuracy of the longitudinal dispersion (Fig. 2.4b). The improved one-sided reflection scheme R2 provided very accurate results also for large time steps as the error related to the reflection barrier method was then limited to a reduced number of particle reflections at the single material contrast between layer 1 and 2 (Fig. 2.4b). The results that are obtained even with large time steps when using the non-linear time splitting TS2 and the one-sided reflection scheme R2 are fully consistent with the analytical solution and more accurate than all results presented in the comparative study of Salamon et al. (2006) for this test scenario with the interpolation, the GSDE, the reflection and the total variation diminishing scheme.

2.4.2 Test scenario S2-1 and S2-2

2.4.2.1 Problem description

The scenarios S2-1 and S2-2 were chosen to demonstrate the general applicability of the improved reflection barrier method to more complex three-dimensional transport problems. In these scenarios, the RWPT algorithm has to deal with complexities such as: (1) a heterogeneous flow field, (2) a continuously and discontinuously spatially changing anisotropic dispersion tensor, (3) eigenvectors of $\mathbf{D}$ oriented oblique to the interface, (4) spatially varying water content and (5) multiple reflections during a single time step Δt. To analyze whether the proposed improvements to the reflection barrier method, i. e. the non-linear time splitting TS2 and the one-sided reflection scheme R2, also lead to improvements in complex problems, the transport of a tracer pulse was considered (scenario S2-1). In the scenarios S2-1 and S2-2, we further analyzed how the transformation of the dispersive displacement improves the accuracy of the results.

The water flow and the water content were simulated for a constant flux boundary condition of 1×10^{-3} m d^{-1} at the top surface of a three-dimensional heterogeneous unsaturated porous medium. The porous medium corresponds to an experimental setup at the Agrosphere Institute in Jülich that consists of a $0.875 \times 0.875 \times 0.8317$ m^3 heterogeneously filled sank tank. The tank was filled with rectangular blocks ($15 \times 15 \times 14$ blocks, see Fig. 2.5) of three different sandy materials (here called fine-, medium- and coarse-grained; the hydraulic properties are given in Table 2.2). To analyze how the efficiency of the algorithm depends on the variance of the hydraulic parameter field, we created two additional hydraulic parameter sets for the scenario

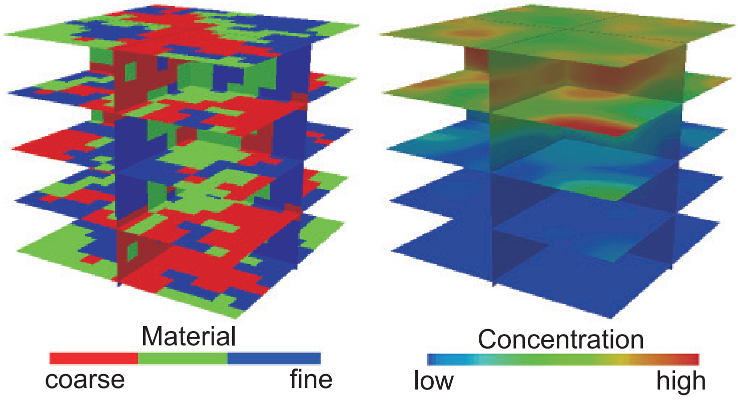

Figure 2.5: Left: Trimodal correlated indicator field used as hydraulic parameter field for scenario S2. Right: Solute distribution of scenario S2-1 at time t = 17 d after a Dirac pulse tracer injection at the soil surface under infiltration conditions.

S2-1 and S2-2 with a lower and a higher variability applying the concept of Miller-similarity scaling (Miller and Miller, 1956). The hydraulic parameters with the lower variability were obtained by dividing the saturated conductivity K_s and the van Genuchten-Mualem parameter α of the coarse material by 3 and $\sqrt{3}$, respectively, and multiplying K_s and α of the fine material by 3 and $\sqrt{3}$, respectively. The hydraulic parameters with the higher variability were obtained by multiplying K_s and α of the coarse material by 3 and $\sqrt{3}$, respectively, and dividing K_s and α of the fine material by 3 and $\sqrt{3}$, respectively. The variances of $\ln(K_s)$ of the three resulting parameter fields are 0.88, 4.2 and 21.2 and the variances of the water content θ are 0.0018, 0.006 and 0.013. We will further refer to them as low, intermediate and high parameter variability.

The arrangement of the blocks was generated using an indicator random field generator SISIM, which is part of the Geostatistical Software Library (GSLIB) (Deutsch and Journel, 1998). The 1.5 cm bottom layer is composed of the fine material only. The lower boundary condition was a constant pressure of -2.5 hPa. No-flow boundary conditions were used at the sides of the tank.

The flow field was simulated using Richards' equation (Richards, 1931). The equation was solved using a cell-centered finite-volume (FV) scheme on rectilinear grids with full-upwinding of relative permeability in space for stabilization. An implicit Euler scheme was used for the time discretization. Linearization of the non-linear equations is done by an inexact Newton-Method with line search. The linear equations are solved with an algebraic multigrid solver. The time step is automatically adapted by the time solver. The flow field was interpolated using RT0 Raviart Thomas elements (Raviart and Thomas, 1975; Brezzi and Fortin, 1991). The numerical code was tested with analytical solutions and successfully applied in several studies (e. g., Ippisch et al., 2006; Samouelian et al., 2007; Rossi et al., 2008; Carminati and Flühler, 2009; Haber-Pohlmeier et al., 2010).

Table 2.2: Van Genuchten-Mualem parameters of materials in S2: $\theta_r =$ residual water content, $\theta_s =$ saturated water content, $K_s =$ saturated conductivity; α, n and $\tau =$ shape parameters).

	θ_r(m^{3}m^{-3})	θ_s(m^{3}m^{-3})	K_s(cm d^{-1})	α(cm^{-1})	n(-)	τ(-)
coarse	0.05	0.41	2496	0.0177	10.8	0.73
medium	0.06	0.36	408	0.0121	5.3	-0.01
fine	0.07	0.35	48	0.0055	3.5	0.66

Differences between the hydraulic properties of the sand blocks led to a highly heterogeneous flow field and large water content variations in the soil profile - ranging from 0.06 to 0.41. In both scenarios S2-1 and S2-2, an anisotropic dispersion tensor was defined. The longitudinal and transversal dispersivities were set to 0.1 m and 0.02 m respectively for all three materials and the molecular diffusion coefficient was assumed to be zero.

In scenario S2-1 a Dirac pulse (1×10^6 particles) was injected at $t = 0$ d at the soil surface into the simulated steady-state flow field. Both the concentration of the irrigated water and the initial concentration of pore water before the injection were 0 kg m^{-3}. In S2-1, we compared the spatial moments of the concentration distributions after 17 d (Fig 2.5, Eq. 2.26 and 2.30) that were obtained with the different particle tracking methods.

Scenario S2-2 served as a test whether the improved reflection barrier method is able to maintain constant concentration in such a transport problem when the system is continuously flushed with the same concentration. The initial concentration was set to $C_0 = 1$ kg m^{-3}, i. e. particles were heterogeneously injected depending on the water content (in total 7.5×10^6 particles, each having a mass of approximately 2.7×10^{-8} kg). The concentration of the irrigated water also had a concentration of $C = 1$ kg m^{-3}, to maintain the amount of particles necessary to preserve a constant and homogeneous concentration of $C(\mathbf{X}, t) = 1$ kg m^{-3}. As performance measure, we compared the simulated concentrations of the $15 \times 15 \times 15$ cells each representing a material block with the true, constant concentration of 1 kg m^{-3} by calculating the RMSE of all elements,

$$\text{RMSE} = \sqrt{\frac{\sum_i (C(\mathbf{X}, t) - C_0)^2}{n_{elements}}} \tag{2.31}$$

The RMSE error was calculated at $t = 10$ d when the RMSE error reached a steady-state in all cases. As a reference, we calculated the RMSE that can be expected from a RWPT simulation with the applied number of particles. In this calculation, we assumed that the particles were randomly distributed over the domain cells so that the concentration is uniform. Thereby, the probability that a particle is placed in a specific element depends on the volume and water content of this element (for details see Appendix A).

The interpolation method was implemented using the ‘hybrid’ scheme described above (LaBolle et al., 1996). The improved reflection barrier method was compared with the interpolation method by performing a spatial and temporal convergence analysis. As stated above, RWPT is principally a grid-free method; however, grids are needed to represent the spatial variation of the variables governing the particle motion (here: velocity, dispersion tensor and water content) and calculate these variables at the particle location by interpolation. The input to all RWPT simulations was the steady-state flow field computed on the coarsest grid ($15 \times 15 \times 15$ elements). Different grids were then applied in the RWPT algorithm to interpolate the variables. The coarsest grid we used for the RWPT simulations was equal to the one of the flow solution and consisted of $15 \times 15 \times 15$ elements (3375 elements), each element representing one material cube (including the homogeneous bottom layer). For the spatial convergence analysis, the grid was gradually refined by doubling the number of cells in each direction during one refinement step. In the following, we refer to the different refined grids with the refinement factor k, which is the number of subdivisions along each axis of the element of the coarsest grid. The finest grid consisted of $120 \times 120 \times 120$ elements (1.7×10^6 elements, grid refinement factor $k = 8$). The particle positions obtained from the RWPT simulations were always used to map the solute concentration to the coarsest grid, so that all results were compared at the same resolution.

For the temporal convergence analysis, we applied time step sizes ranging from $\Delta t = 0.001$ to 1.0 d. To focus on the accuracy of the dispersive displacements in the temporal convergence analysis, we minimized the effect of different time step sizes on the calculation of the advective term of Eq. 2.3 by implementing the analytical velocity integration after Pollock (1988) and Schafer-Perini and Wilson (1991), which is exact for a linearly varying velocity field as provided by the FV solution. Here, for simplicity only written for the x-direction,

$$X_x - X_{x,0} = \frac{a + b(X_{x,1} - X_{x,0})}{b} \exp(b\Delta t) - \frac{a}{b} \tag{2.32}$$

using the velocity interpolator within one element from the FV solution,

$$u_{x,1} = a + b(X_{x,1} - X_{x,0}) \tag{2.33}$$

where X_x is the new particle location after time Δt, $X_{x,1}$ is the initial particle location, $X_{x,0}$ is the coordinate of the left side of the element, a and b are variables of the velocity interpolation using the RT0 Raviart Thomas elements, and $u_{x,1}$ is the velocity at the initial particle coordinates $X_{x,1}$. The velocity of a particle that leaves the element during Δt was updated at the interception point, the time was split linearly $\Delta t = \Delta t_1 + \Delta t_2$ and the second displacement was performed with the updated velocity and the remaining time Δt_2.

2.4.2.2 Results and discussion

Simulations from applying different combinations of options for the reflection barrier method were compared for S2-1 and the intermediate parameter variability (Fig. 2.6). The results indicate that all methods converge to similar calculated first and second moments with decreasing time step size. The use of a two-sided reflection scheme R1 leads to a higher apparent average velocity and a smaller longitudinal macrodispersion compared to the one-sided reflection scheme R2, especially for larger time steps. The linear time splitting scheme TS1 results in a lower apparent average velocity and a higher longitudinal macrodispersion than the non-linear time splitting scheme TS2, also more pronounced for larger time steps. The largest initial deviations occurred when applying both R1 and TS1. When the two-sided reflection scheme R1 was used with the correct time splitting TS2, the trend is the same, the observed errors were a bit lower but the effects did not completely compensate. The best results with large time steps and the fastest convergence were obtained when both improvements, R2 and TS2 were applied. The application of the transformation of the dispersive displacement, in the following called DT1, shifted the apparent average velocity to higher values compared to the combination of R2 and TS2, the apparent longitudinal macrodispersion was almost identical, convergence was even faster.

To evaluate the accuracy of these results, a comparison with a reference numerical method, here, the interpolation method was performed. There is general agreement that the interpolation method converges to the true solution when refining grid and time step size simultaneously. The comparison between improved reflection barrier and interpolation method served to evaluate whether the results of the improved reflection barrier method are reliable also for complex 3-D transport problems. This comparison was performed for all three parameter fields. Fig. 2.7 shows that the results of the apparent average velocity and the apparent longitudinal macrodispersion obtained from the interpolation method converged for the low and intermediate parameter variability when simultaneously decreasing grid size and time step. In these cases, the interpolation method converged to a solution that is consistent with the solution to which the reflection barrier method was converging when applying R2 and DT1. By neglecting the transformation of the dispersive displacement (DT0), the reflection barrier method did not converge to the same solution. This demonstrates the improvement achieved by the transformation of the dispersive displacement. The improved reflection barrier method was practically independent of the grid size (Fig. 2.7). For highest parameter variability, the interpolation method apparently did not converge with the finest grid and smallest time step size, in contrast to the reflection barrier method. The results of the interpolation method indicate that a further grid refinement and time step size reduction probably provides results that approach the ones of the reflection barrier method. However, due to memory limits, a further grid refinement could not be performed.

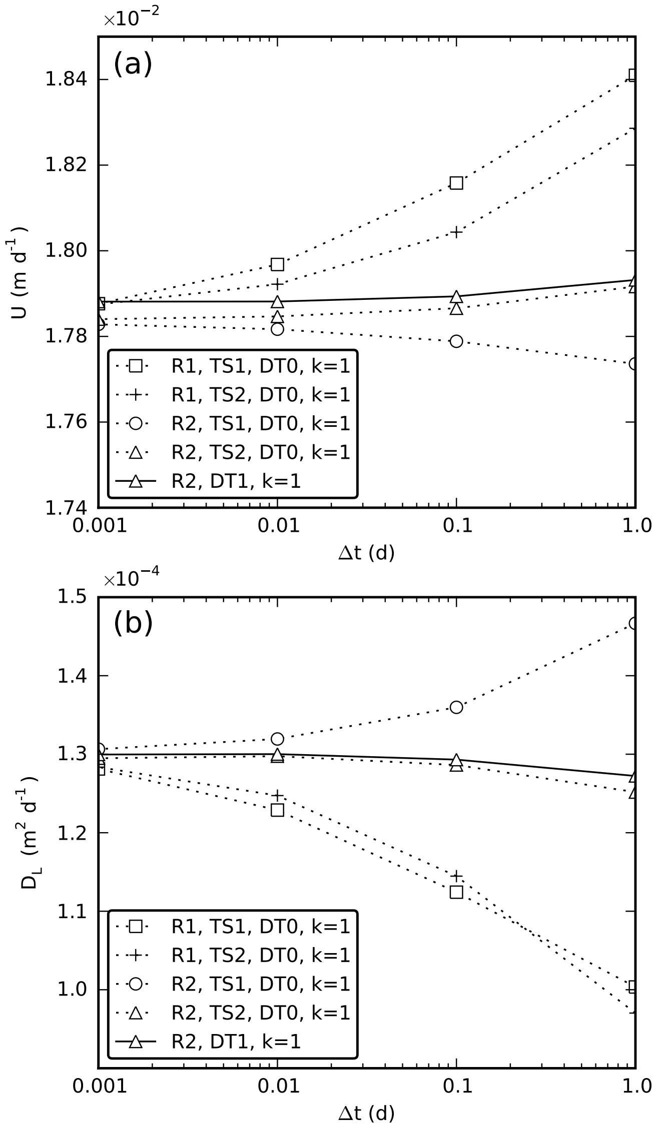

Figure 2.6: Scenario S2-1, apparent average velocity U, (a), and apparent longitudinal dispersion D_L, (b), as a function of applied time step size for the coarsest grid (no grid refinement, refinement factor $k=1$) at time $t=17$ d. Reflection coefficients R1: Lim (2006) and R2: one-sided reflection scheme; Time Splitting TS1: $\Delta t = \Delta t_1 + \Delta t_2$ and TS2: $\sqrt{\Delta t} = \sqrt{\Delta t_1} + \sqrt{\Delta t_2}$; Transformation of dispersive displacement DT0: not applied, DT1: applied, no time splitting necessary.

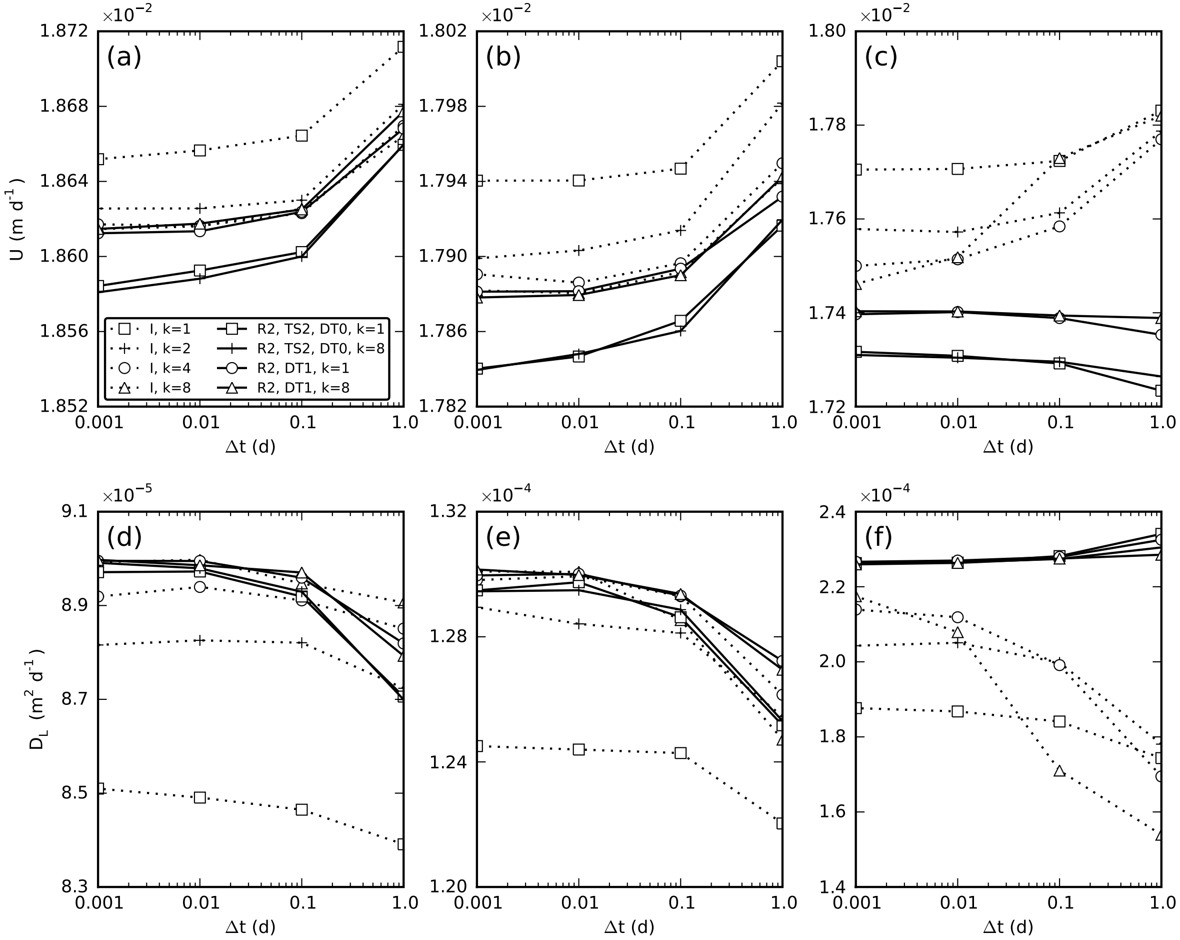

Figure 2.7: Scenario S2-1, apparent average velocity U, (top), and apparent longitudinal dispersion D_L, (bottom), as a function of applied time step size for different grid refinements (refinement factor $k = 1$ to 8, k is the number of subdivisions along each axis of the element of the coarsest grid) and different parameter variabilities (low:(a) and (d), intermediate: (b) and (e), high: (c) and (f)) at time $t = 17$ d. R2: one-sided reflection scheme, and I: Interpolation method; Time Splitting for reflection barrier method TS2: $\sqrt{\Delta t} = \sqrt{\Delta t_1} + \sqrt{\Delta t_2}$; Transformation of dispersive displacement DT0: not applied, DT1: applied, no time splitting necessary.

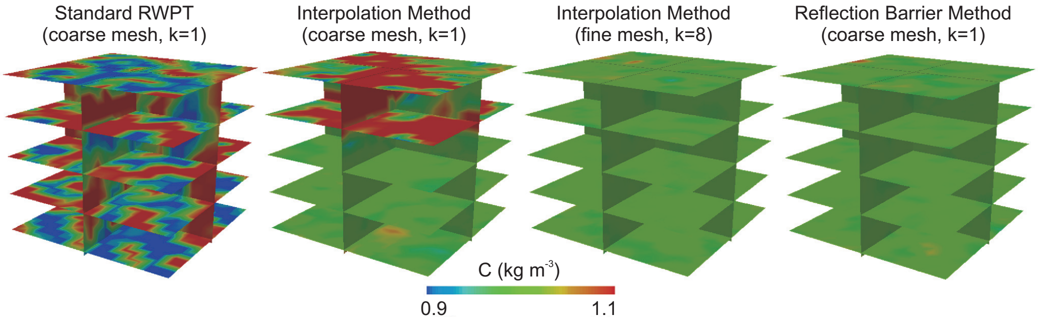

Figure 2.8: Scenario S2-2, constant concentration test. Shown are the solute concentrations at t = 10 d. In this scenario, C is ideally supposed to be homogenously and constantly 1 kg m^{-3}. RMSE error from left to right: 0.79, 0.29, 0.06, 0.03. All scenarios were calculated with the smallest time step size $\Delta t = 0.001$. Refinement factor $k = 1$ to 8, k is the number of subdivisions along each axis of the element of the coarsest grid. The reflection barrier method was applied using the non-linear time splitting TS2, the one-sided reflection scheme R2, and the transformation of the dispersive displacement DT1.

In the last scenario S2-2, it was tested how the improved reflection and interpolation method can maintain a homogenous concentration in a steady-state flux field with advective and dispersive transport. S2-2 represents a classical scenario for which an accumulation of solute in low dispersive regions occurs when a standard RWPT scheme is applied, which neglects discontinuities of $\mathbf{D}$ and θ are not accounted for (Hoteit et al., 2002). We first focus on the results of the intermediate parameter variability. Fig. 2.8 (left) illustrates the high error when neglecting the effect of discontinuous dispersion tensors and applying neither the interpolation nor the improved reflection barrier method ('Standard RWPT'). The calculated root mean squared error (RMSE, see Eq. 2.31) between the simulated concentration and the uniform background concentration ($C = 1$ kg m^{-3}) was 0.77 for the smallest time step. The interpolation method applied on the coarse grid corrected partly these errors (compare Fig. 2.9b), however, especially in the zone where high abrupt water content changes occur, the method has severe problems to maintain the homogenous concentration (RMSE = 0.29 for $\Delta t = 0.001$, Fig. 2.8). For the finest grid, the interpolation method provided acceptable results (RMSE = 0.06 for $\Delta t = 0.001$). The improved reflection barrier provided good results for the coarsest and finest grid (RMSE = 0.03 for $\Delta t = 0.001$), even for the highest time step $\Delta t = 1.0$ (RMSE = 0.06). Only the improved reflection barrier method including DT1 converged to the reference RMSE that could be expected from the applied number of particles (see Appendix A). Both scenarios S2-1 and S2-2 demonstrated that the transformation of the dispersive displacement is required for a proper convergence of the reflection barrier method.

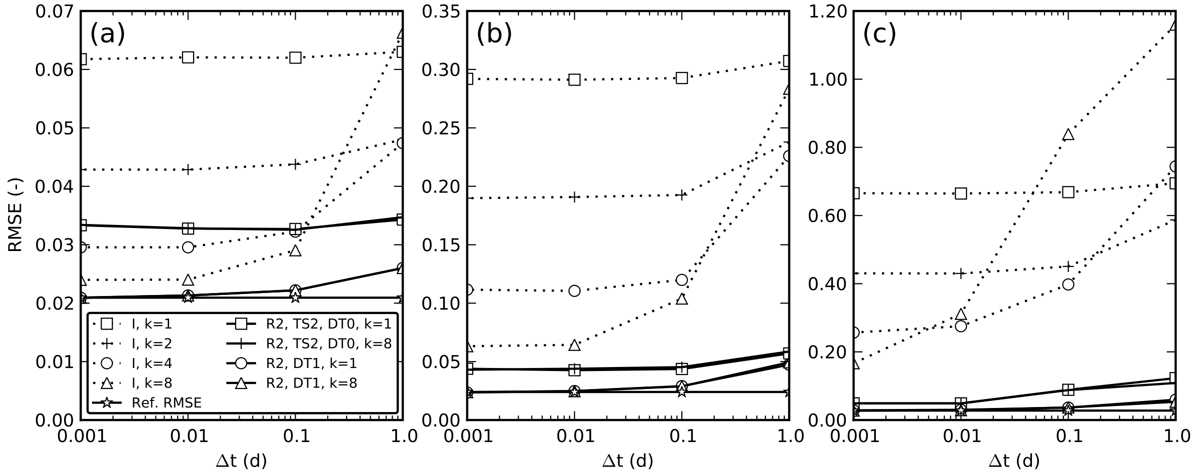

Figure 2.9: Scenario S2-2, RMSE at time t = 10 d of modeled and theoretical concentration $C = 1$ kg m^{-3} calculated from all cells as a function of applied time step size for different grid refinements (refinement factor $k = 1$ to 8, k is the number of subdivisions along each axis of the element of the coarsest grid) and different parameter variability (low: (a), intermediate: (b), high: (c)). R2: one-sided reflection scheme, and I: Interpolation Method; Time Splitting for reflection barrier method TS2: $\sqrt{\Delta t} = \sqrt{\Delta t_1} + \sqrt{\Delta t_2}$; Transformation of dispersive displacement DT0: not applied, DT1: applied, no time splitting necessary.

The results of the lower and higher parameter variability (Fig. 2.9a and 2.9c) show that the RMSE error of both the interpolation and reflection barrier method generally increase with increasing parameter variability. However, the reflection barrier method is much less affected by higher parameter variability than the interpolation method. For the highest parameter variability, both, the grid refinement and the time step reduction are far from being sufficient for the interpolation method to converge to a final solution. In contrast, for the lowest parameter variability, the interpolation method almost converged exactly to the reference RMSE.

The dependency of the solution on the number of particles was evaluated for scenario S2-1 with the intermediate parameter variability, for which both the interpolation and the reflection barrier method converged to the same solution for $\Delta t = 0.001$. Ten model runs ($n_{runs} = 10$) were performed for each of three different numbers of particles ($n = 10^6$, 10^5, 10^4). We then calculated the normalized RMSE of the bulk concentration (mass per unit volume) C_b for the same time at which the apparent velocity and macrodispersion was evaluated before ($t = 17$ d),

$$\mathrm{RMSE}_{\mathrm{normalized}} = \sqrt{\frac{1}{n_{elements}} \sum_i \frac{1}{n_{runs}} \sum_j \left(\frac{C_{b(i,j)}(\mathbf{X}, t)}{\bar{C}_{b(i)}(\mathbf{X}, t)} - 1 \right)^2} \qquad (2.34)$$

where $\bar{C}_{b(i)}$ is the mean concentration of the solution at element i. Fig. 2.10 shows the $\mathrm{RMSE}_{\mathrm{normalized}}$ as a function of the number of applied particles n_{par} for three different bulk concentration ranges. Within a concentration range, the fluctuations of the results of the interpolation and the reflection barrier method depend linearly on the inverse of the square root of the number of particles. Fig. 2.10 further shows that for a specific number of particles, the magnitude of the fluctuations depends on the local concentration, with higher fluctuations where the concentrations are lower. This is the expected behavior for random walk particle tracking algorithms (Kinzelbach and Uffink, 1991).

We also tested if a random vector $\mathbf{Z}$ with a uniform distribution between -1 and 1 can be used instead of the normally distributed random vector $\boldsymbol{\xi}$. However, we found that the transformation of the dispersive displacement is only consistently applicable when using the normally distributed random vector $\boldsymbol{\xi}$. The results from the application of the uniformly distributed and from the normally distributed random vector differ in terms of their mean direction of the dispersive displacements that reach the interface ($\mathrm{E}(\Delta \mathbf{X}_1)$ of Fig. 2.2). Particularly, when using $\mathbf{Z}$ a mean dispersive displacement direction was obtained that differs from the expected correlated part of the dispersive displacement which is in contrast to the theory of the proposed transformation of the dispersive displacement. Although the observed errors were very small in practical applications, we suggest the use of the normally distributed random vector $\boldsymbol{\xi}$ when applying the transformation of the dispersive displacement.

Finally, the effect of neglecting water content variations were analyzed. For

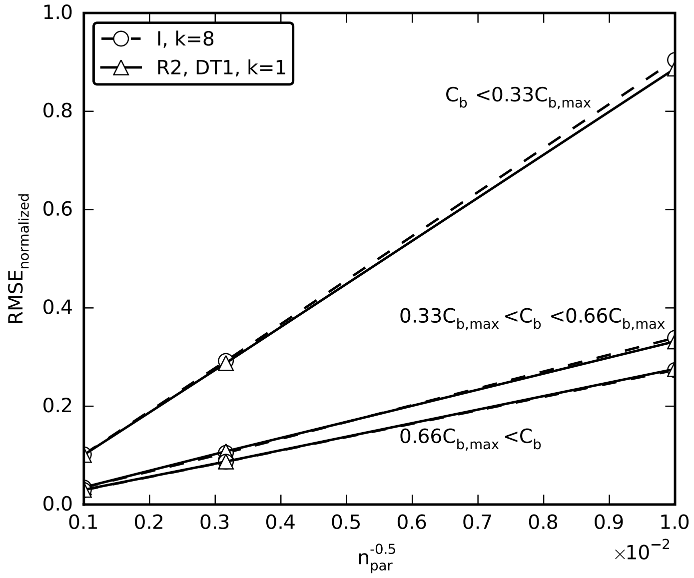

Figure 2.10: Convergence with the number of particles n_{par} for scenario S2-1 and intermediate parameter variability. Normalized RMSE as a function of the inverse of the root of the number of particles for three different bulk concentration ranges, where $C_{b,max}$ is the maximum bulk concentration of the spatial concentration distribution of the true solution. I: Interpolation method, R2: one-sided reflection; DT1: transformation of dispersive displacement applied, no time splitting necessary; k: number of subdivisions along each axis of the element of the coarsest grid.

scenario S2-1 with intermediate parameter variability, simulations were performed using the reflection coefficient of Hoteit et al. (2002) which does not account for water content variations. Based on the results above, we used the proposed improved reflection scheme (R2, DT1) and the interpolation method with the finest grid size (I, $k = 8$) as reference for the true solution. Fig. 2.11 shows the large deviations that occur when water content variations are not considered in the reflection coefficient. This test demonstrates the important improvement proposed by Lim (2006) when applying the reflection barrier method to porous media with varying porosity or water contents.

2.5 Discussion

2.5.1 Convergence to the true solution

In general, RWPT converges with the number of particles, the time step size and in case of the interpolation method also with the resolution of the interpolation grid. The reflection barrier method is independent of the interpolation grid size. Velocity and water content are directly obtained by linear interpolation from the numerical flow solution. The interpolation method introduces an additional error by the interpolation of discontinuities as described in 2.2.1. Convergence to the true solution is obtained by a simultaneous refinement of the interpolation grid and a

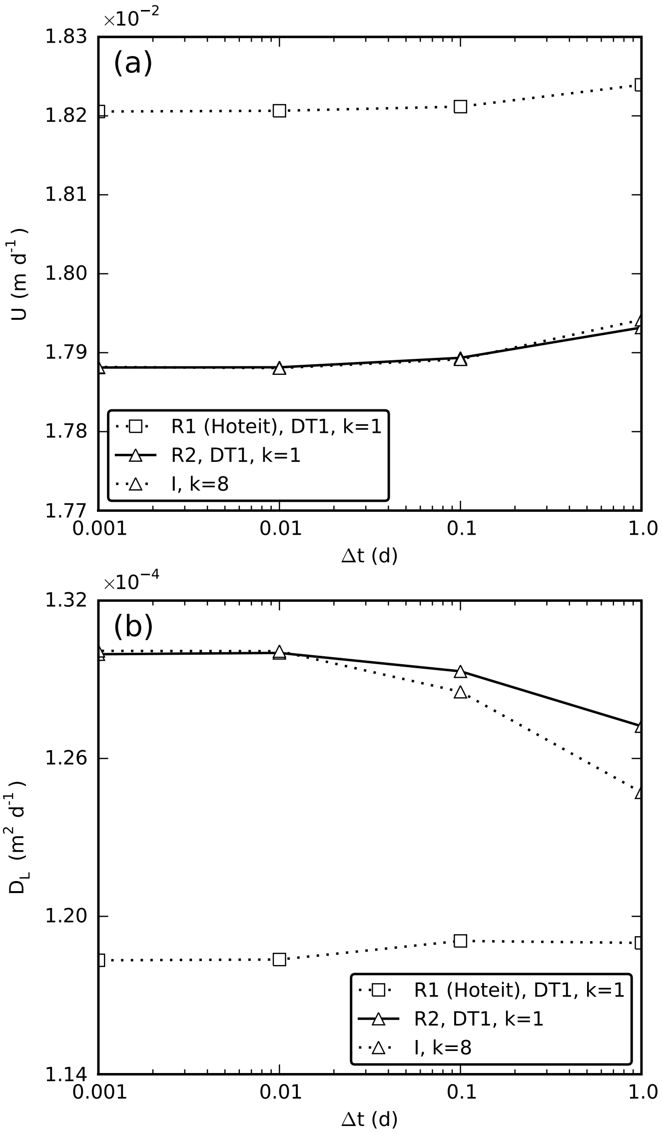

Figure 2.11: Scenario S2-1, (a) apparent average velocity U, and (b) apparent longitudinal dispersion D_L, at time $t = 17\,\mathrm{d}$ as a function of applied time step size. Reflection coefficient R1: Lim (2006), here with the neglecting of water content variations which corresponds to the reflection coefficient of Hoteit et al. (2002), R2: one-sided reflection scheme (this study), and I: Interpolation method; Transformation of dispersive displacement applied (DT1), k: number of subdivisions along each axis of the element of the coarsest grid.

reduction of the time step (LaBolle et al., 1996; Salamon et al., 2006).

The results of both S2-1 and S2-2 are completely consistent with this general behavior. For example, in S2-2 (at intermediate parameter variability) the interpolation method apparently performs poor because the grid is still not fine enough. Even for the finest grid, a further decrease of the time step size would not lead to any improvement, as the solution already converged to the best solution for this level of refinement. Due to memory limits a further refinement of the interpolation grid was not possible in this demanding three-dimensional scenario. For the reflection barrier method there is no change with grid refinement and the convergence to the correct solution with time step reduction is much faster when a transformation of the dispersive displacements and a one-sided reflection scheme were used.

2.5.2 Efficiency considerations

When comparing the results from the improved and the original reflection barrier method, the higher efficiency of the improved scheme is apparent in the more accurate results for the same time step Δt (see Figures 2.4 to 2.9). As the computation costs for the reflection barrier method and the interpolation method differ, the time step Δt cannot be taken directly as an indicator for the computational efficiency. We therefore evaluated the numerical error as a function of CPU time. For scenarios S2-1 and S2-2 with the intermediate parameter field variance we calculated a relative error which characterizes each result, ϑ_i, with respect to the ‘true’, ϑ_t, and worst, ϑ_w, solution,

$$\text{relative error} = \frac{\vartheta_i - \vartheta_t}{\vartheta_t - \vartheta_w} \tag{2.35}$$

In S2-1, ϑ_t was the average of the obtained U and D_L values of the interpolation method ($\Delta t = 0.001$ and $k = 8$) and the reflection barrier method ($\Delta t = 0.001$ and $k = 1$). This is justified because both methods converged to the same solution. In S2-2 we used the calculated reference RMSE (see Appendix A) as true solution. Fig. 2.12 demonstrates that for each result (apparent average velocity U, apparent longitudinal macrodisperion D_L, RMSE with respect to homogeneous concentration) the improved reflection barrier method represents the method with the highest computational efficiency (best result for any given CPU time). The higher computational cost of the interpolation method is based on: (1) the expensive bilinear interpolation of $\mathbf{u}$ and θ in each time step for every particle and (2) the calculation of a refined velocity matrix when grid refinement is applied. In scenario S2-1 and S2-2, the latter step is performed only once as we assumed a steady-state velocity field. We stress that the steady-state scenario used here is advantageous for the interpolation method. In particular when dealing with the commonly highly transient flow in soils, in which the velocity field is frequently updated, the calculation of the refined velocity matrix can become a considerable time-consuming factor for the interpolation method. The

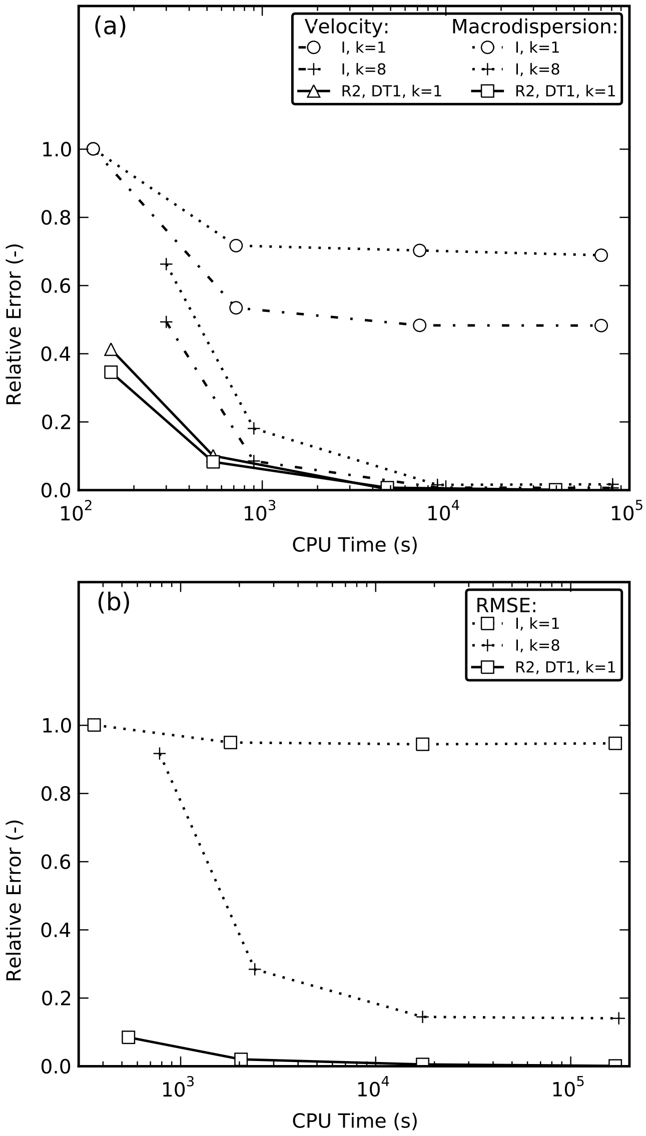

Figure 2.12: Relative error (Eq. 2.35) as a function of CPU time (s). (a) Scenario S2-1, relative error given for apparent average velocity U and apparent longitudinal macrodispersion D_L. (b) Scenario S2-2, relative error given with respect to best possible RMSE. k: Grid refinement factor, k is the number of subdivisions along each axis of the element of the coarsest grid: R2: one-sided reflection scheme, I: Interpolation method; DT1: Transformation of dispersive displacement applied.

improved reflection barrier method requires no grid refinement and its computational efficiency is therefore not affected by new velocity fields occurring under transient conditions.

The results of S2-1 and S2-2 (Fig. 2.7 and 2.9) indicate that a lower parameter variability, and thus a less demanding scenario, reduces the efficiency differences between the reflection barrier and interpolation method. In contrast, a higher variability does not influence the fast convergence of the improved reflection barrier method while the interpolation method has convergence problems even with the finest grid and smallest time step size. Based on these results, we conclude that the reflection barrier method is best suited for hydraulic parameter fields with high contrasts, while it has no disadvantages if the contrasts are lower.

2.5.3 Practical application aspects of the improved reflection barrier method

The proposed three algorithmic improvements to the reflection barrier method can easily be implemented in a standard RWPT code, as they only need small modifications of the core module responsible for the dispersive displacement of a particle.

The proposed RWPT algorithm is superior to other RWPT algorithms in situations where either the water content or the dispersion tensor are discontinuous. This can be the case when the flow velocity field is obtained from a discretization scheme where the water content is element-wise constant (like e. g. in cell-centered finite-volume schemes) resulting in abrupt changes of the dispersion tensor (as the pore water velocity is unsteady) and water content at element interfaces. However, even for finite-element solutions where the solution is much smoother, discontinuities can occur at material interfaces. The results showed that the efficiency gain of the reflection barrier method is increasing with the heterogeneity of the system, while the interpolation method gets severe problems to approach the true solution.

To obtain convergence with the reflection barrier method, in principle, reflecting barriers have to be applied at all element interfaces with a discontinuity of the dispersion tensor or water content. To reduce the computation time, it might be possible to define a threshold depending on the size of the jump indicating whether or not an interface should act as a reflection barrier. If a large part of the domain is characterized by negligible jumps between two adjacent elements, this could lead to a marked acceleration of the reflection barrier method. However, the error introduced by the thresholding has to be tested with a convergence analysis for the specific scenario.

2.6 Conclusions

We presented three improvements to the reflection barrier method used in RWPT algorithms. This method was originally developed to account for discontinuities of the dispersion tensor, but can also be used to account for abrupt changes in the water content and retardation factors as recently proposed by Lim (2006).

1. We showed that a linear time splitting for the dispersive displacement across an element interface with $\Delta t = \Delta t_1 + \Delta t_2$ proposed in the reflection schemes of Hoteit et al. (2002) and Lim (2006), and applied in subsequent studies (Salamon et al., 2006; Zhang et al., 2009) systematically overestimates the second dispersive displacement. The erroneous linear time splitting caused deviations of numerical results from analytical solutions observed in previous studies (Salamon et al., 2006). We derived a corrected time splitting with $\sqrt{\Delta t} = \sqrt{\Delta t_1} + \sqrt{\Delta t_2}$.

2. The results demonstrate that the two-sided reflection barrier method is only valid for $\Delta t \rightarrow 0$. Inaccuracies occur for a discrete time step size. To reduce this error, we derived a one-sided reflection scheme from the two-sided reflection coefficients of Lim (2006). The strength of the new approach is that monotonicity is preserved while the portion of reflected particles is systematically reduced at all element interfaces. Therefore, the error introduced by the reflection barrier method in a discrete time step size Δt is reduced.

3. In complex multidimensional transport problems with spatially abruptly varying anisotropic dispersion tensors, the reflection barrier method can be improved by a transformation of the dispersive displacement before performing the second dispersive displacement starting from an interface within one time step Δt. We proposed a transformation of the dispersive displacement that is consistent with the definition of the reflection coefficient and assures a proper convergence of the reflection barrier method to the true solution in complex multidimensional transport problems.

The comparison of RWPT simulations in two- and three-dimensional space applying different reflection barrier schemes demonstrated that only the improved reflection barrier method was able to converge to the true solution of the ADE for all scenarios. The improved reflection barrier method also provided more accurate results for a much larger time step size compared to the original reflection barrier schemes. In two- or three-dimensional simulations, where we usually deal with many element interfaces and complex flow and transport problems, significant jumps in the dispersion tensor or water content normally occur only at a small portion of the total number of element interfaces. For these cases, especially the proposed one-sided reflection scheme is very beneficial as it reduces the number of necessary reflections tremendously. We stress that the algorithmic issues and improvements presented here with respect to the reflection barrier method do not apply to the GSDE method.

A comparison with the interpolation method demonstrated that the reflection barrier method in combination with the improvements can provide more efficiently accurate results of the complex three-dimensional transport problems presented in this study. Especially for abrupt changes of the dispersion tensor and unsaturated conditions characterized by highly heterogeneous water contents, the improved reflection barrier method has important advantages since, unlike the interpolation method, it does not require grid refinements to represent discontinuities. In the interpolation method, results improve when refining the grid used for the bilinear interpolation of the variables governing the dispersive displacement. The results presented in this thesis demonstrate that the problems resulting from the application of the reflection barrier method to complex three-dimensional scenarios, which have been reported before (LaBolle et al., 1996; Salamon et al., 2006), can be alleviated effectively using the proper improvements or corrections.

The proposed RWPT algorithm may be very useful in parameter optimization and geostatistical inversion studies for groundwater or vadose zone applications, in which numerous forward model runs need to be performed with acceptable accuracy in short times. We stress that the algorithm combines the good performance of RWPT under advection-dominated transport conditions with an improved treatment of the dispersive transport. Especially for simulations in the vadose zone, where advection- and dispersion-dominated transport conditions alternate, it is important that numerical codes work efficiently under both conditions. However, the new algorithm also enhances the applicability of RWPT to groundwater studies, in which dispersion from or into low velocity zones must be simulated accurately.

Chapter 3

Near-surface solute redistribution during evaporation[*]

Abstract

We present results from solute transport experiments in an evaporating composite porous medium consisting of a cylindrical inner core with coarse sand that was surrounded by a mantle with fine sand. Small volumes of dye and salt tracer were applied at the surface of the fine material of the evaporating column. The pressure head at the bottom boundary was kept constant using a hanging water table ensuring liquid phase continuity to top surface in both fine and coarse material, whereby the latter was hydraulically less conductive at these pressure conditions. Contrary to the expectation that solute accumulation at an evaporating surface is proportional to local cumulative evaporation, high concentration spots developed at the surface of the coarse material, for which IR surface temperature measurements did not indicate higher evaporation fluxes. Three-dimensional unsaturated flow and transport simulations and a second tracer experiment monitored with magnetic resonance imaging (MRI) demonstrated that preferential upward water flux in the fine sand deeper in the column and near-surface lateral water flow from the fine into the coarse sand in combination with a downward diffusive flux are responsible for the local solute accumulation. We propose that at the wet regions of a soil surface, solute accumulation is largely decoupled from local evaporation fluxes and strongly governed by relative differences of the hydraulic conductivities. The possible formation of high solute concentration spots at the surface of coarser regions usually representing preferential flow pathways during strong precipitation may have an accelerating effect on the leaching of solutes.

---

[*] adapted from: Bechtold, M., S. Haber-Pohlmeier, J. Vanderborght, A. Pohlmeier, T.P.A. Ferré, and H. Vereecken. 2011a. Near-surface solute redistribution during evaporation. Geophys. Res. Lett., 38, L17404.

3.1 Introduction

Quantifying solute migration through soil is critical for understanding nutrient cycling and soil/atmosphere mass flux and for managing soil and groundwater quality. Solute transport in the vadose zone is a complex problem because of the combined effects of soil heterogeneity and the nonlinearity of unsaturated water flow. In the shallow subsurface, the problem is further complicated by the spatial and temporal variability of precipitation and evapotranspiration. Numerical studies in multi-dimensional Gaussian-type heterogeneous soils have shown that solute leaching rates under realistic weather conditions are reduced compared to steady-state conditions, while vertical spreading may either decrease or increase depending on the structure of soil heterogeneity (Russo et al., 1998; Vanderborght et al., 2006). These phenomena were explained by two underlying processes: (1) lateral transport of solute mass into the finer soil matrix during redistribution and upward flow intervals; and (2) a higher downward flow rate during short precipitation events which can either decrease or increase spatial flow variability.

Comparisons between numerical simulations and experimental observations of solute transport in unsaturated heterogeneous porous media with known heterogeneity are essential for supporting numerical studies but are only available for steady-state infiltration conditions (Wildenschild, 1999a; Rossi et al., 2008) and they are missing for non-monotonic transient flow conditions. Recent experiments have confirmed lateral water redistribution within composite porous media from coarse- to fine-grained zones during drying, which may occur over large distances and significantly enhance evaporative losses from heterogeneous porous media compared to homogeneous equivalents (Lehmann and Or, 2009). The simulation of this lateral redistribution and its effect on solute transport is directly linked to the imposed boundary conditions at the heterogeneous soil surface. Unlike for infiltration events, the definition of boundary conditions for evaporation from heterogeneous soil surfaces is debated (Shokri et al., 2008b).

In this study, we present results of two experimental setups. First, salt and dye tracer experiments are used to provide experimental evidence of solute redistribution at the evaporation surface of a composite porous medium. Second, solute redistribution during a full cycle of infiltration and evaporation within and at the evaporation surface of a heterogeneous medium was observed using magnetic resonance imaging (MRI). In contrast to recent evaporation experiments in composite porous media (Lehmann and Or, 2009; Shahraeeni and Or, 2010; Nachshon et al., 2011), we conducted experiments under which the fine and coarse material remained permanently under ‘stage-1’ (liquid flow-dominated) evaporation conditions. Therefore, this study provides indications of solute accumulation in regions at the soil surface that are connected by liquid flow to the deeper soil. Observations were compared with numerical simulations based on common continuum-scale theory for liquid flow and solute transport.

3.2 Material and methods

3.2.1 Laboratory experiments

Laboratory experiments were carried out in coaxial cylindrical quartz sand columns (height: 12.5 cm, diameter d = 8 cm), consisting of a core (d = 2.9 cm) of coarse sand (FH31) surrounded by fine sand (F36) with mean grain sizes of 0.35 and 0.165 mm, respectively (manufacturer: Quarzwerke Frechen GmbH, Germany). The columns were closed at the bottom by a porous glass filter plate, which remained saturated (saturated hydraulic conductivity Ks = 655 cm d^{-1}) and hydraulically coupled to a reservoir of deionized water. Prior to the experiment, the samples were flushed with deionized water and hydrostatic equilibrium was established with a water table located 19.5 cm below the bottom boundary. We applied 9 ml tracer solution ($\sim$ 2 mm water column) manually with a syringe to the surface of the fine sand in four columns. Brilliant Blue (BB) (0.38 wt. %) and KCl (0.6 wt. %) were each used separately as tracers in two of the columns. After tracer application, one column of each pair was covered by a plate to eliminate evaporation, while the others were placed under a fan to create a steady evaporation rate.

The evaporation rate was measured continuously by weighing the water reservoirs over a period of 10 days and ranged between 0.7 and 1.0 cm d^{-1}. Evaporation rates varied between the columns due to their different position to the fan and varied over time due to air temperature and humidity variations in the lab. No systematic decline in evaporation rate over time was observed so that a nearly steady-state evaporation rate could be assumed. The spatial distribution of the evaporation rate from the heterogeneous soil surface was inferred from surface temperature images obtained with an IR camera (A320, FLIR System). Evaporative cooling resulted in a nearly constant and uniform temperature difference of 3 K between evaporating and non-evaporating columns indicating a uniform evaporation flux from the coarse and fine material. Only the last IR measurement of the evaporating KCl column at day 9 indicated an increase of temperature by 0.5 K in the coarse compared to the fine material. After 10 days, the complete volumes of fine and coarse material were sampled separately and the mass of BB and KCl in each material was determined by leaching the materials with deionized water.

In a second experiment, transport of an MRI contrast agent Gd-DTPA^{2-} (Haber-Pohlmeier et al., 2010) was monitored during an infiltration followed by an evaporation phase in an identically prepared sand column. During infiltration, single drip irrigation was applied with a rate of 3 cm^3 min^{-1} at the center of a porous plate (d = 5 cm) placed on the sample surface and a water table at 1.5 cm below the bottom plate of the column. The hydraulic conductivities of the two materials for this shallow water table were much higher than the infiltration rate, so that the pressure conditions deviated only weakly from hydrostatic equilibrium. When steady flow conditions were reached, 8 cm^3 of a 5 mmol l^{-1} (0.28 wt. %) Gd-DTPA^{2-} solution were applied and flushed with 62 cm^3 of tracer free solution at the same infiltration rate. After irrigation, i. e. 23 minutes after the start of the tracer application, the water table was lowered and maintained as in the first experiment at 19.5 cm below the bottom boundary. The porous plate was removed from the surface and a fan was operated for 10 days. The evaporation rate, which was measured continuously, ranged between 0.31 and 0.51 cm d^{-1} and showed no systematic decline.

Tracer distribution was visualized by collecting high resolution MRI scans using a 4.7 T (200 MHz for ^{1}H) vertical ultra wide bore magnet (Magnex Scientific, UK), equipped with a Varian gradient system of maximum 300 mT/m and a 170-mm birdcage rf coil. The system was operated by VNMRJ software (Varian, UK). The measurements were performed using a single-echo-multi-slice imaging pulse sequence with strong T_1 weighting ($t_R = 0.25$ s, $t_E = 4.1$ ms, 4 vertical slices of 2 mm thickness, FOV: 140 x 140 mm, matrix size 128 x 128) leading to a nearly linear relation between MRI signal intensity, S/S_0, and the logarithm of the Gd-DTPA^{2-} concentration in the range of 0.1-5 mmol l^{-1} (Haber-Pohlmeier et al., 2010). Above 5 mmol l^{-1}, S/S_0 decreases with increasing Gd-DTPA^{2-} concentration. Water distribution was determined by the same sequence, but without T_1 weighting and setting $t_R = 4$ s. The water content θ (m^3 m^{-3}) maps were calculated from the spatially resolved signal amplitudes. The relative error is about 10 % per voxel (e. g. $\theta = 0.2 \pm 0.02$).

3.2.2 Flow and transport modeling

Water flow was described locally by Richards' equation (Richards, 1931),

$$\frac{\partial \theta\,(h)}{\partial t} = -\nabla\cdot\, \theta \mathbf{u} = \nabla\cdot\, [K\,(\theta)\,\nabla h] + \frac{\partial K\,(\theta)}{\partial z} \tag{3.1}$$

where t is time (d), h is pressure head (cm), θ is volumetric water content (m^3 m^{-3}), $\mathbf{u}$ is the pore water velocity vector (cm d^{-1}), K is hydraulic conductivity (cm d^{-1}) and z is the vertical coordinate directed upwards (cm). $\theta(h)$ and $K(\theta)$ were described by the van Genuchten-Mualem (vGM) parametric expressions (van Genuchten, 1980). Eq. 3.1 was numerically solved with a cell-centered finite-volume code (e. g., Ippisch et al., 2006). Solute transport was assumed to be governed by the advection-dispersion equation,

$$\theta \frac{\partial C}{\partial t} = -\theta \mathbf{u}\cdot\, \nabla C + \nabla\cdot\, (\theta \mathbf{D}\cdot\, \nabla C) \tag{3.2}$$

where C is solute concentration in pore water (mmol l^{-1}), $\mathbf{D}$ (cm^2 d^{-1}) is the local-scale dispersion tensor of an isotropic porous medium, with $\mathbf{D} = (\alpha_T \|\mathbf{u}\| + D_m)\,\mathbf{I} + (\alpha_L - \alpha_T)\,\mathbf{u}\mathbf{u}^T \|\mathbf{u}\|^{-1}$, where α_T and α_L are the transversal and longitudinal dispersivities (cm), D_m is the effective molecular diffusion coefficient (cm^2 d^{-1}), and $\mathbf{I}$ is the identity matrix. Solute transport was modeled using the random walk particle tracking code PARTRACE (Bechtold et al., 2011b).

The lower boundary of the experiments was described by a prescribed pressure head depending on the imposed water table level. Drip irrigation was modeled as a constant flux by applying the irrigation flow rate uniformly to a circular area surface of 2 cm diameter based on experimental observation (wetted part of the porous plate). Evaporation from the heterogeneous surface was modeled as a uniform flux boundary condition (0.78 cm d^{-1} for the BB and KCl experiments and 0.42 cm d^{-1} for the Gd-DTPA^{2-} experiment), which is supported by IR-derived surface temperature. Simulations were also carried out with lower evaporation rate in the coarse than in the fine material.

Water flow and solute transport were simulated in three dimensions with a regular grid spacing of 0.1 cm. The hydraulic parameters of the two materials were determined using pressure cells and multi-step outflow experiments (vGM coarse sand: $\theta_s = 0.4$, $\theta_r = 0.05$, $K_s = 3888$ cm d^{-1}, $\alpha = 0.035$ cm^{-1}, $n = 8.0$; fine sand: $\theta_s = 0.41$, $\theta_r = 0.05$, $K_s = 2496$ cm d^{-1}, $\alpha = 0.0177$ cm^{-1}, $n = 10.8$). We set the longitudinal dispersivity α_L to the mean grain size and the transverse dispersivity $\alpha_T = 0.1\alpha_L$, which are typical values reported for saturated unconsolidated homogenous porous media (Yoon et al., 2008). The diffusion coefficients $D_{m,w}$ of KCl, BB and Gd-DTPA^{2-} in water were assumed to be 1.77, 0.086, and 0.35 cm^2 d^{-1} (Kasteel et al., 2002; Osuga and Han, 2004), respectively, and were evaluated as a function of water content to obtain D_m, $D_m = \theta^{(7/3)}/\theta_s^2\ D_{m,w}$ (Millington and Quirk, 1961). The three-dimensional model was used to predict the solute concentrations in space and time, which were compared to the MRI results and to the KCl and BB masses that accumulated in the coarse material.

3.3 Results and discussion

3.3.1 Near-surface redistribution of tracers

The redistribution of BB that was applied at the surface of the fine sand of an evaporating and non-evaporating column is shown in Fig. 3.1. In the column without evaporation, diffusion homogenizes the solute concentration at the soil surface. Diffusion also reduces the concentration at the soil surface due to vertical diffusive mass transport into the soil column as can be derived from decrease of the blue color saturation. In the evaporating column, the dye tracer accumulated during the experiment in the coarse sand whereas the concentration at the surface of the fine sand decreased over time. The decrease in concentration at the surface of the fine sand in the evaporating soil column was not accompanied by a vertical diffusion front that moved downward as in the non-evaporating soil column. The appearance of a thin salt crust in the coarse sand at the end of the experiment of the column to which KCl was applied corroborates the observations of the BB accumulation in the coarse sand.

The mass that accumulated in the coarse sand, which makes up 14 % of the

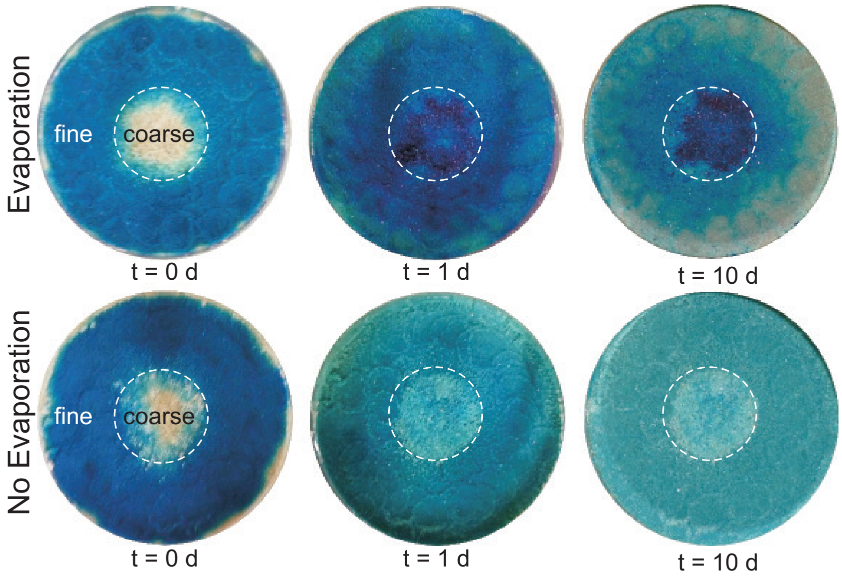

Figure 3.1: Brilliant Blue (BB) experiment. Upper row: column exposed to evaporation. Lower row: covered column, no evaporation.

evaporating surface, was 80 % and 36 % of the applied BB and KCl tracer mass, respectively, in the evaporating columns and 10 % and 8 % of the applied BB and KCl tracer mass, respectively, in the non-evaporating columns. The larger mass fraction of tracer in the coarse material than the evaporating surface fraction of the coarse material implies that mass was transferred by lateral advection fluxes against a concentration gradient from the fine into the coarse sand.

Fig. 3.2 shows the simulated mass accumulation in the coarse sand over time and the observed accumulation after 10 d. The simulated mass accumulation in the coarse sand of the evaporating columns is also larger than the evaporating surface fraction of the coarse sand. This implies that the observed tracer mass transfer from the surface of the fine sand and accumulation at the surface of the coarse sand is in line with classical theory of water flow and solute transport in unsaturated media. However, while the accumulation of BB in the coarse sand of the evaporating column was explained very well by the simulation that assumes uniform evaporation, the accumulation of KCl in the evaporating column was strongly overestimated.

It must be noted that the evaporation fluxes in the coarse and fine material are not predicted by the unsaturated flow equation but are imposed boundary conditions. Based on the uniform surface cooling indicated by IR images, we assumed a uniform evaporation flux. However, due to the relatively small difference in surface temperature between the evaporating and non-evaporating surfaces (3 K), some difference in evaporation rate from the coarse and fine material could have been undetected in the IR surface temperature measurements. Two causes for a lower evaporation rate from the coarse material could be brought forward. First, the rate at which water is removed from the soil surface depends on the vapor pressure at the

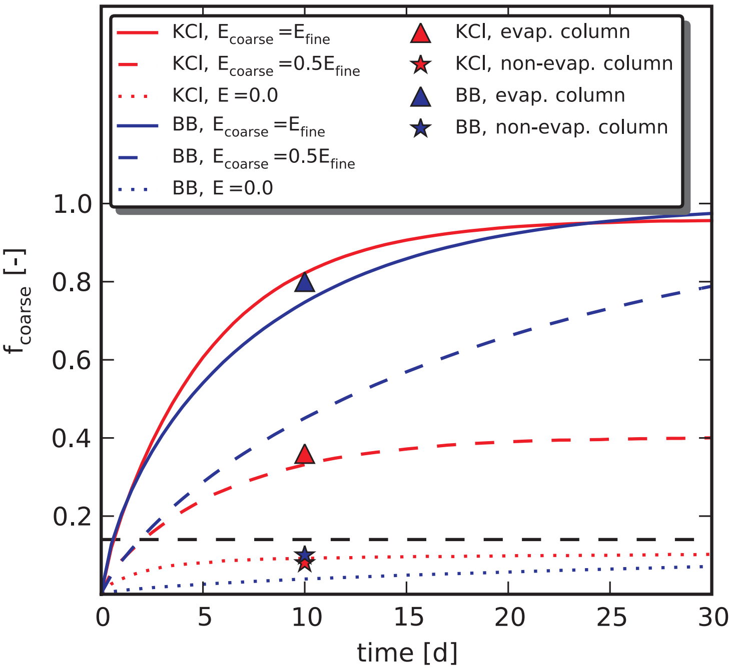

Figure 3.2: Modeled and measured solute mass fraction in coarse sand f_{coarse} vs. time after solute application. Black dashed line indicates the evaporating surface fraction of coarse sand. Single data points indicate solute mass fractions determined at the end of the experiment (t = 10 d).

soil surface, which is close the saturated vapor pressure, and to the resistance to vapor transfer in the air above the soil layer. Recent work of Lehmann and Or that builds on earlier work of Suzuki and Maeda (1968), shows that above drier surfaces of coarse grained materials the resistance to vapor transfer is larger and the evaporation rate smaller than above wetter surfaces of fine grained materials due to larger distances between evaporating micro scale patches. Second, the increasing osmotic potential of the pore water and the thin salt crust observed at the evaporation surface of the evaporating KCl column may be another reason for a decline in evaporation rate towards the end of the experiment. Therefore, simulations were carried out also for a lower evaporation rate in the coarse sand (0.5 of the evaporation rate from the fine sand). Also for this case, tracer mass accumulation in the coarse sand was simulated (Fig. 3.2) so that the occurrence of near-surface lateral advective mass transfer and solute accumulation in the coarse sand are not critically dependent on a uniform evaporation rate boundary in the different materials.

Despite the fact that tracer accumulation in the coarse sand must be attributed to a lateral advective flux, also diffusive fluxes play a role in the lateral redistribution process. The smaller molecular diffusion constant of BB compared to KCl leads to larger accumulation of BB at later times, because the simulated back diffusive flux from the coarse material is smaller when the molecular diffusion constant is smaller. The effect of back diffusion is enhanced when the lateral advective fluxes into the coarse material are decreased due to a lower evaporation rate from the coarse material. A lower evaporation rate from the coarse material in the evaporating KCl column towards the end of the experiment together with back diffusion could explain the lower experimental accumulation of KCl compared to BB.

To obtain better insight in the processes leading to near surface lateral redistribution, the hydraulic conductivities of the two materials at the different heights, simulated water contents, and water flux vectors during the steady-state evaporation are shown in Fig. 3.3a and 3.3b. Above -11 cm height in the soil column, the fine sand is more conductive than the coarse sand. This leads to a lateral redistribution of water from the coarse into the fine sand between -11 cm and -2 cm height and to a lower upward flux in the coarse sand than in the fine sand. Imposing a uniform evaporative demand, lateral flow back from the fine into the coarse sand close to the sample surface between -2 and 0 cm height must compensate for the lower upward flux in the coarse sand deeper in the sample. The simulated surface water content in the coarse sand of $\theta = 0.17$ and its near-surface unsaturated hydraulic conductivity of 110 cm d^{-1} were still high enough to ensure liquid phase continuity and the lateral fluxes that sustain the evaporative demand from the coarse sand with relatively low hydraulic gradients. In addition to the uniform IR surface temperatures and uniform evaporative cooling, the fact that the coarse sand surface did not consist of loose sand particles is an additional indication that also in the experiment liquid films and water menisci that keep particles together and ensure liquid phase continuity were present.

Representing solute diffusion by random particle displacements can be used to illustrate the accumulation of solutes in the coarse material (Fig. 3.3c). When solutes at the evaporating surface of the fine sand are moved downwards by diffusion against the upward evaporative flux, the lateral component of the advective flux will result in a net lateral solute flux from the fine towards the coarse material.

3.3.2 Redistribution of tracers deeper in the sample

Fig. 3.4 shows MRI observed and simulated water content and MRI signal intensities S/S_0, which are between 0.3 and 0.8 proportional to the logarithm of Gd-DTPA^{2-} concentration, during an infiltration-evaporation cycle in the composite medium. During the infiltration phase, high pressure heads caused a nearly uniform water content distribution in the sample with small variability being related to packing inhomogeneities and lower MRI sensitivity at the top and bottom of the sample (Fig. 3.4a). Under these conditions, hydraulic conductivity was highest in the inner core filled with coarse sand.

The infiltration phase was characterized by fast transport in the coarse sand, while lateral flow away from the drip source and dispersive spreading moved part of the tracer plume into the fine sand (Fig. 3.4b, $t = 2$ min). The lowering of the water table

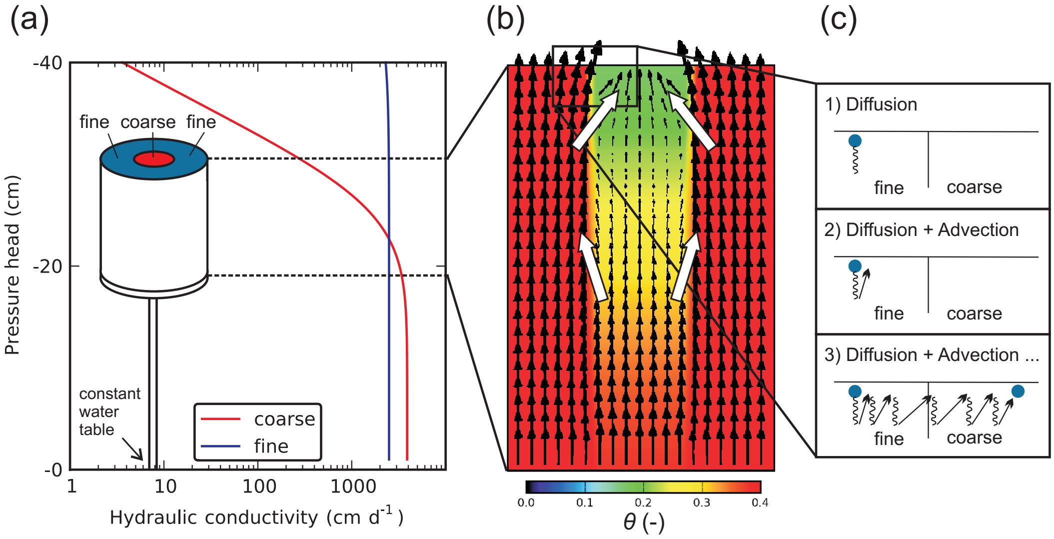

Figure 3.3: (a) Hydraulic conductivity vs. pressure head of the coarse (red) and fine sand (blue). Illustration of the column: Due to the high hydraulic conductivity, pressure head varies almost linearly with depth and deviates little from the hydrostatic equilibrium. (b) Simulated water contents and water flux vectors scaled by magnitude during steady-state evaporation. White vectors indicate principal flow direction (c) Concept of back diffusion and lateral water flow leading to near-surface lateral redistribution and solute mass accumulation.

between infiltration and evaporation phase caused drainage mainly from the coarse sand which moved the tracer plume down in the coarse sand (Fig. 3.4b, $t = 2$ h). The lowering of the water table and the change of the flow direction provoked a change of the flow pattern. Both experiment and simulation show that mass accumulated more rapidly at the soil surface in both the fine and coarse material than that the plume in the coarse material moved upward so that the zone between the tracer plume in the coarse material and the soil surface seems to be bypassed by the tracer (Fig. 3.4b, day 1 to 5). This suggests that deeper in the soil profile, tracer was transported from the coarse to the fine material, in which the upward flux was higher.

The simulations indicate that lateral redistribution continues when most of the tracer mass is at the soil surface and leads to a depletion of tracer in the fine sand and an accumulation in the coarse sand (Fig. 3.4b, day 8 to 10). The simulations also indicate that the accumulation leads to a zone of high tracer concentrations in a shallow layer below the soil surface that exceeds the concentration range with a positive correlation between tracer concentration and S/S_0. However, the increase in S/S_0 deeper below the surface in the coarse sand combined with a decrease in the fine zone between day 8 and 10 indicates a near surface lateral redistribution of the tracer mass in the experiment. This increase at a greater depth could have been caused by density-driven downward transport, which is ignored in the model. The removal of the infiltration disk and the sand that stack to it disturbed the coarse sand surface, caused a lower packing density, lower water contents close to the soil surface

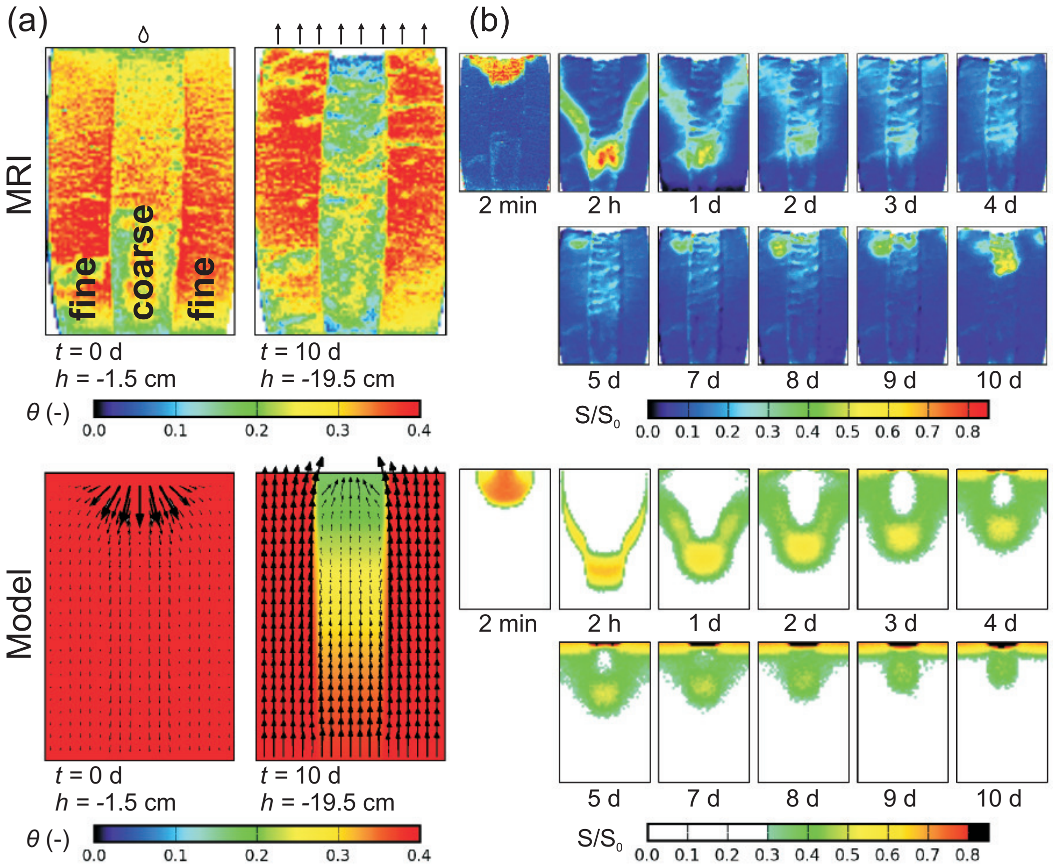

Figure 3.4: Gd-DTPA^{2-} tracer experiment. Shown is a vertical slice through the center of the column. (a) Top: Water content derived from MRI during infiltration and evaporation phase; Bottom: Modeled water content and flow vectors scaled by magnitude. (b) MRI Signal intensity S/S_0 that is proportional to logarithm of the Gd-DTPA^{2-} concentration; top: derived from MRI, bottom: derived from simulated Gd-DTPA^{2-} concentration.

and a local depression of the evaporating surface in the coarse sand which was a few mm lower than the evaporating surface of the fine sand. This depression may have caused a lower evaporation rate from the coarse sand and less lateral redistribution of tracer mass close to the surface.

3.4 Conclusions

We presented experimental evidence of solute redistribution at the wet surface of a composite porous medium during evaporation. The observations were well reproduced by numerical simulations based on Richards' equation and advection-dispersion equation. One key result of the redistribution process was the accumulation of solutes in coarse-grained zones near the sample surface. For evaporating wet surfaces that are connected by liquid films to the deeper soil, the results of this study indicate that solute accumulation may be largely decoupled from the local evaporation fluxes and rather be governed by the relative differences of the hydraulic conductivities, the scale of the heterogeneity, and the diffusion coefficient and solubility of the dissolved substance. Molecular diffusion that moves solutes away form the evaporating surface back into the porous medium in combination with lateral water flow will redistribute and accumulate solutes towards locations with the lowest hydraulic head, i. e. the lowest sum of pressure and gravitational head. These locations correspond to regions with low hydraulic conductivity, which can be either fine- or, like in our experiments, coarse-grained regions, depending on the capillary pressure conditions. Using simulations, we showed that locations where solutes accumulate need not be locations with the highest local evaporation.

The results obtained in this study are different from salt accumulation that was observed in evaporation experiments of successively drying composite porous media (Lehmann and Or, 2009; Shahraeeni and Or, 2010; Nachshon et al., 2011). In these experiments part of the evaporating soil surface dried out and was not connected by liquid flow to the deeper soil. Evaporation from the dried out part of the surface was dominated by vapor flow in the porous medium. When a soil surface consists of dry regions dominated by vapor-flow and wet regions dominated by liquid-flow to the soil surface, solute accumulation takes place at the surface of the liquid-flow dominated region, i. e. the fine region, where the evaporation rate is higher. The comparison of our results with the previous experiments indicates that solute redistribution and locations of solute accumulation on a heterogeneous surface depends on the state of the surface. Since the soil surface state changes dynamically, it is therefore not possible to make generally valid statements about salt accumulation on heterogeneous soil surfaces.

The accumulation of solutes at the surface of coarser regions that are usually preferential flow pathways during strong precipitation may have an accelerating effect on the leaching of solutes. Where and whether redistribution occurs depends on the timing and duration of leaching and evaporation periods after solute application. This lends further importance to understanding the dynamics of boundary conditions, complementing effects such as macropore flow activation during infiltration. Future research should investigate the impacts of heterogeneity during infiltration and evaporation across a range of soil structures and boundary conditions, perhaps leading to an effective parameter model that can account for the small-scale redistribution processes at larger scales.

Chapter 4

Upward transport in a 3-D heterogeneous laboratory soil under evaporation conditions[*]

Abstract

Upward water flow induced by evaporation can cause soil salinization, transport of contaminants to the soil surface, and influences the migration of solutes to the groundwater. In this study, we used electrical resistivity tomography (ERT) to obtain time-lapse images of an upward flow tracer experiment under evaporation conditions in a three-dimensional (3-D) spatially correlated heterogeneous laboratory soil composed of three different materials (coarse, medium and fine-grained sand). The tracer experiment was performed during 40 days of quasi-steady-state upward flow conditions. Observed transport was compared with 3-D numerical simulation based on Richards' and advection-dispersion equation. ERT-derived and modeled solute transport correlated well in the lower part of the laboratory soil while deviations increased towards the surface. Inversion of synthetic ERT data indicated that the deviations cannot be explained by ERT errors only, but also that errors of the flow and transport model must be invoked. In the experiment, the actual evaporation locally exceeded the potential evaporation rate determined as maximum evaporation from open water. This was not reproduced by the classical potential/actual evaporation concept. Introducing the partial compensation of low evaporation zones by increasing the potential evaporation rate uniformly led to a better correlation between monitored and modeled transport. Despite the remaining deviations, experiment and model showed a consistent and systematic pattern of preferential pathways. Close above the water table most of transport occurred in the coarse material, while with increasing height transport was dominated by finer materials. For the first time, such a transition of preferential pathways of upward transport was demonstrated experimentally.

---

[*] adapted from: Bechtold, M., J. Vanderborght, L. Weihermüller, M. Herbst, T. Günther, O. Ippisch, R. Kasteel and H. Vereecken. 2011c. Upward transport in a 3-D heterogeneous laboratory soil under evaporation conditions. Submitted to Vadose Zone J, V11-0066.

4.1 Introduction

Evaporation causes local upward water flow in the vadose zone. This upward water flow carries solutes towards the soil surface and is therefore a key process in soil salinization and the transport of contaminants to the soil surface (Jury et al., 1990; Nassar and Horton, 1999; Ozturk and Ozkan, 2004). Although net water and solute flux is mainly downwards in most non-arid climates, upward flow periods are also observable in dry periods. Therefore, upward flow and transport are relevant for solute migration even under such climatic conditions (Russo et al., 1998; Vanderborght et al., 2006; Bechtold et al., 2011a).

The complexity of solute migration is strongly coupled to the highly-nonlinear soil water flow problem that arises from the superposition of the non-linear soil hydraulic functions, the spatially and temporally variable boundary conditions, and the spatial heterogeneity of soil hydraulic properties. Soil heterogeneity is known to occur at different spatial scales (Vogel and Roth, 2003) and can be described by Gaussian scaling approaches (Russo and Bouton, 1992) and non-Gaussian components such as connected paths and abrupt changes (Coquet et al., 2005; Neuweiler and Vogel, 2007). The location of preferential water flow and solute transport in heterogeneous soils depends on the spatial distribution of the actual hydraulic conductivity. In an unsaturated soil and for temporally varying boundary conditions this spatial distribution may change over time (e. g., Roth, 1995; Mohammadi and Vanclooster, 2011). Numerical studies in multi-dimensional Gaussian-type heterogeneous soils demonstrated that under natural weather conditions with upward flow periods solute leaching rate is reduced compared to steady-state infiltration conditions while the vertical spreading may either decrease or increase depending on the underlying statistics of soil heterogeneity (Russo et al., 1998; Vanderborght et al., 2006). Mainly two processes have been identified to generate these effects: (1) lateral redistribution of solute mass into the finer soil matrix during upward flow intervals and (2) a higher flow rate during infiltration which can either decrease or increase spatial flow variability.

As in these studies, a basic understanding of unsaturated flow and transport processes is often gained from numerical simulations that are based on Richards' equation (RE) and advection-dispersion equation (ADE) (Herbst et al., 2005). When fully-distributed two- or three-dimensional models are used to reproduce observed transport in field soils or columns of undisturbed soil, results are often not satisfying and deviations between modeled and observed data occur (e. g., Kasteel et al., 2000; Coquet et al., 2005; Javaux et al., 2006; Vogel et al., 2006). Researchers have recognized that unresolved horizontal and vertical soil heterogeneity causes large parts of these deviations. In general, the uncertainty in the heterogeneity of natural soils is often so dominant that it is difficult to detect further issues of the model.

Therefore, experimental studies in unsaturated heterogeneous porous media with known heterogeneity, hereforth called ‘laboratory soils’, are highly valuable to evaluate the accuracy of numerical simulations based on RE and ADE. During the last decades, researchers constructed laboratory soils with increasing complexity. The first approaches are reported for the investigation of solute migration in laboratory aquifers (Silliman et al., 1998, and references therein). Unfortunately, similar studies focusing on unsaturated flow and transport are less frequent. Amongst the first, Wildenschild et al. (1999b; 1999a) analyzed the flow-rate dependency of preferential infiltration and transport in a two-dimensional laboratory soil composed of five different sands. They evaluated the applicability of effective parameters to describe transient flow and transport events. Based on these ideas, Ursino et al. (2001) constructed a two-dimensional laboratory soil with an anisotropic structure and oblique bedding. Their infiltration experiments showed that the flow-rate controlled a saturation-dependent macroscopic anisotropy which in a feedback governed the preferential flow and transport pattern. The detailed comparison with numerical flow and transport simulations in subsequent studies (Ursino, 2004; Rossi et al., 2008) demonstrated that numerical simulations based on RE and ADE were able to describe the main features of the observed transport process.

Despite the significance of upward transport for groundwater quality management and sustainable agricultural practice, little effort was made to experimentally measure upward transport at given boundary conditions and to test existing numerical models on laboratory soil setups with high complexity. For a homogeneous laboratory soil, Mohamed et al. (2000) performed an upward flow tracer experiment during evaporation from a shallow water table. Using numerical simulations they proved the validity of RE and ADE under the given experimental conditions. On the other hand, recent experiments in composite porous media of two materials have confirmed lateral water redistribution within composite porous media from coarse to fine grained zones during evaporation, which may occur over large distances and significantly enhance evaporative losses from heterogeneous porous media compared to homogeneous equivalents (Lehmann and Or, 2009). These experiments were not compared with numerical simulations. By the combination of tracer experiments and numerical simulations, Bechtold et al. (2011a) introduced a second redistribution process under evaporation conditions that occurs close to the soil surface. They demonstrated that as long as liquid water flow to the soil surface is sustained to coarse- and fine-grained zones, lateral flow in combination with a downward diffusive flux will redistribute and accumulate solutes towards locations with the lowest hydraulic head at the evaporation surface.

During the last two decades, non-invasive geophysical measurement techniques have been increasingly developed and evaluated in a hydrological context (Binley et al., 2010). The spatially and temporally highly resolved data obtained from these techniques allow the detailed analysis of the effect of heterogeneity on flow and transport at different spatial scales. Electrical resistivity tomography (ERT) became the most popular technique for monitoring saline tracer movements in soils and aquifers because of its direct sensitivity to water electrical conductivity changes. ERT can be applied at both the laboratory scale (Binley et al., 1996; Slater et al., 2002; Koestel et al., 2008; Garré et al., 2010) and the field scale (Kemna et al., 2002; Singha and Gorelick, 2005; Looms et al., 2008; Monego et al., 2010; Oberdörster et al., 2010).

Referring to the lack of knowledge of upward flow and transport in heterogeneous soils, we present the results of a tracer experiment that was performed in a complex heterogeneous laboratory soil under upward flow conditions, which was monitored with ERT. To our knowledge this is the first attempt to experimentally analyze upward flow in such complex soil. The first objective of this study is the detailed comparison between observed and modeled solute transport and to attribute resulting deviations to ERT and flow and transport modeling errors. The well-controlled experimental setup is used to evaluate the potential of ERT to non-invasively image and characterize upward transport in heterogeneous soils. Thereby, ERT errors are investigated by additional synthetic ERT experiments. On the other hand, flow and transport modeling errors are evaluated by two different approaches for modeling the evaporation pattern at the soil surface. The second objective of this study is to analyze the effect of soil heterogeneity on upward transport. We find that a three-dimensional solute transport analysis identifies locations of preferential flow and transport under upward flow conditions.

4.2 Material and methods

4.2.1 Sandbox and boundary conditions

The experiment was performed on a sandbox of size $87.5 \times 87.5 \times 83.2$ cm^3 (length × width × height) with side walls of Plexiglas and a bottom composed of nine square nylon porous suction plates (ecoTech Umweltsysteme, bubble point 1000 hPa). The sandbox was settled on a precision balance with a resolution of 100 g m^{-2}. A schematic drawing of the setup is presented in Fig. 4.1a and a photographic documentation in Appendix B. The outlets of the suction plates were connected to a water reservoir, which was settled on a separate balance to measure the inflow rate. A Mariotte's bottle was used to maintain a constant head of -2.5 cm at the bottom of the porous medium throughout the experiment. The sandbox was insulated at the four side walls, while the bottom was exposed to laboratory temperature. The top was covered with an evaporation chamber with four inlets, one at each side wall, and a central outlet at the top. The evaporation chamber was entirely insulated from the laboratory.

Dry air with an absolute humidity of 0.8 g m^{-3} at 0.1 MPa was heated by an air heater prior to entering the evaporation chamber through the inlets at a flow rate of

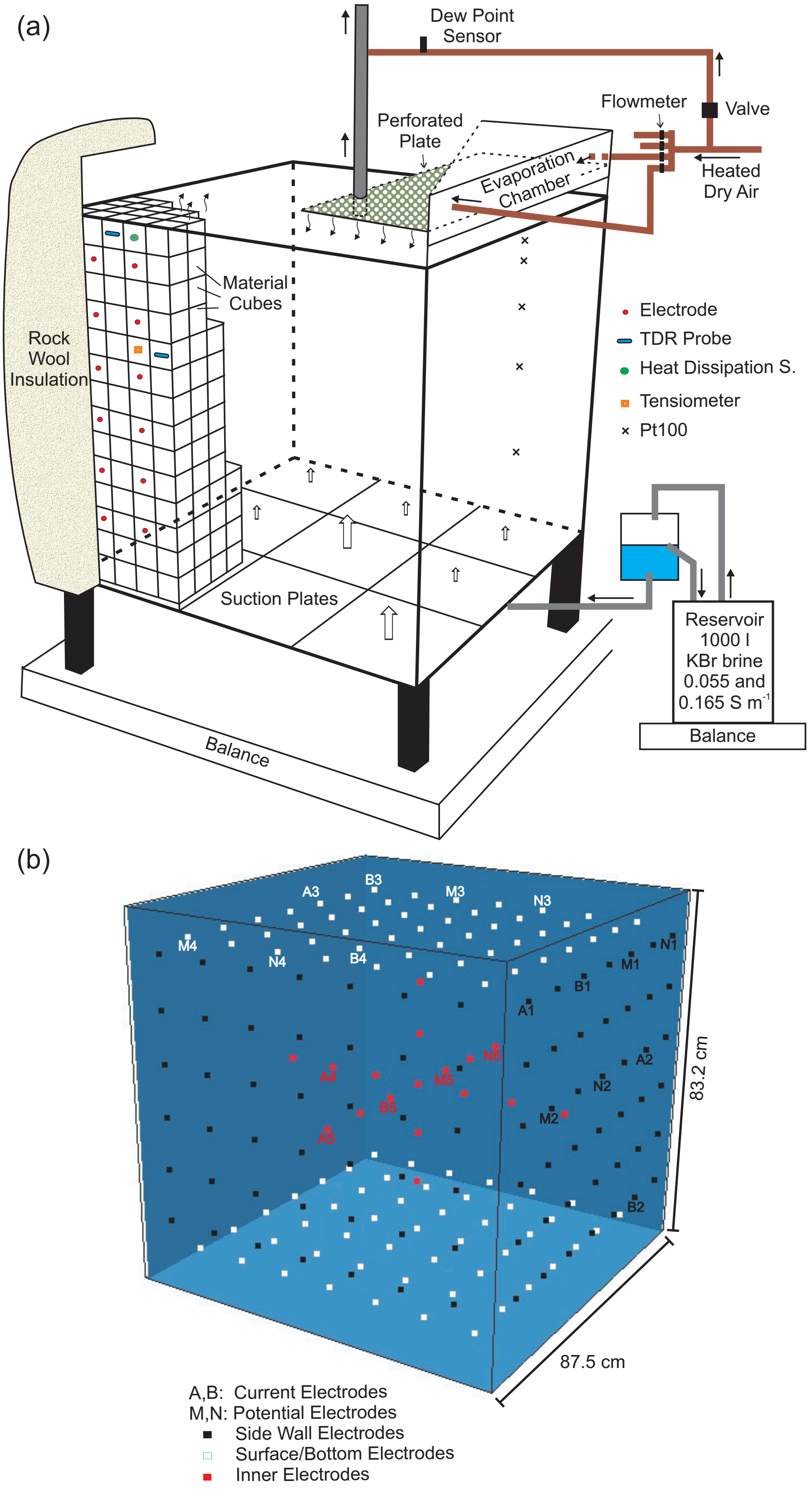

Figure 4.1: (a) Experimental setup, (b) Locations of surface and top electrodes (white), front and right side wall electrodes (black) and inner electrodes (red). Example arrays are indicated with A and B (current electrodes), M and N (potential electrodes), and the number that represents a specific array.

400 l min^{-1}. To homogenize the inflowing air, a perforated plate was installed above the soil surface. The temperature in the evaporation chamber was measured between the porous medium surface and the perforated plate, and ranged between 27 and 32 °C depending on the evaporation rate. The total evaporation rate was determined gravimetrically and by the air humidity measured with a dew point hygrometer in the in- and outflowing air. The evaporation rate at the soil atmosphere interface can be obtained from the air humidity measurements, $E_{a,tot,humidity}$ (mm d^{-1}), assuming an ideal gas,

$$E_{a,tot,humidity} = \frac{V_m^w p_{ch} Q_{air}}{R_g A} \left(\frac{f_{in}}{T_{in}} - \frac{f_{out}}{T_{out}} \right) \tag{4.1}$$

where V_m^w is the molar volume of liquid water (m^3 mol^{-1}), f_{in} and f_{out} are the molar fractions of water vapor in the inflow and outflow air (-), p_{ch} is the total pressure in the evaporation chamber (Pa), Q_{air} is the air flow rate through the system (m^3 d^{-1}), R_g is the gas constant (8.314 J K^{-1} mol^1), and A is the surface area (m^2). Since T (K) is the absolute temperature, T_{in} and T_{out} can be approximated by the average temperature in the chamber, T_{ch}.

Potential Evaporation Rate: According to Jensen et al. (1990), the reference evapotranspiration is the rate at which readily available soil water is vaporized from specified vegetated surfaces. In a similar way, we define the potential evaporation rate E_{pot} for our setup. Under the given experimental conditions, we measured a steady evaporation rate E_{wat} of 7.46 mm d^{-1} from a 2 cm thick open water body that covered the whole surface. The water body was insulated from the underlying porous medium by a 1 cm thick Styrofoam layer. At this evaporation rate, the temperature in the chamber was 27 °C and the absolute humidity of the outflowing air was 11.2 g m^{-3}. The evaporative latent heat flux was

$$J_{lat} = \lambda_v E_{wat} \rho_w \tag{4.2}$$

where λ_v is the latent heat of vaporization (2.45 MJ kg^{-1} at 20 °C), and ρ_w is the density of water (0.998 g cm^{-3} at 20 °C). During the tracer experiment, the available energy for evaporation was lowered by the heat flux J_{Hc} into the soil. Because the insulation layer between water body and soil surface inhibited this heat flux, the potential evaporation rate E_{pot} was calculated by

$$E_{pot} = E_{wat}(J_{lat} - J_{Hc})J_{lat}^{-1} \tag{4.3}$$

J_{Hc} was estimated for the steady-state upward flow conditions using the heat flux equation,

$$J_{Hc} = \kappa \frac{\Delta T}{\Delta z} \tag{4.4}$$

where κ is the average thermal conductivity of the porous medium (1.8 W m^{-1} K^{-1} for a sand with a porosity of 0.4 and a water content of 0.30 m^3 m^{-3}, (van Duin, 1963)),

Table 4.1: Van Genuchten-Mualem parameters of the coarse, medium, and fine material: θ_r = residual water content, θ_s = saturated water content, α = shape parameter, n = shape parameter, K_s = saturated conductivity, τ = tortuosity factor.

	θ_r(m^3 m^{-3})	θ_s(m^3 m^{-3})	α(m^{-1})	n(-)	K_s(cm d^{-1})	τ(-)
coarse	0.05	0.41	1.77	10.8	2496	0.73
medium	0.06	0.36	1.21	5.3	408	-0.01
fine	0.07	0.35	0.55	3.5	48	0.66

ΔT is the temperature difference between soil surface (22 °C ; average temperature of fine and medium material), and the bottom of the lysimeter (12 °C), Δz is the height of the porous medium. For the experimental setup, E_{pot} was calculated to be 6.7 mm d^{-1}.

4.2.2 Porous medium

The sandbox was filled with three different quartz sands, which are further referred to as ‘coarse’, ‘medium’ and ‘fine’. Independent estimation of the hydraulic parameters of the three materials was based on constant head infiltration (for K_s) and multistep outflow experiments (Table 4.1, Fig. 4.2b and 4.2c). The three materials were arranged to a trimodal, correlated indicator field consisting of $15 \times 15 \times 14$ cubes with a side length of 5.8 cm (Fig. 4.2a). The structure was generated using the random indicator field generator SISIM of GSLIB (Deutsch and Journel, 1998). We assumed an isotropic medium with a correlation length of 23 cm. To generate the same material distribution for both upward and downward (not shown) flow conditions, we mirrored the upper field at the horizontal plane in the middle of the sandbox.

The packing procedure was similar to the one described by Ursino et al. (2001), whereby the material was packed in frames at a predefined high bulk density (Table 4.2) to prevent secondary compaction in the sand box. In a next step, the cubes were saturated and frozen. Finally, the frozen cubes were assembled in the sand box layer by layer. At the lower end a homogeneous layer of the fine material with a thickness of 1.5 cm was inserted to homogenize possible hydraulic conductivity variations of the porous membranes. After completing each subsequent layer, the frozen soil was allowed to melt and the water table was raised to the top of this layer before inserting the next one. Due to this procedure thin gaps between the cubes were sealed. Therefore, it was not necessary to fill any gaps as done by Ursino et al. (2001).

4.2.3 Tracer experiment under evaporation conditions

Potassium bromide (KBr) dissolved in deionized water was used for the background water and the tracer solution. KBr was chosen because of the high solubility of KBr

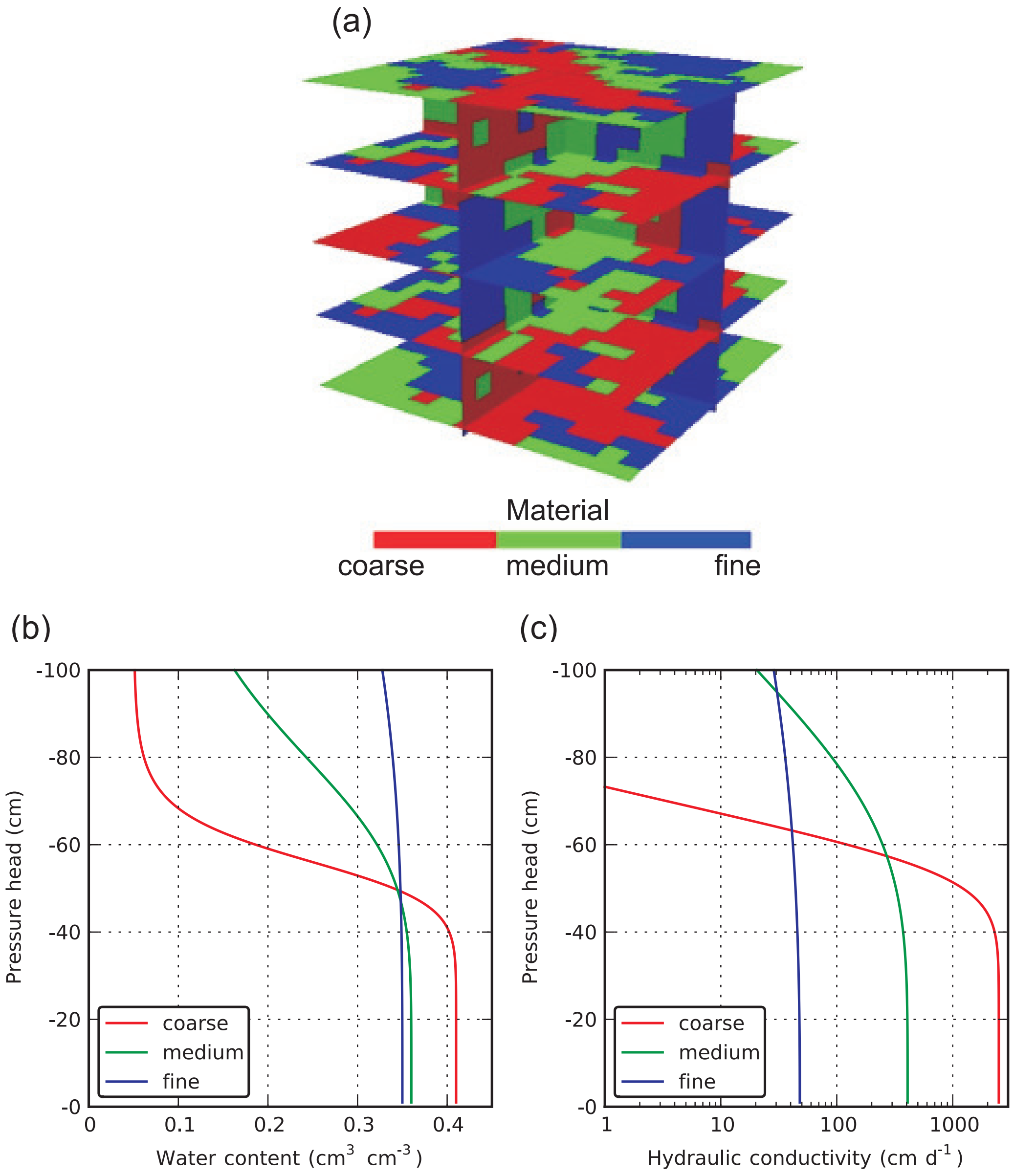

Figure 4.2: (a) Distribution of coarse (red), medium (green) and fine (blue) material cubes, (b) Water content and (c) hydraulic conductivity as a function of pressure head. Hydraulic parameters were determined with constant head infiltration (for K_s) and multi-step outflow experiments.

Table 4.2: Properties of the coarse, medium, and fine material. ρ_b = bulk density, α_L = longitudinal dispersivity, α_T = transversal dispersivity; petrophysical parameters: n_{Archie} = Archie saturation exponent, $F_{Archie,material}$ = material Archie formation factor.

	ρ_b(g cm^{-3})	α_L(m)	$\alpha_T(m)$	n_{Archie}(-)	$F_{Archie,material}$
coarse	1.48	1.7×10^{-4}	1.7×10^{-5}	1.87	3.84
medium	1.51	1.5×10^{-4}	1.5×10^{-5}	1.81	4.64
fine	1.58	0.9×10^{-4}	0.9×10^{-5}	1.41	4.38

and K_2CO_3 salts to avoid crystallization as much as possible. Prior to the experiment, the porous medium was flushed with background water with an electrical conductivity σ_w of 0.0550 S m^{-1} (at 25 °C). All electrical conductivities (and resistivities) in this chapter were transferred to 25 °C by applying

$$\sigma_{25°\mathrm{C}} = \frac{\sigma}{1 - 0.01845 \times (298.15 - T)} \tag{4.5}$$

Eq. 4.5 was determined in the laboratory for the temperature range of the experiment (10 to 25 °C). At hydrostatic equilibrium (water table 2.5 cm below the porous medium), evaporation was initiated. After 5 days, quasi-steady-state conditions established, i. e. inflow rate equaled evaporation rate. We refer to this state as quasi-steady-state conditions because a slight decrease in the evaporation rate over time occurred that was accompanied by a slow increase of temperature of the sample surface. After quasi-steady-state conditions were established the solution in the water reservoirs was exchanged (t = 5 d) with the tracer solution with σ_w of 0.165 S m^{-1}, which entered the porous medium through the suction plates. In total, about 0.76 water-filled pore volumes of tracer solution entered from day 5 until the end of the experiment at day 40.

4.2.4 Point sensors

The sand box was equipped with 24 tensiometers (T5, UMS, Germany) and 7 heat dissipation sensors (type 229-L, Campbell, USA). The tensiometers were installed horizontally at eight levels with three replicates, one located in each material (Table 4.3). The heat dissipation sensors were horizontally inserted close to the surface (Table 4.3). They were individually calibrated by the method described by Flint et al. (2002).

Additionally, a total of 39 custom-made time domain reflectometry (TDR) sensors (11 cm long) were installed next to the tensiometers into adjacent cubes of the same material and connected to a TDR100 cable tester (Campbell Scientific, Logan, UT). They were used to determine water content and bulk electrical conductivity. The TDR100 waveform acquisition and the calibration of the TDR probes were performed as suggested by Bechtold et al. (2010) (see Appendix C). Topp's equation for mineral soils (equation 7 in Topp et al., 1980) was used to calculate volumetric water content

Table 4.3: Number and locations of the point sensors and electrodes.

	Total Number	Number per Height	Height (cm)
Tensiometer	24	3	-72.9, -61.2, -49.6, -37.9, -26.2, -14.6, -8.7, -2.9
Heat dissipation sensors	7	3	-4.9, -1.1
		1	-8.4
TDR probes	39	9	-2.9
		6	-26.2, -14.6, -8.7
		3	-72.9, -61.2, -49.6, -37.9
Pt100 temperature sensors	13	8	-1.0
		1	-68.0, -46.7, -31.5, -14.5, -4.3
Electrodes	283	28	-67.0, -55.4, -43.7, -32.1, -20.4, -8.7
		49	-77.0, -7.0
		1	-65.2, -53.3, -30.2, -18.5
		13	-41.8

from dielectric permittivity. In order to avoid electrical short cuts through the TDR cables when measuring ERT, relays were built in between TDR probes and multiplexers as suggested by Koestel et al. (2008). Due to the insulation and the heated evaporation chamber, a vertical temperature profile developed which was measured by 13 Pt100 sensors (Table 4.3 and Fig. 4.1a). All point measurement devices were connected to a CR3000 Campbell data logger.

4.2.5 Time-lapse electrical resistivity tomography

4.2.5.1 Data acquisition

The spatio-temporal changes of bulk electrical conductivity σ_b were monitored using time-lapse ERT. An overview of the work flow of the ERT data processing is given in Fig. 4.3.

The ERT device (RESECS, GeoServe, Kiel, Germany) was connected via relay boxes to 283 cylindrical stainless steel electrodes of 1 cm diameter and 2 cm length with conic tip, which were located at the six sides of the sand box and along three axes within the porous medium (Table 4.3 and Fig. 4.1b). A representative selection of the applied electrode array types are given in Fig. 4.1b. In one data acquisition frame, 42830 measurements of transfer resistances were collected during 10 hours. Two frames were collected per day. Each electrode array was measured in normal and reciprocal mode for error estimation and data filtering. Electrodes were considered as point sources since simulations with real dimension showed small deviations for the filtered arrays with small geometric factors (Rücker and Günther, 2011).

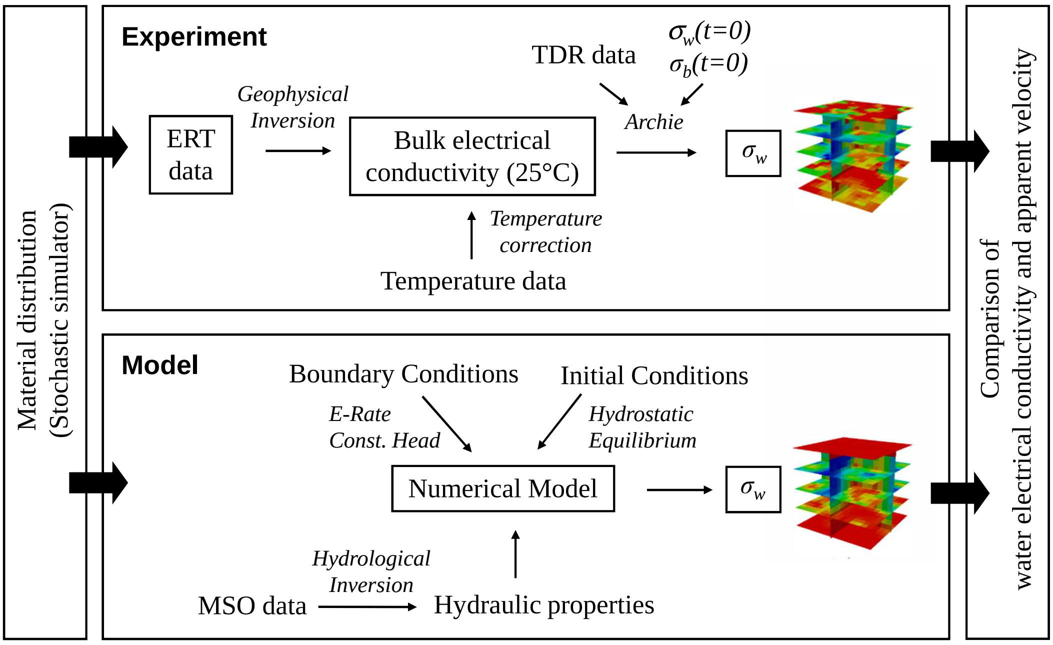

Figure 4.3: Flow chart of the main steps of the ERT processing and the numerical modeling. The comparison between experiment and model is performed for the water electrical conductivity σ_w and apparent velocity u_{app}.

4.2.5.2 Inverse problem

The forward solution for three-dimensional current flow was obtained with the finite-element approach (for details see Rücker et al., 2006). The necessary regularization in the inverse problem was addressed by adding an extra term in the objective function $\mathit{\Phi}$ that evaluates the smoothness of the inverted solution (Günther et al., 2006),

$$\mathit{\Phi}(\mathbf{m}) = \|\mathbf{W_d}[\mathbf{d} - \mathbf{f}(\mathbf{m})]\|_2^2 + \lambda\|\mathbf{W_s m}\|_2^2 \tag{4.6}$$

where $\mathbf{W_d}$ is the data weighting matrix that is defined by the measurement error (see Section 4.2.5.3), $\mathbf{d} = (d_1, d_2, \ldots, d_N)^T$ is the data vector containing N measured, log-transformed apparent resistivities, $d_i = \log(G_i R_i)$ with R_i being the transfer resistances and G_i the geometric factors, $\mathbf{m}$ is the model vector $\mathbf{m} = (m_1, m_2, \ldots, m_M)^T$ with $m_j = -\log \sigma_{b,j}$ and M being the number of model parameters, $\mathbf{f}$ is the forward operator, λ is the factor weighting the regularizing model functional, and $\mathbf{W_s}$ is the smoothness constraint operator (see Section 4.2.5.5). A Gauss-Newton scheme with global regularization was used to minimize $\mathit{\Phi}$ (for further details see Günther et al., 2006).

The regularization factor λ was set to the highest possible value still yielding a χ^2 of 1.0 for the first five data sets, where χ^2 is the error-weighted data misfit that corresponds with the first term of the right hand side of Eq. 4.6 divided by the number of measurements N. With ongoing evaporation the strong solute accumulation close to the soil surface led to increasing misfits in the ERT inversion. For these conditions, we decided to accept χ^2 values of up to 1.3, while keeping λ at the value used for the first five data sets.

We inverted the parameters on a hexahedral mesh of 15 × 15 × 28 cells, in x-, y- and z-direction, respectively. Therefore, two cells represented one material cube. The data of each time step was inverted separately, because the application of more complex time-lapse inversion strategies did not improve the inversion results.

4.2.5.3 Estimating the data error weighting matrix $\mathbf{W_d}$

The data weighting matrix $\mathbf{W_d}$ is primarily defined by measurement error, which has uncorrelated (noise due to limited precision of equipment) and correlated (electrode position error, erroneous point representation of electrode shape, varying electrode to soil contact resistance) components (Binley et al., 1995; LaBrecque et al., 1996; Oldenborger et al., 2005; Rücker and Günther, 2011). In practice, when a reliable and artifact-free σ_b distribution is sought with a final χ^2 of 1, $\mathbf{W_d}$ must also compensate for model errors. Model errors are related to the limited grid resolution and the assumption of smoothness in the presence of abrupt σ_b contrasts. Under the given complexity, the 'true' $\mathbf{W_d}$ remains largely unknown when working with real data sets. Here, we approximated $\mathbf{W_d}$ by

$$\mathbf{W_d} = \mathrm{diag}\left(\frac{1}{\log(1+\varepsilon_i)}\right) \tag{4.7}$$

where ε_i is the uncorrelated relative error. ε_i was assumed to have an absolute component, a (Ω), and a relative component, b (-) (LaBrecque et al., 1996),

$$\varepsilon_i = aR_i^{-1} + b \tag{4.8}$$

The factors a and b were estimated both by reciprocity and position error analysis. Reciprocity analysis and data filtering was performed as in Koestel et al (2008). Maximum values for the absolute and relative reciprocity error were 0.03 Ω and 0.3 %, respectively (Fig. 4.4).

The error model (Eq. 4.8) was also used in the position error analysis. Thereby, we made the simplifying assumption that the position error, which is correlated and characterized by off-diagonal entries in $\mathbf{W_d}$, can be roughly approximated by a matrix $\mathbf{W_d}$ with uncorrelated errors only. Because the misplacement of the individual electrodes is unknown, we added random noise to the positions of all electrodes with a normal distribution of zero mean and standard deviation of 3 mm, which we considered as realistic for our setup. Using the correct and erroneous electrode positions, two complete data sets were generated for all time steps by forward modeling. σ_b distributions were inferred from flow and transport simulation of the observed process (see below). The two data sets were treated as being 'normal' and 'reciprocal' for the analysis of the error model (Eq. 4.8), which described the position error well (Fig. 4.4) and resulted in maximum absolute and relative errors of 0.08 Ω and 0.5 %. Position and reciprocity error were added by adding their variances, so

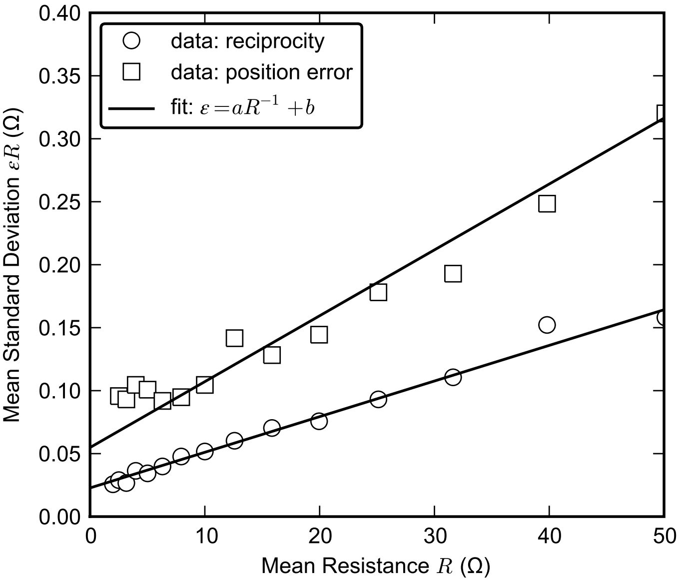

Figure 4.4: Reciprocity: Mean Standard Deviation εR of normal and reciprocal measurement plotted as a function of mean resistance R for the data in each bin. Position Error: Mean Standard Deviation εR of synthetic measurement based on correct and erroneous electrode positions plotted as a function of mean resistance R for the data in each bin. Fit is shown for the time step in which the relative error component, b, was highest.

the total error derived from both reciprocity and position error analysis was 0.09 Ω and 0.6 %, which is two to three times higher than the reciprocity error alone.

However, the estimated error level from reciprocity and position error analysis was still too low to fit the first five data frames to a χ^2 of 1. Like in previous studies (e. g., LaBrecque et al., 1996; Koestel et al., 2008), we used the estimated error level as starting point and successively scaled the factors a and b by a single factor until the χ^2 criteria was achieved. Simultaneously, we adjusted λ to obtain artifact-free solutions. Artifacts were identified by comparing the inverted σ_b distribution with the well-constrained σ_b distribution based on the material-specific TDR data and the uniform electrical pore water conductivity at day 0. The final error level, $a = 0.42$ Ω and $b = 2.8$ %, was 4.5 times higher than the error level estimated from reciprocity and position error analysis. This error level was applied to all frames.

4.2.5.4 From bulk to water electrical conductivity

Additional laboratory multi-step outflow data (not shown) indicated that matrix conduction and surface conductivity of the three materials is negligible. Thus, we transferred σ_b to water electrical conductivity σ_w by applying Archie's first and second law (1942),

$$\sigma_w = F_{Archie,app} S^{-n_{Archie}} \sigma_b \tag{4.9}$$

where S is the water saturation of the pore space (-), $F_{Archie,app}$ is the apparent

Archie's formation factor and n_{Archie} is Archie's saturation exponent. $F_{Archie,app}$ and n_{Archie} were determined for the coarse, medium and fine material. TDR derived water contents were used to estimate S, assuming that the water content measured by a single TDR probe at a certain height was representative for all cubes of the same material in the same layer. Flow and transport modeling results indicated that this is a valid assumption during the experiment. Between two measurement heights, S was interpolated linearly.

Using the water content and $\sigma_{b,TDR}$ measurements from all TDR probes, n_{Archie} was determined by fitting

$$\log_{10}\left(\frac{\sigma_w}{F_{Archie,material}\sigma_{b,TDR}}\right) = -n_{Archie}\log_{10}(S) \tag{4.10}$$

where the material formation factor, $F_{Archie,material}$, was determined using $\sigma_{b,TDR}$ from the three TDR probes at the lowermost level, and assuming full saturation $S^{-n_{Archie}} = 1$ and $\sigma_w = 0.055$ S m^{-1} prior to tracer injection.

Due to the smoothing related to the regularization, the material-specific petrophysical parameters are not directly applicable to transfer ERT-derived σ_b to σ_w (Slater et al., 2002; Singha and Gorelick, 2006). Alternatively, apparent parameters that account for the smoothing errors can be determined for a well-defined state of the system (Slater et al., 2002). However, they are only an approximation for the remaining time of the experiment, because the smoothing effect changes with time (Singha and Gorelick, 2006). In our laboratory soil, changes in S were minor, thus we kept n_{Archie} as material-specific parameter and used it to determine the voxel-scale apparent formation factor $F_{Archie,app}$, by applying σ_b at $t = 0$, $\sigma_w = 0.055$ S m^{-1}, and S from the TDR water contents. The spatially-variable $F_{Archie,app}$ was subsequently applied in Eq. 4.9 for all time steps.

4.2.5.5 Using structural constraints in the smoothness constraint operator $\mathbf{W_s}$

Goal of the smoothness-constrained inversion is to find the smoothest distribution of the log-transformed σ_b that describes the data within the measurement error. For the porous medium in this study, which is characterized by numerous sharp contrasts of σ_b, especially in the upper unsaturated part of the porous medium, it is evident that the smoothest model is not the 'best'.

A method to include a priori information about the structure of the medium and the process in the ERT inversion is to adapt the smoothness constraint operator $\mathbf{W_s}$ (Günther et al., 2006). We compared the inversion results in which the knowledge about structure was used as constraint (named 'SC') with the one in which the structure was not considered (named 'No SC'). The knowledge about the heterogeneity of the porous medium was included by treating all material interfaces with a model control reduced by a factor of 0.3. Equally, we reduced model control at the interface between the first and second voxel layer (-2.9 cm below the surface) in order to permit an abrupt increase of σ_b close to the soil surface that occurs with ongoing accumulation of dissolved bromide due to evaporation. Tests with smaller factors than 0.3 led to noisy distributions of σ_b with numerous artifacts.

4.2.5.6 Obtaining local evaporation rates from electrical resistivity tomography

We used the increase of water electrical conductivity in the uppermost material cubes to estimate the spatial variability of evaporation rates. From 0.0 S m^{-1} to 8.0 S m^{-1} (factor 50 higher than the tracer solution), we confirmed that the KBr concentrations were linearly related to water electrical conductivity. Thus, the rate of increase of solute mass, Δm, in material cube i of the uppermost cube layer was calculated by

$$\Delta m_i = \frac{\Delta \sigma_{w,i} \theta_i}{\Delta t V_c} \tag{4.11}$$

where V_c is the volume of a material cube (cm^3), $\Delta \sigma_w$ is the increase of the water electrical conductivity (S m^{-1}), and θ is the water content (m^3 m^{-3}). The evaporation rate, E_a, from each material cube was obtained as

$$E_{a,i} = \frac{\Delta m_i}{\sigma_0 A_c} \tag{4.12}$$

where σ_0 is the background water electrical conductivity (S m^{-1}) and A_c is the area of a side of the material cube (m^2). This approach was based on several assumptions: (1) in the uppermost cube layer solute fluxes were only vertical, (2) water content variation was negligible, (3) KBr remained dissolved in the water, (4) back diffusion was not high enough to distribute accumulated solutes below the first cube layer, (5) tracer solution did not yet arrive in the surface area, and (6) the ERT inversion captured the full magnitude of the increase of the water electrical conductivity. Under the given assumptions, the approach is best applicable in the early stages of the evaporation experiment. Thus, we applied it for the time span from day 5 until day 6, just after quasi steady-state conditions have been established.

4.2.6 Numerical simulation of flow and transport

4.2.6.1 Numerical model

For the simulation of the water flow a three-dimensional cell-centered finite-volume (FV) code was used (e. g., Ippisch et al., 2006; Rossi et al., 2008; Carminati and Flühler, 2009; Bechtold et al., 2011b) which solves the Richards' equation (Richards, 1931),

$$\frac{\partial \theta(h)}{\partial t} = -\nabla \cdot \theta \mathbf{u} = [K(\theta) \nabla h] + \frac{\partial K(\theta)}{\partial z} \tag{4.13}$$

where t is time (d), h is pressure head (cm), θ is volumetric water content (m^3 m^{-3}), $\mathbf{u}$ is the pore water velocity vector (cm d^{-1}), K is hydraulic conductivity (cm d^{-1})

and z is the vertical coordinate directed positively upwards (cm). $\theta(h)$ and $K(\theta)$ were described by the van Genuchten-Mualem (vGM) parametric expressions (van Genuchten, 1980) (Table 4.1).

Solute transport was described by the advection-dispersion equation (ADE),

$$\theta\frac{\partial C}{\partial t} = -\theta\mathbf{u}\cdot\nabla C + \nabla\cdot(\theta\mathbf{D}\cdot\nabla C) \tag{4.14}$$

where C is solute concentration in pore water (kg cm^{-3}), $\mathbf{D}$ is the local-scale dispersion tensor of an isotropic porous medium (cm^2 d^{-1}), with $\mathbf{D} = (\alpha_T\|\mathbf{u}\|+D_m)\,\mathbf{I} + (\alpha_L-\alpha_T)\,\mathbf{u}\mathbf{u}^T\|\mathbf{u}\|^{-1}$, where α_T and α_L are the transversal and longitudinal dispersivities (cm), D_m is the effective molecular diffusion coefficient (cm^2 d^{-1}), and $\mathbf{I}$ is the identity matrix. We set α_L to the mean grain size and α_T to 1/10 of α_L (Table 4.2), which are typical values reported for saturated unconsolidated homogenous porous media (Greiner et al., 1997; Yoon et al., 2008; Lamy et al., 2009). Water content dependence of α_L and α_T was neglected, because D_m was more than one order of magnitude higher than the mechanical dispersion in the experiment. The diffusion coefficient $D_{m,w}$ of KBr in water was assumed to be 2.05×10^{-9} m^2 s^{-1} (Kasteel et al., 2002) and was multiplied by the tortuosity factor evaluated as a function of water content using the relationship of Millington and Quirk (1961) in order to obtain D_m.

Solute transport was modeled using the random walk particle tracking (RWPT) code PARTRACE, which is based on the equivalent stochastic differential version of Eq. 4.14 and uses an improved algorithm that accurately accounts for discontinuous dispersion tensors and water contents (Bechtold et al., 2011b). Water flow and solute transport were simulated on a rectilinear grid ($60 \times 60 \times 63$ elements) with decreasing vertical element size to the surface (down to 1 mm). Element boundaries were placed just at the interfaces of the material cubes. Because hydraulic properties are defined element-wise in the cell-centered FV approach, the model domain did exactly reproduce the sharp interfaces. Convergence in the RWPT solution was achieved by gradually increasing the number of particles (3.5×10^8 particles) and decreasing the time step size ($\Delta t = 0.025$ d).

The lower boundary of the experiment was described by a prescribed pressure head depending on the imposed water table level (-2.5 cm). The four side walls were modeled as no flow boundary condition. Throughout this chapter, modeled solute concentration is presented as water electrical conductivity, which is then used for comparison with the monitoring results.

4.2.6.2 Evaporation boundary condition

Evaporation from the heterogeneous surface was modeled with two different approaches. The first approach is the classical potential/actual evaporation boundary condition (‘E_{pot}/E_a no compensation’). Here, we applied the previously determined potential evaporation E_{pot} as a constant for the whole experimental period. If a critical pressure head (here: -10^5 cm) was reached at the top of the uppermost element, the Neumann switched to the Dirichlet boundary condition. At this location, the actual evaporation rate dropped below the potential evaporation rate.

In the second approach, we directly applied the measured gravimetrical evaporation rate as potential evaporation rate (‘E_{pot}/E_a compensation’). If a critical pressure head was locally reached, the actual evaporation rate dropped also below the potential evaporation rate at this location, however, the flux deficit was compensated uniformly by all other elements. Thus, the local decrease of the evaporation rate led to the global enhancement of the potential evaporation rate. This approach assured that the modeled total actual evaporation rate equals the measured one. If not mentioned otherwise, we used the simulation data of this approach for the comparison with the experimental data.

4.2.7 Generation and inversion of synthetic electrical resistivity tomography data

Deviations between monitored and modeled water electrical conductivities σ_w can be caused by uncertainties and errors at the monitoring and/or the modeling side of the workflow (Fig. 4.3). It is well-known that ERT-derived σ_w distributions are highly uncertain because of measurement errors, smoothness constraint errors, and errors related to spatially and temporally-varying apparent petrophysical parameters (Slater et al., 2002; Singha and Gorelick, 2006; Koestel et al., 2008). To evaluate the error of the ERT-derived σ_w distributions, we performed synthetic ERT experiments.

First, the flow and transport process was modeled by applying the defined structure and properties of the porous medium as well as the experimental boundary conditions. σ_w obtained from the numerical model (‘E_{pot}/E_a compensation’) represented the ‘true’ solution. Second, using the ‘true’ solution, we generated a synthetic set of time-lapse ERT data. Therefore, modeled σ_w were transformed to σ_b by the use of the material-specific petrophysical parameters. Afterwards, we applied the ERT forward operator to the resulting distribution of σ_b and to the same arrays that were used in the inversion of the experimental ERT data. The forward modeling resulted in a first data set of noise-free time-lapse ERT data, further referred to as ‘ERT synth. (no error)’. A second data set, further referred to as ‘ERT synth. (exp. error)’, was generated by adding zero-mean uncorrelated Gaussian random noise with a standard deviation that corresponded to the error level that was necessary to fit the experimental data to a χ^2 of 1 ($a = 0.42\ \Omega$ and $b = 2.8$ %, see above). The resulting data sets were inverted and the inversion results were processed as done for the experimental data (see above). The comparison between the inversion results of σ_w and the ‘true’ distribution of σ_w provides an approximation of the resolving power of ERT in our experimental setup.

4.2.8 Solute transport analysis

4.2.8.1 Comparison of monitored and modeled solute transport

We used the defined boundary conditions and the known structure and hydraulic properties of the porous medium to set up a fully-distributed 3-D numerical flow and transport model of the tracer experiment. Model results were compared in detail with monitoring data. An overview of the workflow is given in Fig. 4.3. In order to compare monitored and modeled solute transport, we chose the size of a material cube as scale of comparison throughout the rest of this study. The voxel-scale ERT-derived and modeled water electrical conductivities were used to determine the water electrical conductivity for each material cube.

In a first step, the 80 ERT-derived images of water electrical conductivity were directly compared with the modeled water electrical conductivity. However, absolute values of water electrical conductivity obtained from ERT are considerably flawed due to smoothing errors and spatially and temporally variable apparent petrophysical parameters. Therefore, in a second step, we additionally used apparent velocity u_{app} for comparison. Values of u_{app} were expected to be less dependent on the absolute values of σ_w derived from ERT and thus were supposed to be more robust for comparing the main transport characteristics of the monitored and modeled data. The spatial distribution of u_{app} was derived by fitting the solution of the one-dimensional form of the ADE (Eq. 4.14) for a 3rd type boundary condition and a step tracer application (van Genuchten and Parker, 1984) to the monitored and modeled time series of σ_w of each material cube.

4.2.8.2 Leaching surfaces

A tool to characterize the spatial and temporal spreading of solutes in heterogeneous porous media is the analysis of leaching surfaces (de Rooij and Stagnitti, 2002). A leaching surface is a three-dimensional representation of the complete set of local-scale breakthrough curves (BTC) at some control plane. The BTCs that form a leaching surface are based on solute flux and a Dirac pulse application. To obtain leaching surfaces from our data, we basically followed the approach described in Garré et al. (2010) to transfer our ERT-derived time-lapse data of resident concentrations of a step tracer application to solute fluxes resulting from a Dirac pulse. We used the fitted u_{app} (see above) to calculate time series of resident concentrations $C(\mathbf{X}, t)$ for a Dirac tracer application and a 1st type boundary condition using the corresponding analytical solution of the ADE. The normalized solute flux, J_s (m^{-2} d^{-1}), was obtained as

$$J_s(\mathbf{X}, t) = \frac{C(\mathbf{X}, t)}{M_0} u_{app}(\mathbf{X}) \theta(\mathbf{X}) \tag{4.15}$$

where M_0 is the 0th moment representing the total applied solute mass (kg). Bloem et al. (2008) evaluated the potential and limitations of the methodology that we chose to

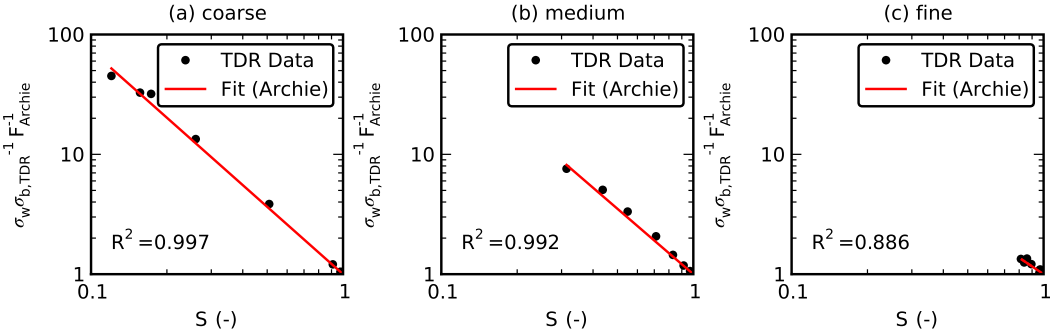

Figure 4.5: Determination of Archie's saturation exponent n_{Archie} for the coarse (a), medium (b), and fine (c) material. The linear model describing the relationship between $\log_{10}(\sigma_w \sigma_{b,TDR}^{-1} F_{Archie,material}^{-1})$ and $\log_{10}(S)$ through the origin (0,0) was fitted to the TDR data collected at time $t = 0$.

derive solute fluxes from local resident concentrations by the use of temporal moment analysis. According to their findings, the presented leaching surfaces cannot be evaluated in all quantitative details but should rather serve as a tool to qualitatively illustrate the transport phenomena of the upward transport experiment.

In Eq. 4.15, the volumetric water content $\theta(\mathbf{X})$ was given by the TDR measurements for the experimental BTCs and by the modeled water contents for the modeled BTCs. The material cubes in the control plane where then ranked in order of descending amount of cumulative leaching $\int_0^\infty J_s(\mathbf{X},t)dt$. A curved surface was obtained by plotting all BTCs in a 3-D diagram, where the horizontal x-axis is the cumulated area of the sorted pixels, the horizontal y-axis is the time and the vertical z-axis is the scaled solute flux $Surf(\mathbf{X},t)$. $J_s(\mathbf{X},t)$ was scaled, so that the resulting leaching surface integrates to unity,

$$Surf(\mathbf{X},t) = J_s(\mathbf{X},t)\left(\int_0^\infty \int_0^{87.5} \int_0^{87.5} J_s(\mathbf{X},t)dx_1 dx_2 dt\right)^{-1} \tag{4.16}$$

4.3 Results and discussion

4.3.1 Petrophysical parameters and effect of structural constraints

The TDR data at $t = 0$ d were described well by using the Archie model (Eq. 4.10 and Fig. 4.5). The water content range that was covered in the fitting differed among the three materials. However, the water content distribution under quasi-steady-state upward flow conditions did not deviate much from the one at hydrostatic equilibrium at $t = 0$ d, thus n_{Archie} can be considered as representative for the experimental conditions.

To evaluate the effect of the structural constraints, the ERT-derived σ_b distributions at $t = 0$ d were compared with the σ_b distribution obtained from the TDR water contents and petrophysical parameters, which we considered as reliable ground

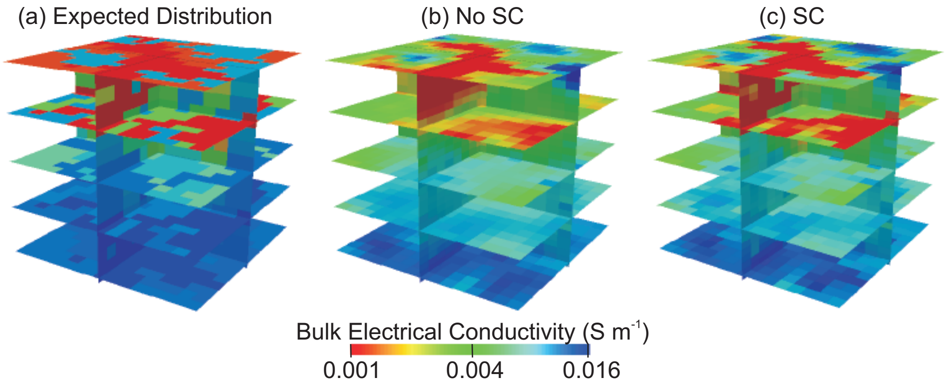

Figure 4.6: Bulk electrical conductivity distribution at time $t = 0$, (a) as expected from TDR water contents and the material-specific petrophysical parameters, (b) as obtained from the 'No SC' (no structural constraints) ERT inversion and (c) from the 'SC' (structural constraints) ERT inversion in which the knowledge about the structure was included.

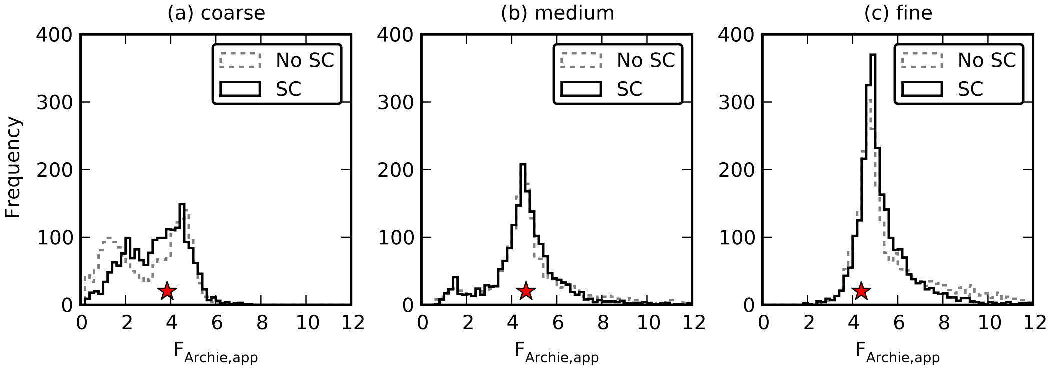

Figure 4.7: Frequency distribution of the apparent formation factor $F_{Archie,app}$ for the coarse (a), medium (b), and fine (c) material when using the 'No SC' (no structural constraints) and the 'SC' (structural constraints) approach. The red star indicates the material formation factor $F_{Archie,material}$ obtained from the TDR data.

truth for the hydrostatic equilibrium conditions at the beginning of the experiment. Fig. 4.6 demonstrates that the inversion in which the knowledge about structure is used as constraint (named 'SC') provided an image that is much closer to the ground truth. In contrast, the inversion result in which the structure was not considered (named 'No SC') shows very smoothed contrasts. Fig. 4.7 demonstrates the large variation of the derived apparent formation factors $F_{Archie,app}$ around the material formation factors $F_{Archie,material}$. It also shows that the 'SC'-approach provides a slightly narrower distribution of $F_{Archie,app}$ that is closer to the value $F_{Archie,material}$. The smoothing error that is the primary reason for the application of apparent formation factors is reduced by the improved model control in the 'SC'-approach. We used the more robust results of the 'SC'-approach to process the time-lapse ERT data.

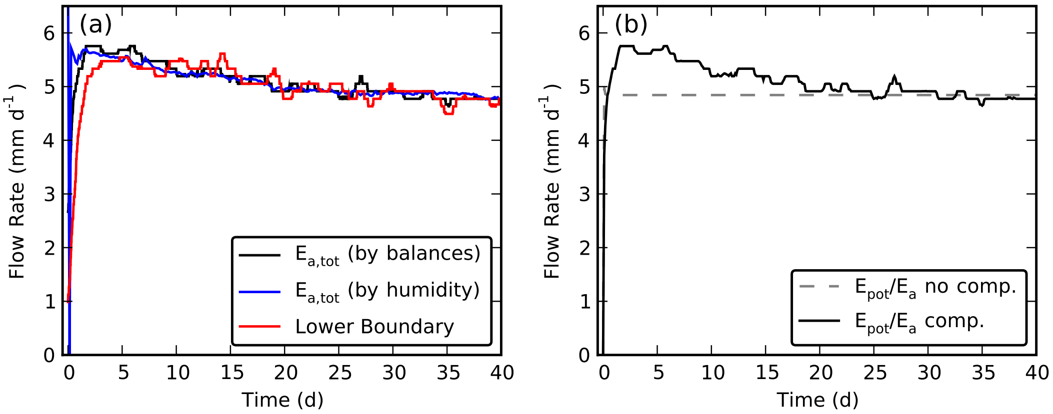

Figure 4.8: (a) Measured total evaporation rate $E_{a,tot}$ (by balances and humidity) and measured flow rate through the lower boundary over the 40 days period of the experiment, (b) evaporation rate as modeled by the classical potential/actual evaporation (‘E_{pot}/E_a no compensation’) and the ‘E_{pot}/E_a compensation’ approach in which lateral evaporation compensation is possible.

4.3.2 Total and material-specific evaporation rates

The total evaporation rate was the only evaporation flux that was directly measured during the experiment by the use of balances and humidity sensors. The two techniques showed the same temporal evolution of the total evaporation flux (Fig. 4.8a). After a quick increase of the evaporation rate to about 5.7 mm d^{-1} at the beginning of the experiment, the rate decreased continuously down to 4.8 mm d^{-1} towards the end. Because the heating device and air flow rate were stable throughout the experiment, technical reasons for this decrease can be excluded. Instead, the decreasing evaporation rate can be explained by the decreasing osmotic potential with increasing salt concentration due to evaporation (Nassar and Horton, 1999; Fujimaki et al., 2006). Because the background water was saline too, the concentration increased immediately after evaporation started. Assuming constant temperature and humidity of the outflowing air, we followed the approach given in Fujimaki et al. (2006) to approximate the decrease of the evaporation rate ΔE_{osm} with decreasing osmotic potential by applying

$$\Delta E_{osm} = \frac{\rho_{vs}(rH_{\mathrm{s},1} - rH_{\mathrm{s},2})}{r_a} \tag{4.17}$$

where ρ_{vs} is the saturated water vapor density (g cm^{-3}), r_a is the aerodynamic resistance (1.3 s cm^{-1}) that was determined for the initial evaporation rate when osmotic effects were negligible (Fujimaki et al., 2006, Eq. 2 therein), and $rH_{\mathrm{s},1}$ and $rH_{\mathrm{s},2}$ are the relative humidity at the soil surface at the start ($t = 5$ d) and at the end of the tracer experiment, respectively. $rH_{\mathrm{s},1}$ and $rH_{\mathrm{s},2}$ were calculated by the approach introduced by Philip and de Vries (1957),

$$rH_{\mathrm{s}} = \exp\left(\frac{h + h_{osm}}{R_v T_{surf}}\right) \tag{4.18}$$

where h_{osm} is the osmotic potential (cm), R_v is the gas constant for water vapor (4697 cm K^{-1}) and T_{surf} is the temperature at the soil surface (K). h_{osm} was approximated as in Fujimaki et al. (2006). For our experimental setup, we obtained that the evaporation rate would have decreased by 38 % at saturation concentration of KBr (36 wt. %), which is similar to values reported by Fujimaki et al. (2006) that ranged from 25 to 40 % for NaCl and KCl. The experimentally observed decrease of the total evaporation rate was only 16 %. The lower decrease indicates that, if at all, saturation concentration of KBr was reached only locally. Additionally, the decrease in the evaporation rate was accompanied by an increase of the temperature in the evaporation chamber from 30 to 32 °C, which is a counter-acting effect. Fig. 4.8a also shows the quasi-steady conditions that established after 5 days, when the inflow rate through the bottom boundary approached the evaporation rate.

Experimental observations indicate that evaporation from the surface was spatially variable. Directly after the experiment presented in this chapter, the suction plates were closed, thus the inflow was inhibited, and the drying of the porous medium due to evaporation was monitored. This experiment is not presented here, however, the soil sampling at the end of this drying sequence showed that no salt accumulated in the uppermost coarse material cubes. This observation indicates that salts also did not accumulate during the steady-state upward flow period of this study. The observation was supported by the ERT data, which did show a strong decrease of bulk electrical conductivity in the coarse material during the first day and only a slight increase of water electrical conductivity σ_w during the rest of the experiment. The slight increase of σ_w was probably caused by smoothing errors related to the overall increase of σ_w close to the surface. The drying of the coarse material and the loss of liquid continuity was also indicated by the uppermost tensiometer and the heat dissipation sensors that showed decreasing pressure heads until they lost hydraulic contact after day 1.

Thus, after one day, evaporation from the coarse material can be considered as ‘stage-2’ evaporation. As demonstrated by Shokri et al. (2008a), the evaporation flux under ‘stage-2’ evaporation is supported by vapor diffusion, and the evaporation rate is proportional to the diffusion length to the surface. Assuming a diffusion length of 5.8 cm, which is the height of the cubes for which we did not observe any salt accumulation, we obtained an evaporation rate from the coarse material of about 0.2 mm d^{-1} (Shokri et al., 2008a, Eq. 1 therein).

The coarse material represented 31 % of the total sample surface. By assuming an evaporation rate of 0.2 mm d^{-1} for this material, the evaporation from the remaining part $E_{fine+medium}$ (69 % of total surface) can be calculated. During the first days of the experiment $E_{fine+medium}$ was

$$E_{fine+medium} = \frac{5.7\text{mm d}^{-1} - 0.31 \times 0.2\text{mm d}^{-1}}{0.69} = 8.2\text{mm d}^{-1} \tag{4.19}$$

Surprisingly, $E_{fine+medium}$ was higher than the potential evaporation rate of the experimental setup (E_{pot} = 6.7 mm d^{-1}). Thus, the drop in the evaporation from the coarse material was compensated by an increased evaporation from the fine and medium one. The given evaporation rates indicate that the drop of the evaporation rate from the coarse material was compensated with 50 % by the medium and fine material. Two compensation mechanisms could have caused the local increase of the actual evaporation rate (1) the flux of thermal energy away from the coarse material that was at 1 cm depth 4 to 6 °C hotter than the fine and medium material and (2) the lower humidity and higher temperature of the air in the evaporation chamber due to the lower total evaporation during the experiment (abs. humidity 8.6 g m^{-3} and 30 °C) compared to the evaporation during the determination of E_{pot} (abs. humidity 11.2 g m^{-3} and 27 °C). These conditions caused a small-scale 'oasis effect' during the experiment. Based on the measured data it was not possible to quantify the two compensation mechanisms with sufficient accuracy.

The numerical flow model predicted that the evaporation from the coarse material quickly approaches very low evaporation rates (Fig. 4.9b). However, the experimentally observed compensation cannot be reproduced by the classical 'E_{pot}/E_a no compensation' approach (Fig. 4.8b). Because no compensation was possible, the total evaporation rate was underestimated. In comparison, the 'E_{pot}/E_a compensation' approach made it possible to reproduce the total evaporation rate exactly.

4.3.3 Evaporation pattern derived from electrical resistivity tomography

The evaporation pattern obtained by applying Eq. 4.11 and 4.12 to the ERT-derived solute accumulation showed a strong underestimation of the total evaporation by a factor of 10. We assume that the highest error was probably caused by the accumulation of solutes in a very thin layer close to the surface that could not be reproduced by the ERT inversion mesh. Therefore, we scaled the local evaporation rates by a factor of 10 so that the measured total evaporation was reproduced.

The resulting ERT-derived evaporation pattern is basically consistent with the other experimental observations (higher temperature in coarse material, loss of liquid continuity in coarse material as indicated by tensiometer and heat dissipation sensors). It also indicates that evaporation from the coarse material practically ceased (Fig. 4.9e). It seems that the pattern additionally allows a differentiation of the evaporation rates of the medium and fine material. The fine material is in most parts characterized by a higher evaporation rate than the medium material. Using the synthetic ERT data, we tested the reliability of this observation. The evaporation pattern obtained from the synthetic ERT inversion (Fig. 4.9d) indicated the same tendency of higher evaporation from the fine material, although these differences were absent in the evaporation pattern of the numerical flow model on which the synthetic inversion was based (Fig. 4.9b).

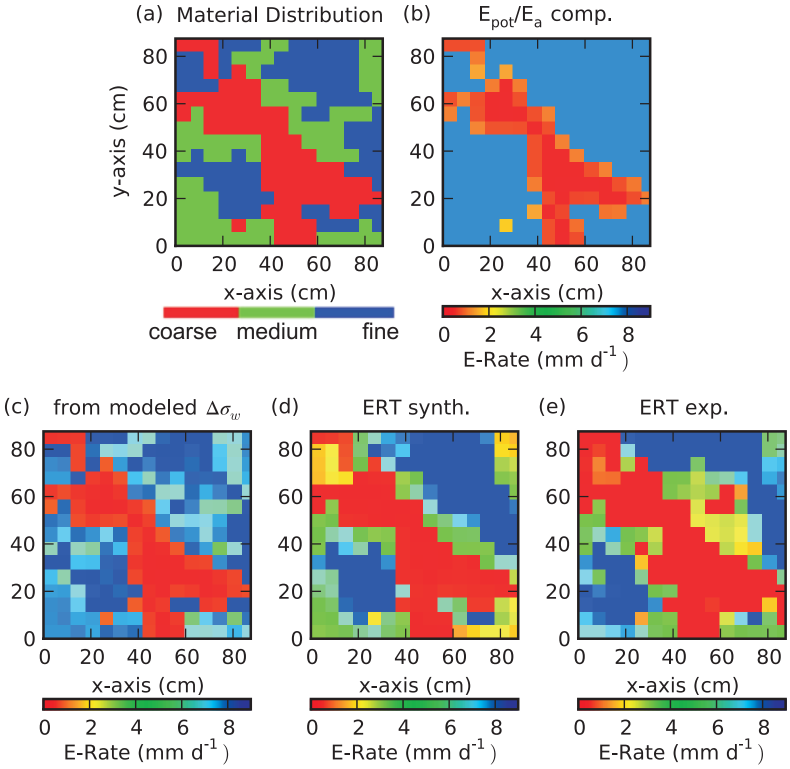

Figure 4.9: (a) Material distribution at the soil surface; evaporation rates (E-Rate) at the soil surface, (b) modeled with the E_{pot}/E_a compensation approach, (c) derived from the modeled increase of water electrical conductivity in the uppermost layer, (d) derived from the inversion results of the synthetic ERT data with experimental error, and (e) derived from the inversion results of the experimental data.

We found that one assumptions was violated during the derivation of the evaporation pattern. The numerical model indicated lateral water fluxes from the medium into the fine material within the uppermost material cubes. Bechtold et al. (2011a) demonstrated that near-surface lateral water fluxes occur when liquid continuity is still sustained and hydraulic conductivity is spatially variable close to the soil surface. In combination with back diffusion from the zone of solute accumulation downwards, these near-surface lateral water fluxes lead to an increased solute accumulation in the material with the lowest hydraulic conductivity, which is the fine material under the experimental conditions. Fig. 4.9c shows the evaporation rates obtained by directly applying Eq. 4.11 and 4.12 to the modeled water electrical conductivities. Higher evaporation rates from the fine material are already indicated in this pattern. Consequently, the evaporation patterns obtained from the synthetic ERT experiment (Fig. 4.9d) also indicate higher evaporation rates from the fine material. Based on the experimental data it was not possible to clarify whether besides this effect, differences in the evaporation rates between the medium and fine material really occurred. Therefore, the analysis demonstrated the value of synthetic ERT inversions to evaluate the information content of the experimental ERT data.

4.3.4 Comparison of monitored and modeled solute transport

Monitored and modeled tracer distributions after 10, 20, 30, and 40 days are plotted for different heights in Fig. 4.10b. The time-lapse data clearly shows that upward transport was not uniform but occurred along preferential pathways that were controlled by the material distribution (Fig. 4.10a). A detailed discussion of the preferential pathways is given in Section 4.3.6. Further, Fig. 4.10b shows that the main preferential flow pathways that were derived from the ERT data and the flow and transport simulations correspond quite well. The quantitative comparison between monitored and modeled water electrical conductivities at the scale of the material cubes showed good correlation in the lower part of the porous medium (height: -60 cm, Fig. 4.11a), whereas in the upper part the deviations are higher (height: -20 cm, Fig. 4.11b). Note that the comparison at the two heights was done for different times to assure that the full range of water electrical conductivities was covered at both heights. The highest deviations occurred for the surface layer, where the ERT-derived water electrical conductivities are much lower than the modeled ones (Fig. 4.10b), as already discussed in the previous section.

Because the direct comparison of water electrical conductivities might be biased by inversion artifacts, the fitted apparent velocities u_{app} were used instead for a more robust comparison between monitored and modeled data (Fig. 4.10c). In Fig. 4.11c and 4.11d, the experimental apparent velocities $u_{app,exp}$ are plotted vs. the modeled apparent velocities $u_{app,mod}$ for each material cube of the layer at -60 cm and -20 cm height, respectively. Like in the comparison of the water electrical conductivities, the experimental and modeled apparent velocities correlated well in the lower part of the laboratory soil whereas in the upper part the correlation was lower.

4.3.5 Reasons for deviations between monitored and modeled solute transport

Deviations between the monitored and modeled solute transport can be attributed to both observational and model errors. On the observational side, uncertainties in the petrophysical parameters and spatial smoothing inherent to the imaging algorithm contributed to observed deviations between ERT and simulation results. On the model side, uncertainties about the top surface boundary condition and about the hydraulic properties of the three materials may contribute to differences between ERT and simulation results.

We addressed the question whether the discrepancies can be attributed exclusively to ERT error by comparing the model results with the inversion results of the different ERT data sets, namely the experimental and the synthetic ERT data ('exp. error' and 'no error'). Fig. 4.12 shows the correlation coefficient between the ERT-derived and the modeled ('E_{pot}/E_a compensation') u_{app} for all heights and the different ERT data sets. In general, the synthetic experiments indicate deviations between

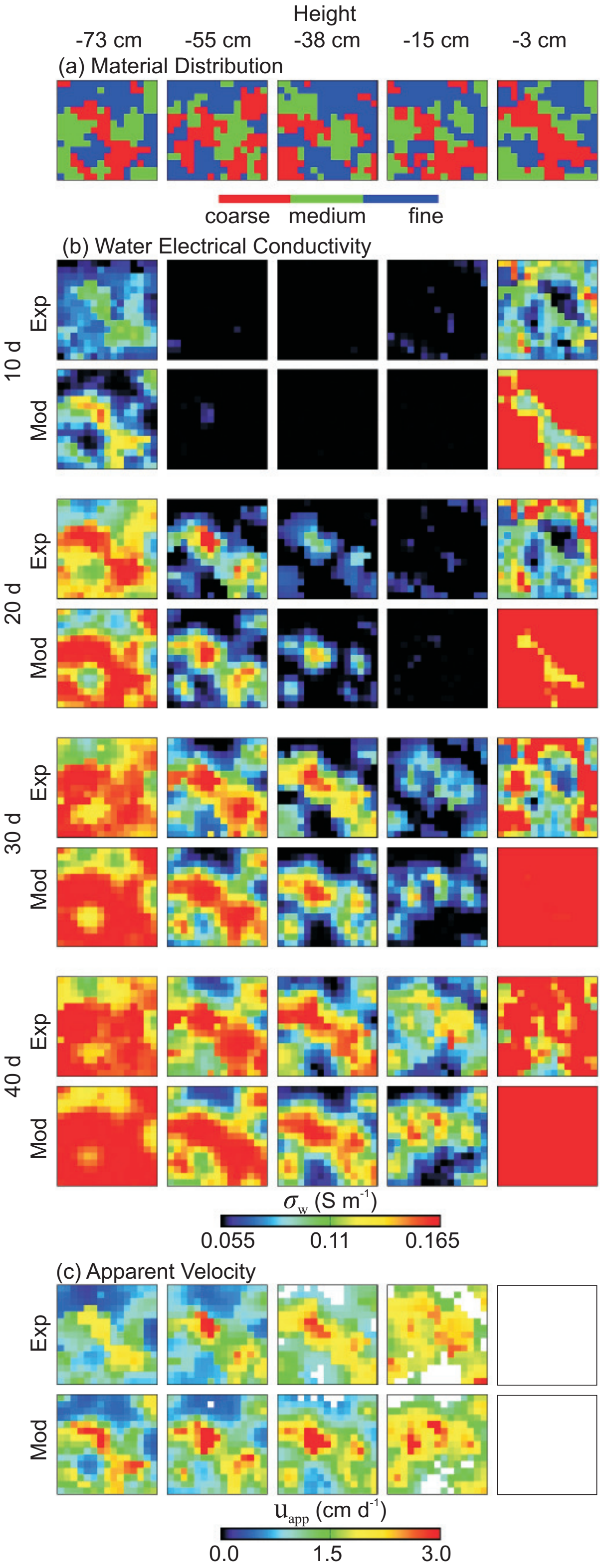

Figure 4.10: Horizontal cross sections at different heights of (a) material distribution, (b) ERT-derived experimental (Exp) and modeled (Mod) water electrical conductivity σ_w at different times (10, 20, 30, and 40 days), and (c) ERT-derived experimental and modeled apparent velocity u_{app}. The numerical flow and transport was based on the 'E_{pot}/E_a compensation' approach. White color in (c) indicates regions where the fitting of the BTC yielded an $R^2 < 0.8$.

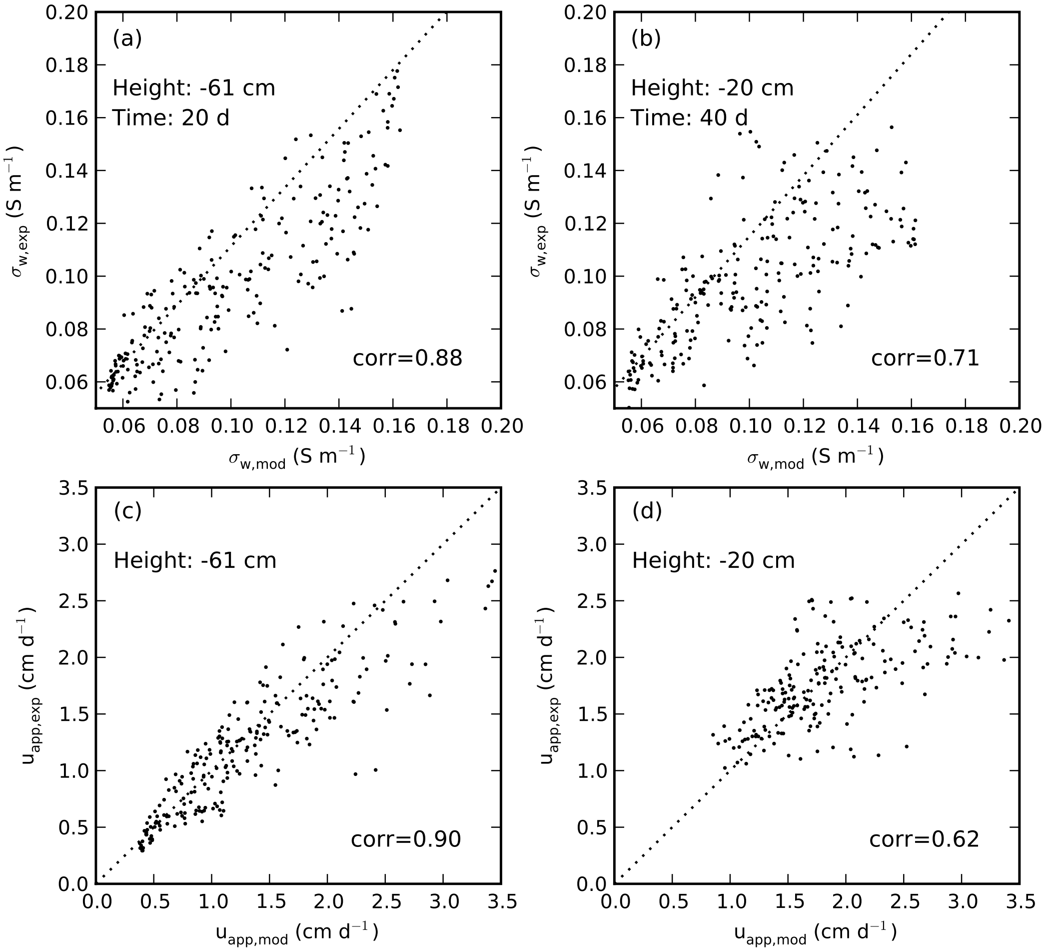

Figure 4.11: Experimental vs. modeled water electrical conductivity σ_w, (a) and (b), and experimental $u_{app,exp}$ vs. modeled apparent velocity $u_{app,mod}$, (c) and (d), for two different heights (and times in case of σ_w).

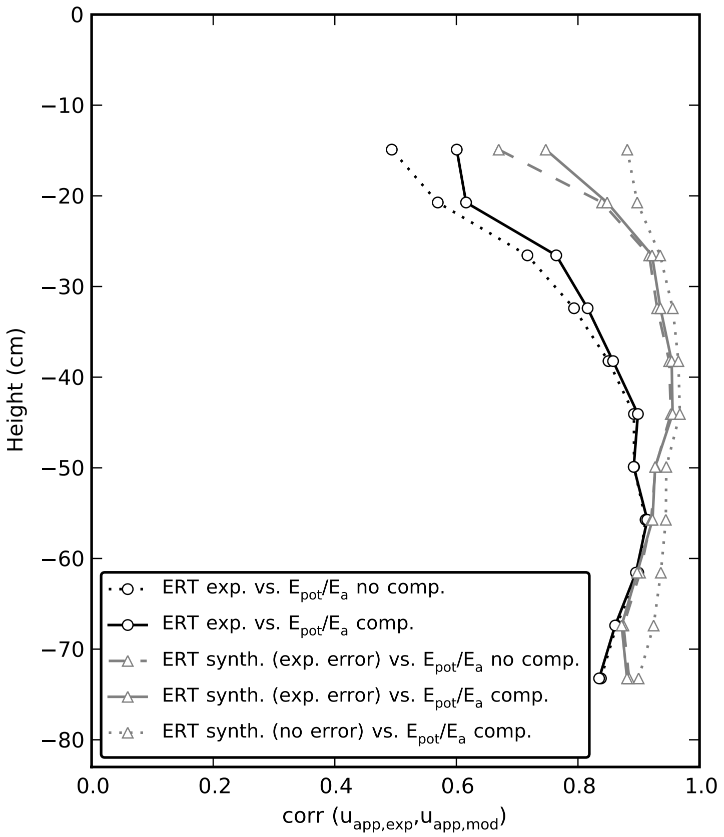

Figure 4.12: Correlation coefficient between experimental $u_{app,exp}$ and modeled apparent velocities $u_{app,mod}$ plotted over the height of the laboratory soil for different combinations of ERT-derived and modeled data.

experimental and modeled u_{app} that increase towards the top. This may be related to higher bulk electrical conductivity contrasts in the upper part so that smoothing errors are supposed to be highest.

As expected, error-free ERT data showed the best correlation. However, even with an error-free data set it was not possible to get a perfect correlation because the inversion smoothes out sharp contrasts and the apparent formation factors derived at $t = 0$ are thus spatially and temporally variable. The synthetic ERT data with experimental error additionally reduced the correlation with the modeled u_{app} for all heights, and especially close to the top surface. However the correlation loss between the simulated velocities and the velocities derived from the synthetic ERT data with realistic measurement errors was still smaller than the correlation loss between the simulated velocities and the velocities derived from the experimental ERT data. This indicates that the discrepancies between experiment and model cannot be solely explained by ERT error. Especially in the upper part, large parts of the remaining deviations must be explained by different error sources.

On the modeling side, the deviations can be caused by the insufficient description of processes induced by the evaporation conditions, namely energy and vapor fluxes that were not considered in the model. The exact reproduction of the total evaporation by the ‘E_{pot}/E_a compensation’ approach improved the model results. Fig. 4.12 shows the correlation coefficient between the experimental and the modeled u_{app} for all heights for the ‘E_{pot}/E_a compensation’ and the ‘E_{pot}/E_a no compensation’ approach. The ‘E_{pot}/E_a compensation’ approach performed better, especially in the upper part of the laboratory soil.

The comparison between the ‘E_{pot}/E_a no compensation’ model results and the inversion results of the synthetic ERT data generated with the ‘true’ model, ‘E_{pot}/E_a compensation’, suggested that the wrong boundary condition, which underestimates the total flux, has a measurable effect on the solute transport in the upper part of the porous medium. The synthetic data shows that the difference can be identified with ERT observations. However, we stress that the ‘E_{pot}/E_a compensation’ approach represents a crude approximation of the compensation that occurs in reality. The exact local enhancement of the potential evaporation rate is spatially variable and depends on the materials and evaporation rates in the neighboring cubes. In the ‘E_{pot}/E_a compensation’ approach we assumed a uniform compensation. A modeling approach that simulates liquid water, water vapor and heat fluxes within the soil, and the lateral exchange of mass, energy and momentum within the boundary layer might improve the correlation between experimental and modeled solute transport because of a more accurate representation of the upper boundary fluxes.

The error analysis showed that the improved upper boundary condition cannot reduce the correlation loss down to the ERT error level. This indicates that other errors and uncertainties in the simulations are responsible for this correlation loss. Besides the spatial evaporation pattern that is probably more complex than our approximation, the deviations can be further caused by errors in the hydraulic parameters of the three materials. In laboratory soil experiments, each material is characterized by a single parameter set. This parameter set is determined separately, e. g. using multi-step outflow experiments. Thus, deviations in the packing between the two setups as well as the variability between cubes of the same material may contribute to deviations between observed and modeled transport. Additionally, it is known that the mixing zone at the interface between two different materials has special pore space characteristics (Vasin et al., 2008) and probably influences the overall flow and transport considerably. These error sources could be partly addressed by fitting the hydraulic properties of the three materials ‘in situ’ using the ERT data in an integrated hydrogeophysical inversion approach, which will be evaluated in future studies.

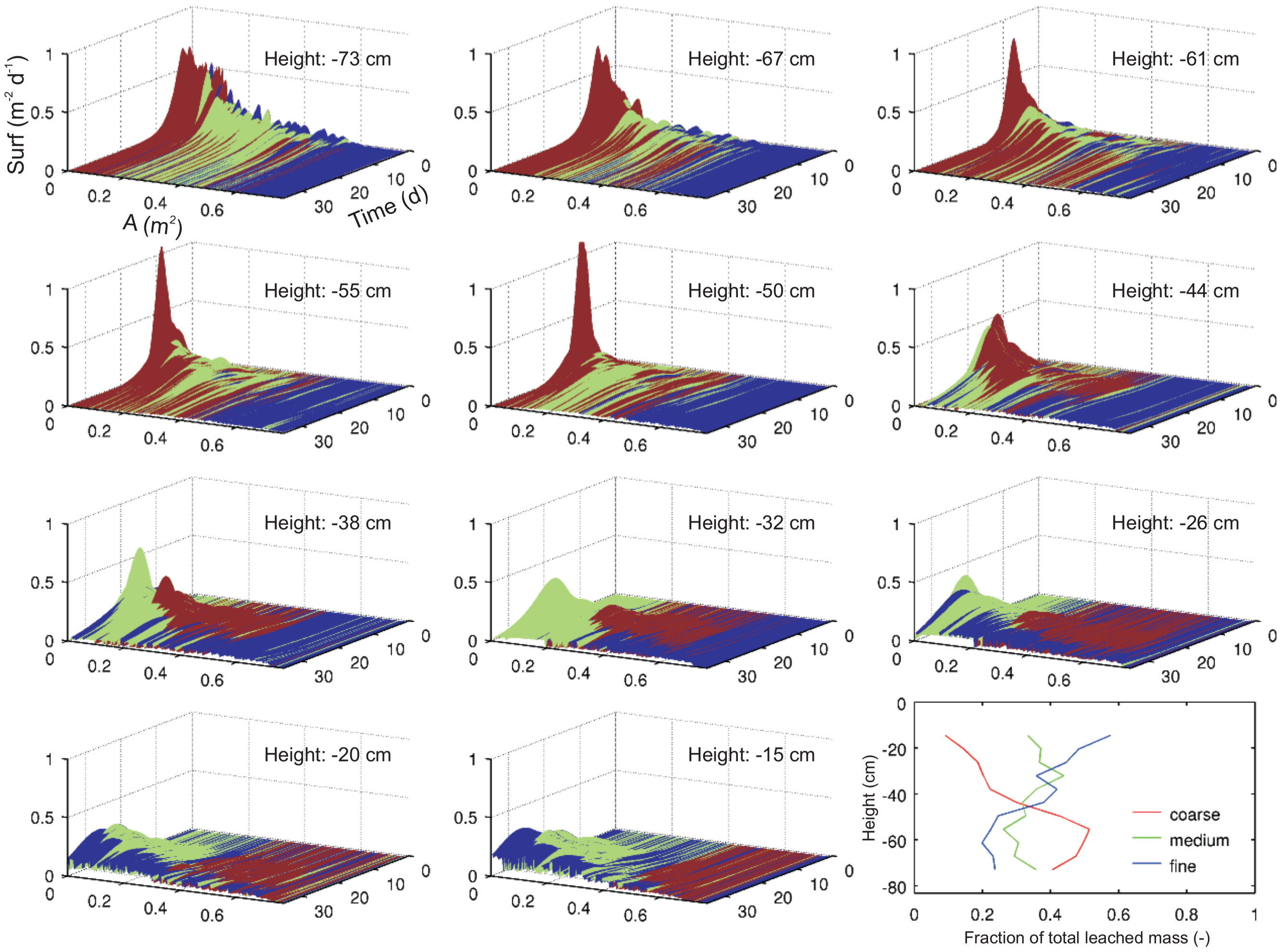

Figure 4.13: Leaching surfaces for different heights. The breakthrough curves are colored by the corresponding material (coarse: red, medium: green, fine: blue). Lower right: The fraction of the total leached mass for each material plotted over the height of the porous medium.

4.3.6 Preferential pathways of upward solute transport

For the analysis of the preferential pathways of upward solute transport, we generated leaching surfaces for 11 heights from -73 cm to -15 cm (Fig. 4.13). We omitted the heights of the two uppermost layers and the bottom layer because the fitting of the BTC yielded a coefficient of determination of $R^2 < 0.8$ for most of the cubes. In the upper layers, this was related to the solute accumulation close to the soil surface that led to an increase of the solute concentration before tracer arrived from below. The leaching surfaces were plotted as in de Rooij and Stagnitti (2002) except that we colored the BTC traces of the surface by the material-specific color. Thus, the surface directly indicates to which extent each material contributes to the overall transport.

The leaching surfaces show a clear trend from the bottom to the top of the porous medium. Close to the bottom (-73 cm and -67 cm) most of the solutes leached through the coarse material (Fig. 4.13), which can be explained by the high hydraulic conductivity of the coarse material close to saturation (Fig. 4.2). The leaching surfaces indicate that the complete fraction of coarse material contributed rather uniformly to the transport. This indicates high connectivity and continuous flow paths between the blocks of coarse material within the first three layers. These conditions changed from -61 to -50 cm. In these layers, parts of the coarse material became less important for the overall transport, whereas other parts of the coarse material seem to compensate the ‘isolated’ coarse fraction by an even higher solute flux. Fig. 4.13 shows that the resulting leaching surfaces are peakier. At -44 cm, the preferential transport pattern changes abruptly and shows that all materials are almost equally contributing to the overall transport. Above -44 cm the contribution of the coarse material continuously decreases, while the medium and fine materials start to dominate the transport. From -26 cm to -15 cm the leaching surfaces indicate that the fine material became the most important transport pathway. The observed trend of preferential transport from coarse over medium to fine material from the bottom to the top of the porous medium is consistent with the hydraulic functions of the three materials (Fig. 4.2).

4.4 Conclusions

This study corroborated the benefit of laboratory experiments in artificial porous media with known heterogeneity and performed under well-defined boundary conditions for studying the effect of heterogeneity on flow and transport, for fundamentally verifying numerical models and for evaluating the data quality of monitoring techniques. We presented results of the first upward tracer experiment in a complex heterogeneous laboratory soil under evaporation conditions. The detailed comparison of ERT-derived and modeled water electrical conductivities and fitted apparent velocities revealed discrepancies that increased from the bottom towards the surface of the laboratory soil. Synthetic ERT experiments demonstrated that this trend can be explained partly by ERT errors. However, large parts of the remaining deviations must be attributed to other error sources. The main conclusion of the detailed ERT analysis is that the accuracy of the ERT setup was high enough to analyze errors of the flow and transport model. This conclusion is, however, not directly transferable to undisturbed soils with unknown heterogeneity. During the ERT processing, we used the knowledge about the heterogeneity of the porous medium. First, we resolved the ambiguity of water content and pore water velocity changes by applying the water content distribution of the material-specific TDR data. Second, we applied structural constraints to the ERT inversion that were based on a priori knowledge about the porous medium. In natural soils these issues must be addressed differently, e. g. by the joint inversion of ERT and GPR data (Doetsch et al., 2010).

With respect to errors of the flow and transport model, we conclude that one major weakness of continuum theory models based on RE and ADE might be the commonly used classical potential/actual evaporation (E_{pot}/E_a) approach. Parts of the deviations between monitored and modeled solute transport was attributed to the erroneous representation of the upper boundary condition. The analysis of the experimental total and local evaporation rates indicated a higher total evaporation rate during the experiment than predicted by the E_{pot}/E_a approach. We showed that the actual evaporation locally exceeded the potential evaporation rate that was determined as maximum evaporation from a free water table. The E_{pot}/E_a approach did therefore underestimate the total evaporation. Introducing the partial compensation of low evaporation zones by increasing the potential evaporation rate uniformly led to a better correlation between monitored and modeled solute transport. We assume two processes to be responsible for this compensation. First, the local decrease of the evaporation rate from coarse-grained regions caused an ‘oasis effect’ that occurred here at smaller scale than usually discussed (e. g., Moriwaki and Kanda, 2004). Second, lateral heat fluxes from the hotter coarse material that was characterized by low, ‘stage-2’ evaporation rates, may have supplied additional energy for evaporation to the fine and medium material. Because both compensation mechanisms are scale-dependent, the efficiency of the compensation (here: 50 % of the evaporation deficit was compensated by wetter regions) probably decreases with increasing scale of the heterogeneity.

Regarding the difficulties in reproducing the upper boundary fluxes, simulation studies that neglect the compensation mechanisms during evaporation (Russo et al., 1998; Russo and Fiori, 2008; Kollet, 2009) must be interpreted carefully. Upscaling approaches that are based on the results of three-dimensional unsaturated flow and transport models under transient conditions with evaporation periods might be biased when the model does not account for lateral evaporative compensation mechanisms at the soil surface.

Based on the three-dimensional experimental observations we reconstructed the flow pathways by using leaching surfaces. The main conclusion of this analysis is that even under the low upward flow velocities during evaporation, upward solute transport was not uniform but showed a systematic pattern of preferential transport pathways. The experiment demonstrated that the locations of preferential upward transport pathways depended on the height above the water table. Close to the water table preferential transport mainly took place in the coarse material, while with increasing height transport was more localized in the finer materials.

The observed strong dependency of water table height on preferential upward transport pathways suggests that upward transport patterns may drastically change when water table falls or rises, showing the ceasing of old and opening of new pathways. Thus, regarding natural soils and boundary conditions, groundwater table fluctuations may not only play an important role in whether upward flow occurs or not, but are also the key process in the activation of preferential upward flow pathways.

Chapter 5

Synthesis

5.1 Summarizing conclusions

This thesis deals with the analysis of solute transport in unsaturated heterogeneous porous media under evaporation conditions. Despite the significance of upward transport for groundwater quality management and sustainable agricultural practice, there are only few studies published that focus on the effect of soil heterogeneity on upward flow and transport. Therefore, laboratory tracer experiments were conducted in artificial porous media with known heterogeneity and under defined boundary conditions, in order (1) to analyze fundamental upward flow and transport processes, (2) to evaluate the potential of non-invasive, three-dimensional geophysical techniques for monitoring these processes, and (3) to verify the predictive power of commonly-applied continuum theory of liquid flow and solute transport in unsaturated porous media.

High concentration gradients due to solute accumulation at the soil surface during evaporation pose very high demands on numerical solution schemes. By using Hydrus-2D/3D (e. g., Simunek et al., 2008) or the parallelized version PARSWMS of the original source code SWMS_3D (Simunek et al., 1995; Hardelauf et al., 2007), it was not possible to avoid oscillations in the numerical solution of the solute transport equation that occurred with ongoing solute accumulation. The fact that these fundamental numerical problems appeared during the application of these widely-used flow and transport codes reflects that upward transport in heterogeneous porous media has barely been investigated in the past. The stability of transport simulations based on RWPT is not negatively affected by high concentration gradients. There is however an on-going debate (e. g., Salamon et al., 2006) on the treatment of dispersive displacements across discontinuities of the dispersion tensor or water content in RWPT codes. These discontinuities occur either naturally (e. g., soil horizons) or numerically at every element interface of finite difference or finite volume schemes. In this thesis, a new RWPT algorithm has been presented that accurately handles these interfaces in an efficient manner. The application of the new algorithm to different transport problems (Haber-Pohlmeier et al., 2010; Bechtold et al., 2011a;

Bechtold et al., 2011b; Bechtold et al., 2011c) proved its robustness and general applicability to vadose zone studies, in particular in the presence of high concentration gradients at the soil surface.

This thesis corroborated the unique value of tracer experiments in artificial heterogeneous porous media to fundamentally study flow and transport processes. Tracer experiments were performed in a simple composite porous medium and a complex laboratory soil under evaporation conditions. For the simple composite porous medium, the close link between experiment and model proved the process of near-surface solute redistribution based on real observations and numerical simulations. Because the initial distribution of solute mass in a heterogeneous flow field has an important impact on the leaching rate (Vanderborght et al., 1998; Demmy et al., 1999), the formation of high solute concentration spots at the soil surface due to near-surface solute redistribution may have broad implications on effective one-dimensional solute fluxes. The upward flow tracer experiment in the more complex laboratory soil can be considered as a benchmark for RE and ADE that describe flow and transport at this scale. The experiment showed a transition of preferential upward transport pathways over the height of the laboratory soil that is mainly consistent with simulated data. The fact that the observed principal redistribution processes and preferential upward transport pathways were reproduced by numerical simulations, based on RE and ADE, supports their application to numerically investigate the effect of soil heterogeneity on solute transport and to derive upscaling concepts. However, the strong simplification of the upper boundary by the classic E_{pot}/E_a approach must be considered as one of the weakest points of numerical flow and transport studies that include evaporation periods. Laboratory experiments demonstrated that evaporation patterns at heterogeneous soil surfaces are complex and a result of locally-decreasing osmotic potential and salt crystallization (Bechtold et al., 2011a; Bechtold et al., 2011c; Nachshon et al., 2011), lateral compensation mechanisms that enhance the actual evaporation locally when evaporation drops in surrounding regions (Bechtold et al., 2011c), and the distribution of soil moisture at the micro scale (Or et al., 2011). An adequate prediction of evaporation patterns at a heterogeneous soil surface is essential for the prediction of solute fluxes below and at the soil surface.

Finally, this thesis demonstrates that non-invasive monitoring techniques are very useful to obtain detailed spatial and temporal information about upward transport. However, it must be stated that MRI and ERT had difficulties to capture the strong solute accumulation at the soil surface during evaporation. Further, in case of ERT, the knowledge about the soil structure was used to disentangle spatial variations in soil moisture and pore water electrical conductivity from observed distributions of the bulk soil electrical conductivity. For experiments with natural soils, in which soil heterogeneity is largely unknown, the joint use of ERT with ground-penetrating radar (GPR) to constrain water content changes is promising (Doetsch et al., 2010).

5.2 Perspectives

5.2.1 Random walk particle tracking in vadose zone studies

As already stated in the review of Delay et al. (2005), RWPT has been rarely used for unsaturated media although the concept is best suited to handle the high spatial and temporal variability of the velocity and water content distribution. The new RWPT algorithm and its applications presented in this thesis could encourage the use and further development of RWPT in future vadose zone studies. Two possible applications are mentioned here. Firstly, the basic idea of the reflection barrier concept is also applicable to reactive transport problems because Eq. 2.5 can also account for abrupt changes of the retardation coefficient. This should be verified in adequate test scenarios. Secondly, the oscillations encountered when using Hydrus-2D/3D or PARSWMS in the presence of high concentration gradients at the soil surface were also reported independently from modeling work with R-SWMS, a three-dimensional coupled flow and transport model for soil and roots, in which solute accumulation occurred around plant roots (Javaux et al., 2008, Natalie Schröder, personal communication 2010). Using the flow velocity field from R-SWMS as input for RWPT simulations using PARTRACE (Bechtold et al., 2011b) provided accurate solutions of the transport problem that could not be obtained by R-SWMS (Schröder et al., 2011).

5.2.2 The effect of upward flow periods on the leaching of solutes

Besides the quasi-steady-steady upward flow tracer experiment presented in Chapter 4, further tracer experiments have been conducted in the complex laboratory soil. These are

- a drying sequence started at the end of the quasi-steady-state tracer experiment (90 days),
- a leaching sequence under transient conditions started at the end of the drying sequence (60 days),
- a pulse tracer application at the soil surface under steady-state downward flow conditions,
- an experiment in which no tracer was applied, but a salinization process occurred under net downward flow conditions due to the combined effect of alternating irrigation and evaporation conditions and soil heterogeneity.

The evaluation of these experiments may further contribute to the understanding of how upward flow periods affect the leaching of solutes. Preliminary numerical flow and transport experiments indicated that depending on the timing and duration of infiltration and evaporation periods, the different solute redistribution processes have either accelerating or retarding effects (Bechtold et al., 2009). The comparison with the experimental data is again essential to prove this finding.

5.2.3 From laboratory soils to natural soils

In this thesis, upward transport has been only analyzed in artificial heterogeneous porous media. Similar tracer experiments should be performed in natural soils. For example, a uniform application of a dye tracer like BB to the soil surface of a natural soil under steady-state upward flow conditions from a constant water table may provide interesting patterns of BB at the soil surface that will strongly depend on the inherent soil heterogeneity. From the quasi-steady-state upward flow tracer experiment the question arises whether preferential upward transport from a constant water table similarly occurs in natural soils. The success of the latter experiment will strongly depend on the resolution and accuracy of the data obtained from the geophysical monitoring technique.

5.2.4 Effective parameter models that account for redistribution processes during upward flow

The modeling studies in this thesis were focused on the fully-deterministic three-dimensional simulation of the observed flow and transport. The ultimate goal however must be to transfer the knowledge about the small-scale processes to larger scales. Future research should investigate the potential and limitations of existing effective parameter models (e. g., Gerke, 2006) to reproduce the effects of solute redistribution during upward flow periods on the leaching rate. Because solutes are transported upwards in the coarse and fine regions during evaporation, the effective parameter model should have at least two permeable regions, such as the dual-permeability model proposed by Gerke and van Genuchten (1993). In this concept, solute mass transfer between the two domains is governed by advective and dispersive transport. The advective exchange that is driven by the pressure head difference between the two domains could principally describe the lateral solute redistribution deeper in the soil, as well as the near-surface solute redistribution.

References

Abu-Zreig et al., 2006 Abu-Zreig, M.M., Y. Abe, and H. Isoda. 2006. Study of salt removal with evaporation drainage method. Can. Biosyst. Eng. 48:A25-A30.

Ackerer and Mose, 2000 Ackerer, P., and R. Mose. 2000. Comment on "Diffusion theory for transport in porous media: transition-probability densities of diffusion processes corresponding to advection-dispersion equations" by Eric M. LaBolle et al. Water Resour. Res. 36:819-821.

Ahlstrom et al., 1977 Ahlstrom, S.W., H.P. Foote, R.C. Arnett, C.R. Cole, and R.J. Serne. 1977. Multi-component mass transport model: theory and numerical implementation. Rep. BNWL-2127. Battelle Pacific Northwest Lab., Richland, Washington.

Aris, 1956 Aris, R. 1956. On the dispersion of a solute in a fluid flowing through a tube. Proc. Roy. Soc. Lond. A 235:67-77.

Ball, 2002 Ball, J.A.R. 2002. Characteristic impedance of unbalanced TDR probes. IEEE Trans. Instr. Meas. 51:532-536.

Bear, 1972 Bear, J. 1972. Dynamics of fluids in porous media. American Elsevier Publishing Company, New York.

Bechtold et al., 2009 Bechtold, M., J. Vanderborght, M. Herbst, L. Weihermüller, R. Kasteel, and H. Vereecken. 2009. Lateral water redistribution during evaporative-driven upward flow and its effect on solute transport. Geophysical Research Abstracts, Vol. 11, EGU General Assembly, 19-24 April 2009, Vienna, Austria.

Bechtold et al., 2010 Bechtold, M., J.A. Huisman, L. Weihermüller, and H. Vereecken. 2010. Accurate determination of the bulk electrical conductivity with the TDR100 cable tester. Soil Sci. Soc. Am. J. 74:495-501.

Bechtold et al., 2011a Bechtold, M., S. Haber-Pohlmeier, J. Vanderborght, A. Pohlmeier, P.A. Ferre, and H. Vereecken. 2011a. Near-surface solute redistribution during evaporation. Geophys. Res. Lett., 38, L17404.

Bechtold et al., 2011b Bechtold, M., J. Vanderborght, O. Ippisch, and H. Vereecken. 2011b. Efficient random walk particle tracking algorithm for advective dispersive transport in media with discontinuous dispersion coefficients and water contents. Accepted for publ. in Water Resour. Res., 2010WR010267.

Bechtold et al., 2011c Bechtold, M., J. Vanderborght, L. Weihermüller, M. Herbst, T. Gunther, O. Ippisch, R. Kasteel, and H. Vereecken. 2011c. Upward transport in a 3-D heterogeneous laboratory soil under evaporation conditions. Submitted to Vadose Zone J. V11-0066.

Binley et al., 1995 Binley, A., A. Ramirez, and W. Daily. 1995. Regularised image reconstruction of noisy electrical resistivity tomography data. in 4th Workshop of the European Concerted Action on Process Tomography, European Concerted Action on Process Tomography, Bergen.

Binley et al., 1996 Binley, A., S. HenryPoulter, and B. Shaw. 1996. Examination of solute transport in an undisturbed soil column using electrical resistance tomography. Water Resour. Res. 32:763-769.

Binley et al., 2010 Binley, A., G. Cassiani, and R. Deiana. 2010. Hydrogeophysics: opportunities and challenges. Boll. Geofis. Teor. Appl. 51:267-284.

Bloem et al., 2008 Bloem, E., J. Vanderborght, and G.H. de Rooij. 2008. Leaching surfaces to characterize transport in a heterogeneous aquifer: comparison between flux concentrations, resident concentrations, and flux concentrations estimated from temporal moment analysis. Water Resour. Res. 44.

Blonquist et al., 2005 Blonquist, J.M., S.B. Jones, and D.A. Robinson. 2005. Standardizing characterization of electromagnetic water content sensors: Part 2. Evaluation of seven sensing systems. Vadose Zone J. 4:1059-1069.

Brezzi and Fortin, 1991 Brezzi, F., and M. Fortin. 1991. Mixed and hybrid finite element methods. Springer.

Campbell Scientific Inc., 2007 Campbell Scientific Inc. 2007. TDR100 Time Domain Reflectometry - User's Guide, pp. 48.

Carminati and Flühler, 2009 Carminati, A., and H. Flühler. 2009. Water infiltration and redistribution in soil aggregate packings. Vadose Zone J. 8:150-157.

Castiglione and Shouse, 2003 Castiglione, P., and P.J. Shouse. 2003. The effect of ohmic, cable losses on time-domain reflectometry measurements of electrical conductivity. Soil Sci. Soc. Am. J. 67:414-424.

Cataldo et al., 2008 Cataldo, A., L. Tarricone, F. Attivissimo, and A. Trotta. 2008. Simultaneous measurement of dielectric properties and levels of liquids using a TDR method. Measurement 41:307-319.

Coquet et al., 2005 Coquet, Y., J. Simunek, C. Coutadeur, M.T. van Genuchten, V. Pot, and J. Roger-Estrade. 2005. Water and solute transport in a cultivated silt loam soil: 2. Numerical analysis. Vadose Zone J. 4:587-601.

Cordes et al., 1991 Cordes, C., H. Daniels, and G. Rouvé. 1991. A new very efficient algorithm for particle tracking in layered aquifers. In: Sari, D.B., et al. (Eds.), Computer Methods in Water Resources II, vol. 1, Groundwater Modelling and Pressure Flow. Springer Verlag, New York, 41-55.

Council, 1991 Council, N.R. 1991. Opportunities in the hydrologic sciences. National Academy Press: Washington.

de Rooij and Stagnitti, 2002 de Rooij, G.H., and F. Stagnitti. 2002. Spatial and temporal distribution of solute leaching in heterogeneous soils: analysis and application to multisampler lysimeter data. J. Contam. Hydrol. 54:329-346.

Delay et al., 2005 Delay, F., P. Ackerer, and C. Danquigny. 2005. Simulating solute transport in porous or fractured formations using random walk particle tracking: A review. Vadose Zone J. 4:360-379.

Demmy et al., 1999 Demmy, G., S. Berglund, and W. Graham. 1999. Injection mode implications for solute transport in porous media: Analysis in a stochastic Lagrangian framework. Water Resour. Res. 35:1965-1973.

Deutsch and Journel, 1998 Deutsch, C.V., and A.G. Journel. 1998. GSLIB: geostatistical software library and user's guide. 2nd ed. Oxford University Press, New York.

Doetsch et al., 2010 Doetsch, J., N. Linde, and A. Binley. 2010. Structural joint inversion of time-lapse crosshole ERT and GPR traveltime data. Geophys. Res. Lett. 37, L24404.

Evett et al., 2005 Evett, S.R., J.A. Tolk, and T.A. Howell. 2005. Time domain reflectometry laboratory calibration in travel time, bulk electrical conductivity, and effective frequency. Vadose Zone J. 4:1020-1029.

FAO, 2000 FAO. 2000. Land resource potential and constraints at regional and country levels. . World Soil Resources Reports 90, Rome, Italy: FAO, Land and Water Development Division.

Fernandez-Garcia et al., 2005 Fernandez-Garcia, D., T.H. Illangasekare, and H. Rajaram. 2005. Differences in the scale-dependence of dispersivity estimated from temporal and spatial moments in chemically and physically heterogeneous porous media. Adv. Water Resour. 28:745-759.

Feyen et al., 1998 Feyen, J., D. Jacques, A. Timmerman, and J. Vanderborght. 1998. Modelling water flow and solute transport in heterogeneous soils: A review of recent approaches. J. agric. eng. res. 70:231-256.

Flint et al., 2002 Flint, A.L., G.S. Campbell, K.M. Ellett, and C. Calissendorff. 2002. Calibration and temperature correction of heat dissipation matric potential sensors. Soil Sci. Soc. Am. J. 66:1439-1445.

Fujimaki et al., 2006 Fujimaki, H., T. Shimano, M. Inoue, and K. Nakane. 2006. Effect of a salt crust on evaporation from a bare saline soil. Vadose Zone J. 5:1246-1256.

Garré et al., 2010 Garré, S., J. Koestel, T. Gunther, M. Javaux, J. Vanderborght, and H. Vereecken. 2010. Comparison of heterogeneous transport processes observed with electrical resistivity tomography in two soils. Vadose Zone J. 9:336-349.

Gerke, 2006 Gerke, H.H. 2006. Preferential flow descriptions for structured soils. J. plant nutr. soil sci. 169:382-400.

Gerke and van Genuchten, 1993 Gerke, H.H., and M.T. van Genuchten. 1993. Evaluation of a 1st-order water transfer term for variably saturated dual-porosity flow models. Water Resour. Res. 29:1225-1238.

Giese and Tiemann, 1975 Giese, K., and R. Tiemann. 1975. Determination of complex permittivity from thin-sample time domain reflectometry improved analysis of step response waveform. Adv. Mol. Relax. Processes 7:45-59.

Greiner et al., 1997 Greiner, A., W. Schreiber, G. Brix, and W. Kinzelbach. 1997. Magnetic resonance imaging of paramagnetic tracers in porous media: Quantification of flow and transport parameters. Water Resour. Res. 33:1461-1473.

Günther et al., 2006 Günther, T., C. Rucker, and K. Spitzer. 2006. Three-dimensional modelling and inversion of dc resistivity data incorporating topography - II. Inversion. Geophys. J. Int. 166:506-517.

Haber-Pohlmeier et al., 2010 Haber-Pohlmeier, S., M. Bechtold, S. Stapf, and A. Pohlmeier. 2010. Water flow monitored by tracer transport in natural porous media using magnetic resonance imaging. Vadose Zone J. 9:835-845.

Hardelauf et al., 2007 Hardelauf, H., M. Javaux, M. Herbst, S. Gottschalk, R. Kasteel, J. Vanderborght, and H. Vereecken. 2007. PARSWMS: a parallelized model for simulating three-dimensional water flow and solute transport in variably saturated soils. Vadose Zone J. 6:255-259.

Harter and Hopmans, 2004 Harter, T., and J.W. Hopmans. 2004. Role of vadose-zone flow processes in regional-scale hydrology: review, opportunities and challenges. Unsaturated-Zone Modeling: Progress, Challenges and Applications 6:179-208.

Heimovaara et al., 1995 Heimovaara, T.J., A.G. Focke, W. Bouten, and J.M. Verstraten. 1995. Assessing temporal variations in soil-water composition with time-domain reflectometry. Soil Sci. Soc. Am. J. 59:689-698.

Herbst et al., 2005 Herbst, M., W. Fialkiewicz, T. Chen, T. Putz, D. Thiery, C. Mouvet, G. Vachaud, and H. Vereecken. 2005. Intercomparison of flow and transport models applied to vertical drainage in cropped lysimeters. Vadose Zone J. 4:240-254.

Hofstee et al., 1998 Hofstee, C., M. Oostrom, J.H. Dane, and R.C. Walker. 1998. Infiltration and redistribution of perchloroethylene in partially saturated, stratified porous media. J. Contam. Hydrol. 34:293-313.

Hoteit et al., 2002 Hoteit, H., R. Mose, A. Younes, F. Lehmann, and P. Ackerer. 2002. Three-dimensional modeling of mass transfer in porous media using the mixed hybrid finite elements and the random-walk methods. Math. Geol. 34:435-456.

Huisman and Bouten, 1999 Huisman, J.A., and W. Bouten. 1999. Comparison of calibration and direct measurement of cable and probe properties in time domain reflectometry. Soil Sci. Soc. Am. J. 63:1615-1617.

Huisman and Vereecken, 2006 Huisman, J.A., and H. Vereecken. 2006. Comments on "Time domain reflectometry laboratory calibration in travel time, bulk electrical conductivity, and effective frequency". Vadose Zone J. 5:1071-1072.

Huisman et al., 2008 Huisman, J.A., C.P. Lin, L. Weihermüller, and H. Vereecken. 2008. Accuracy of bulk electrical conductivity measurements with time domain reflectometry. Vadose Zone J. 7:426-433.

Illangasekare et al., 1995 Illangasekare, T.H., J.L. Ramsey, K.H. Jensen, and M.B. Butts. 1995. Experimental-study of movement and distribution of dense organic contaminants in heterogeneous aquifers. J. Contam. Hydrol. 20:1-25.

Ippisch et al., 2006 Ippisch, O., H.J. Vogel, and P. Bastian. 2006. Validity limits for the van Genuchten-Mualem model and implications for parameter estimation and numerical simulation. Adv. Water Resour. 29:1780-1789.

Javaux et al., 2006 Javaux, M., J. Vanderborght, R. Kasteel, and M. Vanclooster. 2006. Three-dimensional modeling of the scale- and flow rate-dependency of dispersion in a heterogeneous unsaturated sandy monolith. Vadose Zone J. 5:515-528.

Javaux et al., 2008 Javaux, M., T. Schroder, J. Vanderborght, and H. Vereecken. 2008. Use of a three-dimensional detailed modeling approach for predicting root water uptake. Vadose Zone J. 7:1079-1088.

Jensen et al., 1990 Jensen, M.E., R.D. Burman, and R.G. Allen. 1990. Evapotranspiration and irrigation water requirements. ASCE manuals and reports on engineering practice No. 70, ASCE.

Jury et al., 1990 Jury, W.A., D. Russo, G. Streile, and H. Elabd. 1990. Evaluation of volatilization by organic-chemicals residing below the soil surface. Water Resour. Res. 26:13-20.

Kasteel et al., 2000 Kasteel, R., H.J. Vogel, and K. Roth. 2000. From local hydraulic properties to effective transport in soil. Eur. J. Soil Sci. 51:81-91.

Kasteel et al., 2002 Kasteel, R., H.J. Vogel, and K. Roth. 2002. Effect of non-linear adsorption on the transport behaviour of Brilliant Blue in a field soil. Eur. J. Soil Sci. 53:231-240.

Kasteel et al., 2007 Kasteel, R., T. Putz, and H. Vereecken. 2007. An experimental and numerical study on flow and transport in a field soil using zero-tension lysimeters and suction plates. Eur. J. Soil Sci. 58:632-645.

Kemna et al., 2002 Kemna, A., J. Vanderborght, B. Kulessa, and H. Vereecken. 2002. Imaging and characterisation of subsurface solute transport using electrical resistivity tomography (ERT) and equivalent transport models. J. Hydrol. 267:125-146.

Kinzelbach and Uffink, 1991 Kinzelbach, W. and G. Uffink. 1991. The random walk method and extensions in groundwater modelling. In Transport Processes Porous Med. edited by J. Bear and M. Y. Corapcioglu, pp. 761-787, Kluwer Academic, Hingham, MA.

Koestel et al., 2008 Koestel, J., A. Kemna, M. Javaux, A. Binley, and H. Vereecken. 2008. Quantitative imaging of solute transport in an unsaturated and undisturbed soil monolith with 3-D ERT and TDR. Water Resour. Res. 44.

Kollet, 2009 Kollet, S.J. 2009. Influence of soil heterogeneity on evapotranspiration under shallow water table conditions: transient, stochastic simulations. Environ. Res. Lett. 4.

Kowalsky et al., 2004 Kowalsky, M.B., S. Finsterle, and Y. Rubin. 2004. Estimating flow parameter distributions using ground-penetrating radar and hydrological measurements during transient flow in the vadose zone. Adv. Water Resour. 27:583-599.

LaBolle et al., 1996 LaBolle, E.M., G.E. Fogg, and A.F.B. Tompson. 1996. Random-walk simulation of transport in heterogeneous porous media: local mass-conservation problem and implementation methods. Water Resour. Res. 32:583-593.

LaBolle et al., 1998 LaBolle, E.M., J. Quastel, and G.E. Fogg. 1998. Diffusion theory for transport in porous media: transition-probability densities of diffusion processes corresponding to advection-dispersion equations. Water Resour. Res. 34:1685-1693.

LaBolle et al., 2000 LaBolle, E.M., J. Quastel, G.E. Fogg, and J. Gravner. 2000. Diffusion processes in composite porous media and their numerical integration by random walks: Generalized stochastic differential equations with discontinuous coefficients. Water Resour. Res. 36:651-662.

LaBrecque et al., 1996 LaBrecque, D.J., M. Miletto, W. Daily, A. Ramirez, and E. Owen. 1996. The effects of noise on Occam's inversion of resistivity tomography data. Geophysics 61:538-548.

Lamy et al., 2009 Lamy, E., L. Lassabatere, B. Bechet, and H. Andrieu. 2009. Modeling the influence of an artificial macropore in sandy columns on flow and solute transfer. J. Hydrol. 376:392-402.

Lehmann and Or, 2009 Lehmann, P., and D. Or. 2009. Evaporation and capillary coupling across vertical textural contrasts in porous media. Physical Review E 80.

Lichtner et al., 2002 Lichtner, P.C., S. Kelkar, and B. Robinson. 2002. New form of dispersion tensor for axisymmetric porous media with implementation in particle tracking. Water Resour. Res. 38.

Lim, 2006 Lim, D.H. 2006. Numerical study of nuclide migration in a nonuniform horizontal flow field of a high-level radioactive waste repository with multiple canisters. Nucl. Technol. 156:222-245.

Lin et al., 2007 Lin, C.P., C.C. Chung, and S.H. Tang. 2007. Accurate time domain reflectometry measurement of electrical conductivity accounting for cable resistance and recording time. Soil Sci. Soc. Am. J. 71:1278-1287.

Lin et al., 2008 Lin, C.P., C.C. Chung, J.A. Huisman, and S.H. Tang. 2008. Clarification and calibration of reflection coefficient for electrical conductivity measurement by time domain reflectometry. Soil Sci. Soc. Am. J. 72:1033-1040.

Looms et al., 2008 Looms, M.C., K.H. Jensen, A. Binley, and L. Nielsen. 2008. Monitoring unsaturated flow and transport using cross-borehole geophysical methods. Vadose Zone J. 7:227-237.

Lundmark and Jansson, 2008 Lundmark, A., and P.E. Jansson. 2008. Estimating the fate of de-icing salt in a roadside environment by combining modelling and field observations. Water Air Soil Pollut. 195:215-232.

Mallants et al., 1996 Mallants, D., M. Vanclooster, N. Toride, J. Vanderborght, M.T. vanGenuchten, and J. Feyen. 1996. Comparison of three methods to calibrate TDR for monitoring solute movement in undisturbed soil. Soil Sci. Soc. Am. J. 60:747-754.

Marle et al., 1967 Marle, C., Simandou.P, and C. Gaulier. 1967. Etude du déplacement de fluids miscibles en milieu poreux stratifié. Revue De L Institut Francais Du Petrole Et Annales Des Combustibles Liquides 22:272-294.

Maxwell and Kollet, 2008 Maxwell, R.M., and S.J. Kollet. 2008. Interdependence of groundwater dynamics and land-energy feedbacks under climate change. Nat. Geosci. 1:665-669.

Maxwell et al., 2007 Maxwell, R.M., C. Welty, and R.W. Harvey. 2007. Revisiting the cape cod bacteria injection experiment using a stochastic modeling approach. Environ. sci. technol. 41:5548-5558.

Maxwell et al., 2009 Maxwell, R. M. A. F. B. Tompson, and S. Kollet. 2009. A serendipitous, long-term infiltration experiment: Water and tritium circulation beneath the CAMBRIC trench at the Nevada Test Site. J. Contam. Hydrol. 108(1-2):12-28.

Millington and Quirk, 1961 Millington, R., and J.P. Quirk. 1961. Permeability of porous solids. Trans. Faraday Society 57.

Miller and Miller, 1956 Miller, E.E., and R.D. Miller. 1956. Physical Theory for Capillary Flow Phenomena. Journal of Applied Physics 27(4):324-332.

Mohamed et al., 2000 Mohamed, A.A., T. Sasaki, and K. Watanabe. 2000. Solute transport through unsaturated soil due to evaporation. J. Environ. Eng.-Asce 126:842-848.

Mohammadi and Vanclooster, 2011 Mohammadi, M.H., and M. Vanclooster. 2011. Analysis of flow rate dependency of solute transport in an undisturbed inceptisol. Vadose Zone J. 10:394-402.

Monego et al., 2010 Monego, M., G. Cassiani, R. Deiana, M. Putti, G. Passadore, and L. Altissimo. 2010. A tracer test in a shallow heterogeneous aquifer monitored via time-lapse surface electrical resistivity tomography. Geophysics 75:Wa61-Wa73.

Moriwaki and Kanda, 2004 Moriwaki, R., and M. Kanda. 2004. Seasonal and diurnal fluxes of radiation, heat, water vapor, and carbon dioxide over a suburban area. J. Appl. Meteorol. 43.

Nachshon et al., 2011 Nachshon, U., N. Weisbrod, M.I. Dragila, and A. Grader. 2011. Combined evaporation and salt precipitation in homogeneous and heterogeneous porous media. Water Resour. Res. 47.

Nambi and Powers, 2000 Nambi, I.M., and S.E. Powers. 2000. NAPL dissolution in heterogeneous systems: an experimental investigation in a simple heterogeneous system. J. Contam. Hydrol. 44:161-184.

Nassar and Horton, 1999 Nassar, I.N., and R. Horton. 1999. Salinity and compaction effects on soil water evaporation and water and solute distributions. Soil Sci. Soc. Am. J. 63:752-758.

Nelder and Mead, 1965 Nelder, J.A., and R. Mead. 1965. A simplex-method for function minimization. Comput. J. 7:308-313.

Neuendorf, 1997 Neuendorf, O. 1997. Numerische 3D-Simulation des Stofftransports in einem heteorgenen Aquifer. Res. Center Juelich Publ., Juelich, Germany.

Neuweiler and Vogel, 2007 Neuweiler, I., and H.J. Vogel. 2007. Upscaling for unsaturated flow for non-Gaussian heterogeneous porous media. Water Resour. Res. 43.

Nowak et al., 2010 Nowak, W., F.P.J. de Barros, and Y. Rubin. 2010. Bayesian geostatistical design: task-driven optimal site investigation when the geostatistical model is uncertain. Water Resour. Res. 46.

Oberdörster et al., 2010 Oberdörster, C., J. Vanderborght, A. Kemna, and H. Vereecken. 2010. Investigating preferential flow processes in a forest soil using time domain reflectometry and electrical resistivity tomography. Vadose Zone J. 9:350-361.

Oldenborger et al., 2005 Oldenborger, G.A., P.S. Routh, and M.D. Knoll. 2005. Sensitivity of electrical resistivity tomography data to electrode position errors. Geophys. J. Int. 163:1-9.

Or et al., 2011 Or, D., E. Shahraeeni, N. Shokri, and P. Lehmann. 2011. Interfacial processes controlling evaporation rates from porous media. Geophysical Research Abstracts, Vol. 13, EGU General Assembly, 3-7 April 2011, Vienna, Austria.

Osuga and Han, 2004 Osuga, T., and S. Han. 2004. Proton magnetic resonance imaging of diffusion of high- and low molecular-weight contrast agents in opaque porous media saturated with water. Magn. Reson. Imaging 22:1039-1042.

Ozturk and Ozkan, 2004 Ozturk, H.S., and I. Ozkan. 2004. Effects of evaporation and different flow regimes on solute distribution in soil. Transport Porous Med. 56:245-255.

Park et al., 2008 Park, C.H., C. Beyer, S. Bauer, and O. Kolditz. 2008. A study of preferential flow in heterogeneous media using random walk particle tracking. Geosciences J. 12:285-297.

Philip and de Vries, 1957 Philip, J.R., and D.A. de Vries. 1957. Moisture movement in porous materials under temperature gradients. Trans. Am. Geophys. Union 38:222-232.

Pollock, 1988 Pollock, D.W. 1988. Semianalytical computation of path lines for finite-difference models. Ground Water 26:743-750.

Prickett et al., 1981 Prickett, T.A., T.G. Naymik, and C.G. Longquist. 1981. A random walk solute transport model for selected groundwater quality evaluations. Illinois State Water Surv. Bulletin, 65, Champain, IL.

Ramirez et al., 2008 Ramirez, J.M., E.A. Thomann, E.C. Waymire, J. Chastanet, and B.D. Wood. 2008. A note on the theoretical foundations of particle tracking methods in heterogeneous porous media. Water Resour. Res. 44.

Raviart and Thomas, 1975 Raviart, P.A., and J.M. Thomas. 1975. A mixed finite element method for 2-nd order elliptic problems. Springer.

Reece, 1998 Reece, C.F. 1998. Simple method for determining cable length resistance in time domain reflectometry systems. Soil Sci. Soc. Am. J. 62:314-317.

Richards, 1931 Richards, L.A. 1931. Capillary conduction of liquids through porous mediums. Physics 1:318-333.

Ritter et al., 2005 Ritter, A., R. Munoz-Carpena, C.M. Regalado, M. Javaux, and M. Vanclooster. 2005. Using TDR and inverse modeling to characterize solute transport in a layered agricultural volcanic soil. Vadose Zone J. 4:300-309.

Robinson et al., 2003 Robinson, D.A., S.B. Jones, J.M. Wraith, D. Or, and S.P. Friedman. 2003. A review of advances in dielectric and electrical conductivity measurement in soils using time domain reflectometry. Vadose Zone J. 2:444-475.

Rossi et al., 2008 Rossi, M., O. Ippisch, and H. Flühler. 2008. Solute dilution under imbibition and drainage conditions in a heterogeneous structure: modeling of a sand tank experiment. Adv. Water Resour. 31:1242-1252.

Roth, 1995 Roth, K. 1995. Steady-state flow in an unsaturated, 2-dimensional, macroscopically homogeneous, Miller-similar medium. Water Resour. Res. 31:2127-2140.

Rücker and Günther, 2011 Rücker, C., and T. Günther. 2011. The simulation of finite ERT electrodes using the complete electrode model. Geophysis, in press.

Rücker et al., 2006 Rücker, C., T. Günther, and K. Spitzer. 2006. Three-dimensional modelling and inversion of dc resistivity data incorporating topography - I. Modelling. Geophys. J. Int. 166:495-505.

Russo and Bouton, 1992 Russo, D., and M. Bouton. 1992. Statistical-analysis of spatial variability in unsaturated flow parameters. Water Resour. Res. 28:1911-1925.

Russo and Fiori, 2008 Russo, D., and A. Fiori. 2008. Equivalent vadose zone steady state flow: an assessment of its capability to predict transport in a realistic combined vadose zone-groundwater flow system. Water Resour. Res. 44.

Russo et al., 1998 Russo, D., J. Zaidel, and A. Laufer. 1998. Numerical analysis of flow and transport in a three-dimensional partially saturated heterogeneous soil. Water Resour. Res. 34:1451-1468.

Salamon et al., 2006 Salamon, P., D. Fernandez-Garcia, and J.J. Gomez-Hernandez. 2006. A review and numerical assessment of the random walk particle tracking method. J. Contam. Hydrol. 87:277-305.

Salamon et al., 2007 Salamon, P., D. Fernandez-Garcia, and J.J. Gomez-Hernandez. 2007. Modeling tracer transport at the MADE site: The importance of heterogeneity. Water Resour. Res. 43(8).

Samouelian et al., 2007 Samouelian, A., H.J. Vogel, and O. Ippisch. 2007. Upscaling hydraulic conductivity based on the topology of the sub-scale structure. Adv. Water Resour. 30:1179-1189.

Samouelian et al., 2011 Samouelian, A., I. Cousin, C. Dages, A. Frison, and G. Richard. 2011. Determining the effective hydraulic properties of a highly heterogeneous soil horizon. Vadose Zone J. 10:450-458.

Schafer-Perini and Wilson, 1991 Schafer-Perini, A.L., and J.L. Wilson. 1991. Efficient and accurate front tracking for 2-dimensional groundwater-flow models. Water Resour. Res. 27:1471-1485.

Schröder et al., 2011 Schröder, N., M. Javaux, B. Steffen, B. Körfgen, J. Vanderborght, and H. Vereecken. 2011. Impact of 3-D root uptake on solute transport: a numerical study. Geophysical Research Abstracts, Vol. 13, EGU General Assembly, 3-7 April 2011, Vienna, Austria.

Schwartz et al., 2009a Schwartz, R.C., S.R. Evett, and J.M. Bell. 2009a. Complex permittivity model for time domain reflectometry soil water content sensing: II. Calibration. Soil Sci. Soc. Am. J. 73:898-909.

Schwartz et al., 2009b Schwartz, R.C., S.R. Evett, M.G. Pelletier, and J.M. Bell. 2009b. Complex permittivity model for time domain reflectometry soil water content sensing: I. Theory. Soil Sci. Soc. Am. J. 73:886-897.

Seeboonruang and Ginn, 2006 Seeboonruang, U., and T. R. Ginn. 2006. Upscaling heterogeneity in aquifer reactivity via exposure-time concept: Forward model. J. Contam. Hydrol., 84(3-4):127-154.

Seitz, 2002 Seitz, J.L. 2002. Global issues: an introduction. 2nd ed. Wiley-Blackwell, Oxford.

Semra et al., 1993 Semra, K., P. Ackerer, and R. Mose. 1993. Three dimensional groundwater quality modeling in heterogeneous media, p. 3-11, In L. C. Wrobel and C. A. Brebbia, eds. Water pollution II: modelling, measuring and prediction. Southampton, UK.

Seneviratne et al., 2006 Seneviratne, S.I., D. Luthi, M. Litschi, and C. Schar. 2006. Land-atmosphere coupling and climate change in Europe. Nature 443:205-209.

Shahraeeni and Or, 2010 Shahraeeni, E., and D. Or. 2010. Thermo-evaporative fluxes from heterogeneous porous surfaces resolved by infrared thermography. Water Resour. Res. 46.

Shokri et al., 2008a Shokri, N., P. Lehmann, and D. Or. 2008a. Effects of hydrophobic layers on evaporation from porous media. Geophys. Res. Lett. 35.

Shokri et al., 2008b Shokri, N., P. Lehmann, P. Vontobel, and D. Or. 2008b. Drying front and water content dynamics during evaporation from sand delineated by neutron radiography. Water Resour. Res. 44.

Shuai et al., 2009 Shuai, X.F., O. Wendroth, C.C. Lu, and C. Ray. 2009. Reducing the complexity of inverse analysis of time domain reflectometry waveforms. Soil Sci. Soc. Am. J. 73:28-36.

Silliman et al., 1998 Silliman, S.E., L. Zheng, and P. Conwell. 1998. The use of laboratory experiments for the study of conservative solute transport in heterogeneous porous media. Hydrogeology J. 6:166-177.

Simunek et al., 1995 Simunek, J., K. Huang, and M.T. van Genuchten. 1995. The SWMS-3D code for simulating water flow and solute transport in three-dimensional variably-saturated media, Version 1.0. Res. Rep. 139. U.S. Salinity Lab, Riverside, CA.

Simunek et al., 2008 Simunek, J., M.T. van Genuchten, and M. Sejna. 2008. Development and applications of the HYDRUS and STANMOD software packages and related codes. Vadose Zone J. 7:587-600.

Singha and Gorelick, 2005 Singha, K., and S.M. Gorelick. 2005. Saline tracer visualized with three-dimensional electrical resistivity tomography: field-scale spatial moment analysis. Water Resour. Res. 41.

Singha and Gorelick, 2006 Singha, K., and S.M. Gorelick. 2006. Hydrogeophysical tracking of three-dimensional tracer migration: The concept and application of apparent petrophysical relations. Water Resour. Res. 42.

Slater et al., 2002 Slater, L., A. Binley, R. Versteeg, G. Cassiani, R. Birken, and S. Sandberg. 2002. A 3D ERT study of solute transport in a large experimental tank. J. Appl. Geophys. 49:211-229.

Smets et al., 1997 Smets, S.M.P., M. Kuper, J.C. Van Dam, and R.A. Feddes. 1997. Salinization and crop transpiration of irrigated fields in Pakistan's Punjab. Agric. Water Manage. 35:43-60.

Suzuki and Maeda, 1968 Suzuki, M., and S. Maeda. 1968. On the mechanism of drying granular beds: Mass transfer from discontinuous source. J. Chem. Eng. Jpn. 1:26-31.

Thomsen et al., 2007 Thomsen, A., K. Schelde, P. Droscher, and F. Steffensen. 2007. Mobile TDR for geo-referenced measurement of soil water content and electrical conductivity. Precis. agric. 8:213-223.

Tompson and Gelhar, 1990 Tompson, A.F.B., and L.W. Gelhar. 1990. Numerical-simulation of solute transport in 3-dimensional, randomly heterogeneous porous-media. Water Resour. Res. 26:2541-2562.

Topp et al., 1980 Topp, G.C., J.L. Davis, and A.P. Annan. 1980. Electromagnetic determination of soil-water content - measurements in coaxial transmission-lines. Water Resour. Res. 16:574-582.

Uffink, 1985 Uffink, G.J.M. 1985. A random-walk method for the simulation of macrodispersion in a stratified aquifer. IAHS symposia, IUGG 18th General Assembly 65:26-34.

Ursino and Gimmi, 2004 Ursino, N and T. Gimmi. 2004. Combined effect of heterogeneity, anisotropy and saturation on steady state flow and transport: Structure recognition and numerical simulation. Water Resour. Res. 40.

Ursino et al., 2001 Ursino, N., T. Gimmi, and H. Flühler. 2001. Combined effects of heterogeneity, anisotropy, and saturation on steady state flow and transport: A laboratory sand tank experiment. Water Resour. Res. 37:201-208.

van Duin, 1963 van Duin, R.H.A. 1963. The influence of soil management on the temperature wave near the soil surface. Technical Bulletin 29, Institute for Land and Water Management Research, Wageningen.

van Genuchten, 1980 van Genuchten, M.T. 1980. A closed-form equation for predicting the hydraulic conductivity of unsaturated soils. Soil Sci. Soc. Am. J. 44:892-898.

van Genuchten and Parker, 1984 van Genuchten, M.T., and J.C. Parker. 1984. Boundary-conditions for displacement experiments through short laboratory soil columns. Soil Sci. Soc. Am. J. 48:703-708.

Vanclooster et al., 2005 Vanclooster, M., M. Javaux, and J. Vanderborght. 2005. Solute transport in soil at the core and field scale. In M. G. Anderson (ed.) Encyclopedia of Hydrological Sciences. Wiley, New York.

Vanderborght et al., 1998 Vanderborght, J., D. Mallants, and J. Feyen. 1998. Solute transport in a heterogeneous soil for boundary and initial conditions: Evaluation of first-order approximations. Water Resour. Res. 34:3255-3270.

Vanderborght et al., 2006 Vanderborght, J., R. Kasteel, and H. Vereecken. 2006. Stochastic continuum transport equations for field-scale solute transport: overview of theoretical and experimental results. Vadose Zone J. 5:184-203.

Vasin et al., 2008 Vasin, M., P. Lehmann, A. Kaestner, R. Hassanein, W. Nowak, R. Helmig, and I. Neuweiler. 2008. Drainage in heterogeneous sand columns with different geometric structures. Adv. Water Resour. 31:1205-1220.

Vereecken et al., 2007 Vereecken, H., R. Kasteel, J. Vanderborght, and T. Harter. 2007. Upscaling hydraulic properties and soil water flow processes in heterogeneous soils: a review. Vadose Zone J. 6:1-28.

Vogel and Roth, 2003 Vogel, H.J., and K. Roth. 2003. Moving through scales of flow and transport in soil. J. Hydrol. 272:95-106.

Vogel et al., 2006 Vogel, H.J., I. Cousin, O. Ippisch, and P. Bastian. 2006. The dominant role of structure for solute transport in soil: experimental evidence and modelling of structure and transport in a field experiment. Hydrol. Earth Syst. Sci. 10:495-506.

Weissmann et al., 2002 Weissmann, G.S., Y. Zhang, E. M. LaBolle, and G. E. Fogg. 2002. Dispersion of groundwater age in an alluvial aquifer system. Water Resour. Res. 38(10).

Wildenschild, 1999a Wildenschild, D.Y.Y. 1999a. Numerical modeling of observed effective flow behavior in unsaturated heterogeneous sands. Water Resour. Res. 35:29-42.

Wildenschild, 1999b Wildenschild, D.Y.Y. 1999b. Laboratory investigations of effective flow behavior in unsaturated heterogeneous sands. Water Resour. Res. 35:17-27.

Wraith et al., 2005 Wraith, J.A., D.A. Robinson, S.B. Jones, and D.S. Long. 2005. Spatially characterizing apparent electrical conductivity and water content of surface soils with time domain reflectometry. Comput. Electron. Agric. 46:239-261.

Yoon et al., 2008 Yoon, H., C.Y. Zhang, C.J. Werth, A.J. Valocchi, and A.G. Webb. 2008. Numerical simulation of water flow in three dimensional heterogeneous porous media observed in a magnetic resonance imaging experiment. Water Resour. Res. 44.

Yu and Drnevich, 2004 Yu, X., and V.P. Drnevich. 2004. Soil water content and dry density by time domain reflectometry. J. Geotech. Geoenviron. Eng. 130:922-934.

Zhang et al., 2009 Zhang, Y., E.M. LaBolle, and K. Pohlmann. 2009. Monte Carlo simulation of superdiffusion and subdiffusion in macroscopically heterogeneous media. Water Resour. Res. 45.

Appendix A

Reference root mean square error

Let C_i be the concentration in the element i with the volume ΔV_i and the water content θ_i. If we have $n_{par,tot}$ particles for the entire domain, and if we distribute these particles in the domain in such a way that the concentration C_i in each element is the same, we have $n_{par,i}$ particles in the element i,

$$n_{par,i} = n_{par,tot} \frac{\theta_i \Delta V_i}{\sum\limits_i \theta_i \Delta V_i} \tag{A.1}$$

The fraction of particles in the element i is equal to the probability p_i that a particle is in the element i,

$$p_i = \frac{n_{par,i}}{n_{par,tot}} = \frac{\theta_i \Delta V_i}{\sum\limits_i \theta_i \Delta V_i} n_{par,tot}^{-1} \tag{A.2}$$

The concentration in the element i is related to the fraction of particles in the element i as

$$C_i = \frac{n_{par,i} m_{par}}{\theta_i \Delta V_i} = \frac{n_{par,tot} m_{par}}{\theta_i \Delta V_i} p_i \tag{A.3}$$

Instead of distributing the $n_{par,tot}$ over the domain so that the concentration is uniform, the particles can also be distributed according to a random process with a probability p_i that a particle is placed in the element i. If this random process is repeated for $n_{par,tot}$ particles, the expected value of the fraction of particles in the element i,f_i, is equal to p_i. The variance of f_i, $\sigma^2_{f_i}$ is

$$\sigma^2_{f_i} = \frac{p_i(1-p_i)}{n_{par,tot}} \tag{A.4}$$

The concentration that is derived from f_i is

$$\hat{C}_i = \frac{n_{par,tot} m_{par}}{\theta_i \Delta V_i} f_i \tag{A.5}$$

where m_{par} is the mass of a single particle. Its expected value is equal to $\hat{C}_i$ and its variance is equal to

$$\sigma^2_{\hat{C}_i} = \left(\frac{n_{par,tot} m_{par}}{\theta_i \Delta V_i}\right)^2 \frac{p_i(1-p_i)}{n_{par,tot}} = n_{par,tot} \left(\frac{m_{par}}{\theta_i \Delta V_i}\right)^2 p_i(1-p_i) \tag{A.6}$$

Using the equation for p_i, this gives

$$\sigma^2_{\hat{C}_i} = n_{par,tot} \left(\frac{m_{par}}{\theta_i \Delta V_i}\right)^2 \frac{\theta_i \Delta V_i}{\sum\limits_i \theta_i \Delta V_i} \left(1 - \frac{\theta_i \Delta V_i}{\sum\limits_i \theta_i \Delta V_i}\right) \tag{A.7}$$

If m_{par} is defined so that the overall average concentration is equal to 1, then m_{par} is equal to

$$m_{par} = \frac{\sum\limits_i \theta_i \Delta V_i}{n_{par,tot}} \tag{A.8}$$

As a consequence, the expected value of $\hat{C}_i = 1$ and its variance is

$$\sigma^2_{\hat{C}_i} = \frac{1}{n_{par,tot}} \left(\frac{\sum\limits_i \theta_i \Delta V_i}{\theta_i \Delta V_i}\right)^2 \frac{\theta_i \Delta V_i}{\sum\limits_i \theta_i \Delta V_i} \left(1 - \frac{\theta_i \Delta V_i}{\sum\limits_i \theta_i \Delta V_i}\right) \tag{A.9}$$

which simplifies to

$$\sigma^2_{\hat{C}_i} = \frac{1}{n_{par,tot}} \left(\frac{\sum\limits_i \theta_i \Delta V_i}{\theta_i \Delta V_i} - 1\right) \tag{A.10}$$

The root mean square error RMSE is the root of the average of the variances in all elements,

$$\text{RMSE} = \sqrt{\frac{\sum\limits_i \sigma^2_{\hat{C}_i}}{n_{elements}}} \tag{A.11}$$

Appendix B

Photographic documentation of the construction of the laboratory soil

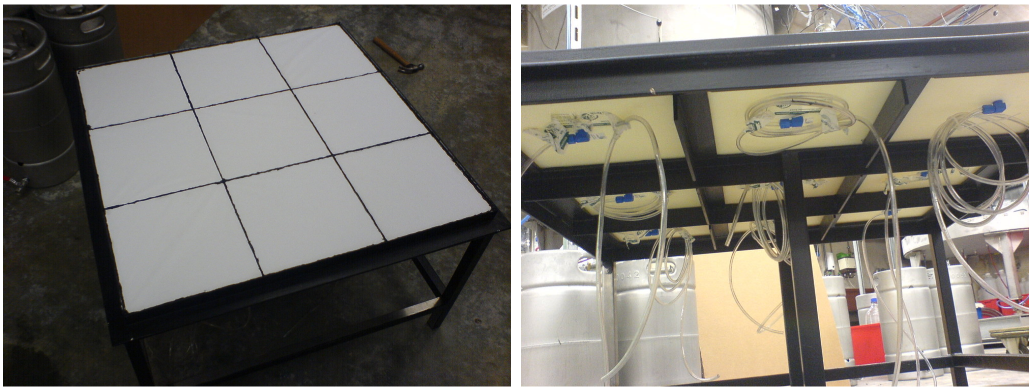

Figure B.1: Left: top view on steel frame and suction plates; right: bottom view on steel frame and suction plates.

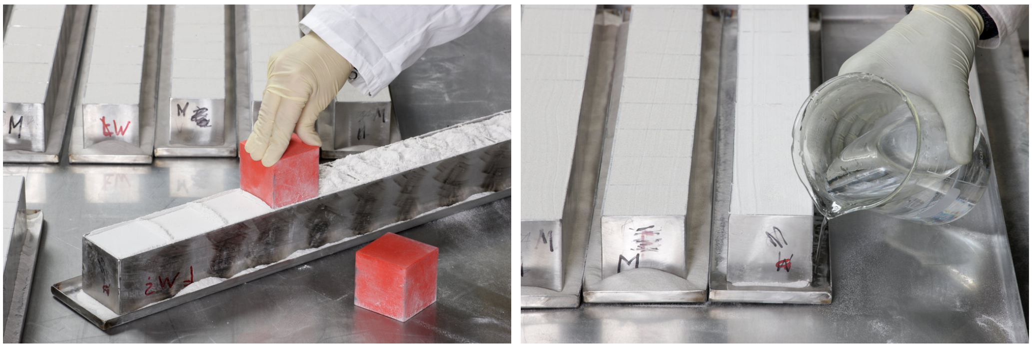

Figure B.2: Left: filling and packing of the cubic frames; right: bottom-up saturation of the substrate.

Figure B.3: Left: Freezing of the cubes; right: removing the cubes from the frames.

Figure B.4: Left: frozen cubes are packed into the sandbox; right: view at the evaporation chamber.

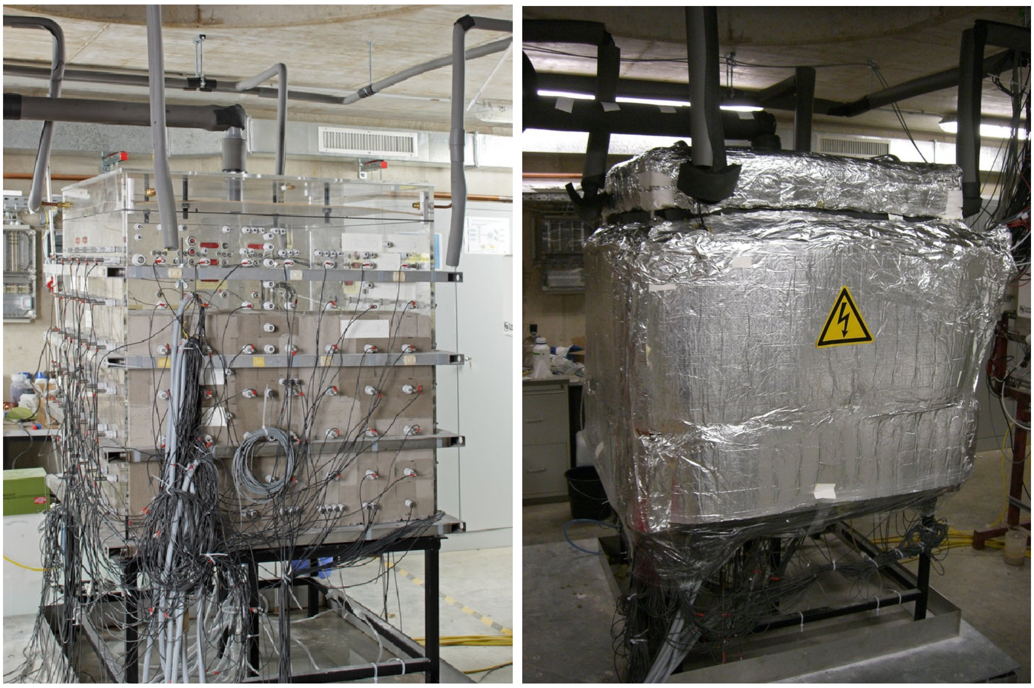

Figure B.5: Left: view at the partly filled laboratory soil; right: view at the insulated laboratory soil.

Appendix C

Accurate determination of the bulk electrical conductivity with the TDR100 cable tester*

Abstract

Time Domain Reflectometry (TDR) is commonly used to determine the soil bulk electrical conductivity. To obtain accurate measurements, the three parameters of a series resistor model (probe constant, K_p; cable resistance, R_C; and remaining resistance, R_0) are typically calibrated using liquids with known electrical conductivity. Several studies have reported discrepancies between calibrated and directly measured parameters of the series resistor model. Here, we suggest that a technical issue with the TDR100 cable tester contributed to part of these inconsistencies. Our results show that with an increasing level of waveform averaging the reflection coefficient, as well as the calibration parameters K_p, R_C, and R_0, approached a maximum value. A comparison with independently determined values indicated that a high level of waveform averaging provided the physically most plausible results. Based on our results, we propose to average at least 16 waveforms each consisting of at least 250 points. An oscilloscope-based signal analysis showed that the increase in reflection coefficient with increasing waveform averaging in saline media is related to a capacitance associated with electrode polarization in combination with a change in the pulse period of the pulse train when the TDR100 starts collecting data points. This capacitance resulted in a slow change of the average voltage in the TDR pulse train until a stable average voltage was reached. Higher levels of waveform averaging cancel the impact of the first erroneous voltage measurements out. In practical applications, the errors in the determination of the bulk electrical conductivity can be as high as 5 % for the low conductivity range (< 0.1 S m^{-1}) and up to 370 % in saline media (1.4 S m^{-1}), when waveform averaging is changed after calibration.

---

[*] adapted from: Bechtold, M., J.A. Huisman, L. Weihermüller, and H. Vereecken. 2010. Accurate determination of the bulk electrical conductivity with the TDR100 cable tester. Soil Sci. Soc. Am. J. 74:495-501.

C.1 Introduction

The advantage of simultaneously measuring water content and bulk electrical conductivity in the same sample volume led to abundant applications of Time Domain Reflectometry (TDR) in vadose zone studies (Robinson et al., 2003; Wraith et al., 2005; Koestel et al., 2008). Although being a standard method nowadays, the accurate determination of bulk electrical conductivity using TDR was recently discussed controversially (Huisman and Bouten, 1999; Castiglione and Shouse, 2003; Evett et al., 2005; Huisman and Vereecken, 2006; Lin et al., 2007; Huisman et al., 2008; Lin et al., 2008). With the introduction of water content estimation models that consider bulk conductivity in addition to apparent permittivity (Evett et al., 2005; Schwartz et al., 2009a; Schwartz et al., 2009b), the importance of accurate electrical conductivity measurements has increased even more.

Based on the work of Giese and Tiemann (1975), who were the first to apply TDR to determine sample resistance, the load resistance, R_L (Ω), is now commonly determined using the reflection coefficient at long times, ρ_∞ (-),

$$R_L = R_{out}\frac{1+\rho_\infty}{1-\rho_\infty} \tag{C.1}$$

where R_{out} is the output resistance of the cable tester (50 Ω). The inverse of the load resistance is the TDR sample conductance. The load resistance is related to the bulk electrical conductivity of the sample, σ_b (S m^{-1}), by a geometric factor K_p (m^{-1}), which is often called the probe constant,

$$\sigma_b = \frac{K_p}{R_L}. \tag{C.2}$$

K_p depends on the probe geometry and can either be calibrated (for procedures see below) or calculated from

$$K_p = \frac{\varepsilon_0 c Z_0}{L_p} \tag{C.3}$$

where ε_0 is the dielectric permittivity of free space (8.854 × 10^{-12} F m^{-1}), c is the speed of light (3 × 10^{8} m s^{-1}), L_p is the length of the probe (m), and Z_0 is the characteristic impedance of the probe (Ω). The only unknown, Z_0, can be determined using the analytical expressions of Ball (2002),

$$Z_0 = \frac{1}{2\pi\left(n-1\right)}\sqrt{\frac{\mu_0}{\varepsilon_0}}\ln\left(H+\sqrt{H^2-1}\right) \tag{C.4}$$

with

$$H = \frac{\left(s^2-r^2\right)^{n-1}-r^{2(n-1)}}{r^{n-1}\left[\left(s+r\right)^{n-1}-\left(s-r\right)^{n-1}\right]} \tag{C.5}$$

where n is the number of wires of the TDR probe, r is the radius of the wires (m), s is the spacing between the middle of the inner wire and the outer wire (m), and μ_0

is the magnetic permeability of free space ($4\pi \times 10^{-7}$ H m^{-1}). Eq. C.4 is valid for all probe designs where s is identical for all outer wires and where the outer wires have the same sector of angle $2\pi/(n\text{-}1)$.

For longer cables and higher electrical conductivity values, the effect of additional resistances of the coaxial cable, probe head, connectors and multiplexers cannot be neglected. To account for these resistances, Heimovaara et al. (1995) modified Eq. C.4 assuming a series resistor model,

$$\sigma_b = \frac{K_p}{R_L - (l_C R_C + R_0)} \tag{C.6}$$

where l_C is cable length (m), R_C is cable resistance (Ωm^{-1}), and R_0 represents additional series resistances (Ω) independent of cable length (i.e. connectors, multiplexers). The model parameters of the series resistor model can be obtained in two different ways: (1) by performing TDR measurements in multiple solutions of varying electrical conductivity to get a set of ρ_∞ and independently determined electrical conductivity values, which is then fitted with Eq. C.6 by using appropriate optimization algorithms (Heimovaara et al., 1995; Mallants et al., 1996) or (2) by calculating K_p from analytical expressions (e. g., Ball, 2002, see below), and by directly measuring cable resistance using shorted cables (Reece, 1998).

Although the series resistor model is physically sound, several studies exist in which the correctness or completeness of the series resistor model is questioned (Heimovaara et al., 1995; Huisman and Bouten, 1999; Castiglione and Shouse, 2003; Huisman et al., 2008). These doubts originated from significant differences between model parameters using these two calibration methods. Huisman and Bouten (1999) found that the simultaneous fitting of cable and probe properties led to more accurate electrical conductivity measurements than directly measuring cable resistance. Recently, Huisman et al. (2008) supported this and further showed that the fitting procedure may correct for deviations from the theory, which indicates that a physical interpretation of the model parameters might not be appropriate.

The doubts on the completeness of the series resistor model fueled the development of an alternative calibration approach presented by Castiglione and Shouse (2003). They used measurements in air ($\sigma_b = 0$) and with a shortened TDR probe ($\sigma_b = \infty$) to linearly rescale the steady-state reflection coefficient between -1.0 and 1.0. The probe constant calibration after Castiglione and Shouse (2003) obtained broad acceptance and was applied in several recent studies (e. g., Ritter et al., 2005; Wraith et al., 2005; Cataldo et al., 2008; Lundmark and Jansson, 2008). Recently, Lin et al. (2007) demonstrated that the Castiglione-Shouse scaling method is theoretically incorrect because the effect of cable resistance on ρ_∞ is nonlinear. In practice however, an accurate probe calibration can still be obtained by using the Castiglione-Shouse scaling method because fitting the probe constant to known electrical conductivity values can compensate for the theoretical error. The disadvantage is that the probe constant no longer depends solely on the TDR probe dimensions but also depends on cable length, which practically means that each TDR probe has to be calibrated individually.

Based on circuit theory and full waveform analysis, Lin et al. (2007; 2008) stressed that the series resistor model is physically sound. They attributed inconsistencies between calibrated and directly measured model parameters reported in literature to recording time issues (Lin et al., 2007) and measurement errors in the reflection coefficient due to imperfect voltage amplitude calibration (Lin et al., 2008). Lin et al. (2007) showed that longer cable lengths as well as very low and high electrical conductivity values can extend the time to reach the steady-state reflection coefficient. As a simple guideline, they suggested to take ρ_∞ after at least 10 multiple reflections within the probe and three multiple reflections within the coaxial cable. The imperfect voltage amplitude calibration is evident from open-circuit measurements, which are known to vary between 0.96 and 1.00 for the TDR100 device (Huisman et al., 2008; Lin et al., 2008). To avoid errors in low conductive samples, this deviation from an optimal open-circuit measurement can be accounted for by a cable-tester-specific correction (Lin et al., 2008),

$$\rho_{corr} = \frac{2\,(\rho + 1)}{(\rho_{open} + 1)} - 1 \tag{C.7}$$

where ρ is the actual reflection coefficient, ρ_{open} is the reflection coefficient of an open-circuit measurement, and ρ_{corr} is the resulting corrected reflection coefficient.

Besides recording time issues and imperfect voltage amplitude calibration, we present an additional technical issue of the TDR100 cable tester that can also lead to experimental deviations from the series resistor model. This technical issue is related to a change in the pulse period of the pulse train when the TDR100 cable tester starts collecting data points in association with electrode polarization effects in saline environments. The objective of this study is to illustrate the implications of this technical issue for accurate measurements of electrical conductivity. The TDR100 is widely used in a broad variety of studies (e. g., Yu and Drnevich, 2004; Blonquist et al., 2005; Thomsen et al., 2007; Cataldo et al., 2008; Koestel et al., 2008; Shuai et al., 2009).

C.2 Materials and methods

The TDR measurements were performed using a Campbell Scientific (Logan, UT) setup composed of a TDR100 cable tester, two levels of SDMX multiplexers (50 Ω) and a CR3000 data logger to acquire the waveforms. The TDR probe was designed and constructed in-house using RG58 C/U cable (probe characteristics: 3 wires, 0.11 m long, 0.02 m spacing, 0.002 m radius, spacing/radius = 10, $K_p = 4.48$ m^{-1} according to Eq. C.3 to C.5). The reflection coefficient at long times was determined by averaging the last 10 of 251 reflection coefficient measurements between 192.8

and 200 m apparent length using a relative propagation velocity (v_p) of 1, which corresponds to the speed of light in free space. The automatic routine of the TDR100 also uses 200 m to determine the reflection coefficient at long times (Campbell Scientific, personal communication, 2007). It should be noted that the reflection coefficient is determined from a pulse with finite width, so the common assumption that TDR measures DC electrical conductivity is not valid. With the reported pulse width of 18 μs for the TDR100, the frequency associated with the electrical conductivity measurements made with TDR is in the kHz range. The maximum cable length considered here was 29.5 m, which means that our time window fulfilled the guidelines for obtaining steady-state reflection coefficients proposed by Lin et al. (2007). A cable-tester-specific open reflection coefficient (after Lin et al., 2008) was obtained by taking the average of 45 measurements at three different cable lengths (9.5, 19.5, and 29.5 m). This resulted in a mean ρ_{open} of 0.9648 with a standard deviation of 0.0013.

We followed the two-step calibration approach proposed by Huisman et al. (2008) to determine the cable and probe properties (Fig. C.1). This approach suggests using eight reference solutions with known electrical conductivity. Four of these solutions should have a low electrical conductivity, which will provide information on the geometric factor K_p. The remaining four solutions should have a high electrical conductivity to estimate the additional resistances of the series resistor model. The electrical conductivities of the reference solutions were measured independently with a standard electrical conductivity meter (Cond 340i / TetraCon 325, WTW, Weilheim, Germany). The solutions with a low electrical conductivity ranged from 0.005 to 0.03 S m^{-1} resulting in ρ_∞ values between 1.0 and 0.5, and the high conductivity solutions ranged from 0.5 to 2.8 S m^{-1} resulting in ρ_∞ values between -0.5 and -1.0. In a first step, we determined the probe constant by fitting Eq. C.2 to the low conductivity data, whereby cable losses were neglected. In a second step, the high conductivity data were used to determine the cable resistance parameters of Eq. C.6 while keeping the probe constant fixed (Fig. C.1). In both steps, parameter optimization was performed by minimizing the sum of squared residuals (SSR) between measured and modeled electrical conductivity using the Simplex algorithm (Nelder and Mead, 1965) implemented in Matlab.

The calibration as well as the direct measurement method rely on the accurate determination of the reflection coefficient at long times. To reduce noise in the acquired waveforms, the TDR100 cable tester provides the option to average automatically over multiple waveforms. Averaging is accomplished by collecting multiple values at a given distance (time) before collecting values at the next distance (time) increment (Campbell Scientific Inc., 2007). To investigate the effect of using different numbers of waveform averages (further referred to as WavAvg), calibration sequences were performed using WavAvg = 1, 4, 16, 64, and 128. Further, we used three different

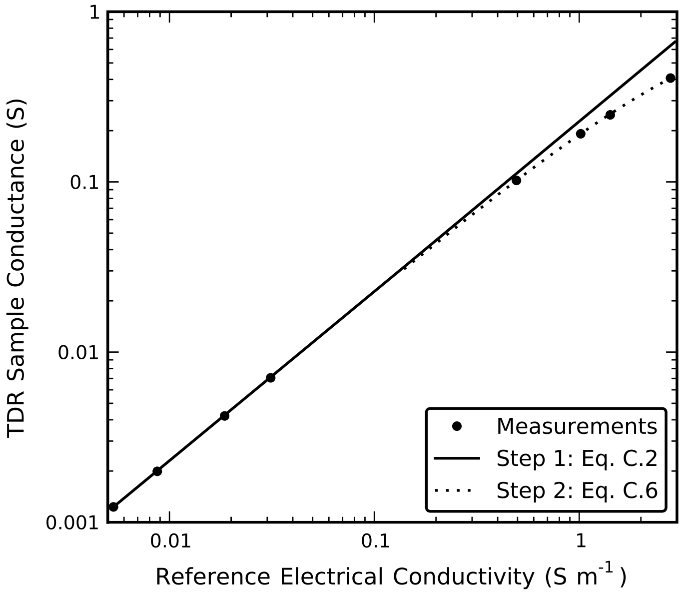

Figure C.1: Two-step calibration approach after Huisman et al. (2008). The figure shows the measured (markers) and modeled (lines) TDR sample conductance (inverse of the load resistance provided by Eq. C.1) as a function of reference electrical conductivity. The slope of the model at low electrical conductivity corresponds with $1/K_p$. In step 1, Eq. C.2 is fitted to the data (solid line). In step 2, the series resistor model Eq. C.6 is fitted to the data while probe constant K_p of step 1 is fixed (solid line). Please note that both axes are plotted logarithmically to visualize the entire range of reference electrical conductivities used to determine the model parameters.

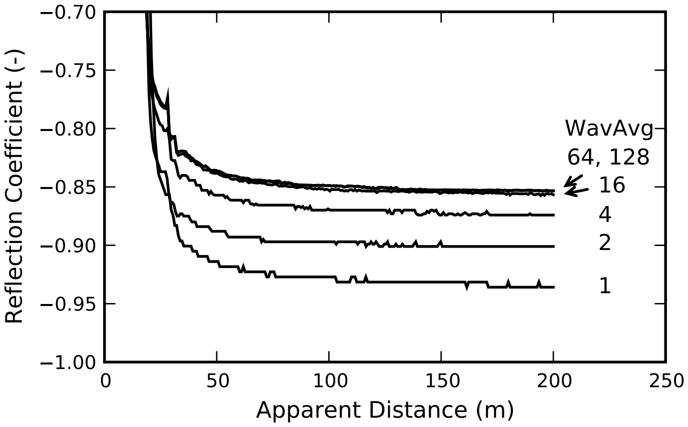

Figure C.2: Reflection coefficient vs. apparent distance. Measurements in a reference solution of 1.4 S m^{-1} for five different numbers of waveform averages (WavAvg = 1, 4, 16, 64, and 128) and with a cable length of 9.5 m.

cable lengths (9.5, 19.5, and 29.5 m), which allowed us to determine R_C and R_0.

C.3 Results and discussion

The intention of the WavAvg option of the TDR100 is to reduce signal noise by averaging over multiple waveforms. However, we noticed that, besides reducing signal noise, there was a significant upward change in the value of the reflection coefficient at long times when the number of waveform averages was increased (Fig. C.2). With increasing averaging, the measured reflection coefficient seemed to approach a maximum value. Using the average of 16 waveforms should be sufficient to approximate this maximum value.

As the series resistor model is considered to be physically sound, it is useful to determine which level of waveform averaging provides the physically most plausible probe and cable properties. Therefore, we performed the two-step calibration procedure for five levels of waveform averaging using a cable length of 9.5 m. For both smaller and larger WavAvg values, the measured TDR sample conductance values can be perfectly fitted by the series resistor model, i.e. Eq. C.6 (see Fig. C.3). The combined resistance of the cable, connectors and cable tester ($l_C R_C + R_0$ in Eq. C.6) increased from -1.28 Ω for a WavAvg of 1 to 0.88 Ω for a WavAvg of 128. Since negative resistance are physically implausible, this demonstrates that a perfect fit of the model to the experimental data does not obligatory prove that the calibration results are physically consistent. This supports the assumption of Huisman and Bouten (1999) that the series resistor model can correct for deviations from theory.

To study the effect of waveform averaging on the calibration parameters K_p, R_C, and R_0 in more detail, we made measurements for two additional cable lengths (19.5 and 29.5 m). With increasing waveform averaging, K_p increased and approached a maximum value of 4.42 ± 0.02 m^{-1} (Fig. C.4). At WavAvg = 1, K_p was underestimated

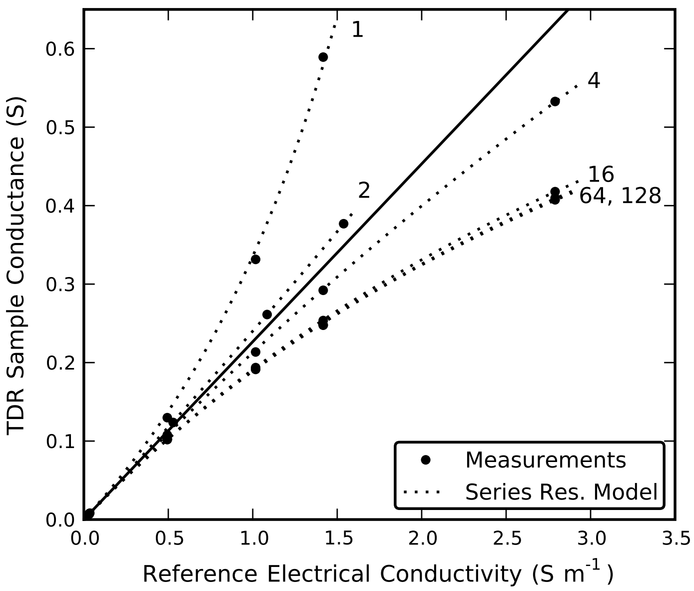

Figure C.3: Measured (markers) and modeled (lines) TDR sample conductance as a function of reference electrical conductivity for different numbers of waveform averages (WavAvg = 1, 4, 16, 64, and 128) and with a cable length of 9.5 m.

by about 5 %. For a cable length of 9.5 m, we performed one additional calibration using WavAvg = 2 to demonstrate that the results indeed approach a maximum value. The maximum value of K_p was reached at a WavAvg value of 16 for all cable lengths. The existence of a maximum K_p value indicates that physically more reasonable results are obtained when averaging is increased. This is supported by the K_p value obtained from Eq. C.3 - C.5, which was 4.48 ± 0.10 m^{-1} for our TDR probe design. The uncertainty of this analytically derived K_p was obtained from Huisman et al. (2008).

To divide the calibrated total resistance (R) into a contribution from the cable resistance (R_C) and the remaining resistance (R_0) we fitted the linear expression $R = l_C R_C + R_0$ to the calibration results for each WavAvg value. Both R_0 and R_C show lower values for lower WavAvg (Fig. C.5). The extra series resistance R_0 is negative for WavAvg values of 1 and 4, which cannot be explained physically. A negative value for R_0 was also reported by Huisman et al. (2008), leading to doubts on the physical meaning of R_0. R_0 is supposed to be a small positive value related to the resistance of the cable tester and any additional devices except the cable itself (Lin et al., 2007). The maximum value for R_0 that is approached with increasing WavAvg is about 0.30 ± 0.05 Ω (Fig. C.6). This corresponds well to the one directly measured by Huisman et al. (2008) for a TDR100 in a similar setup. The maximum value for R_C is 0.058 ± 0.001 Ω m^{-1} (Fig. C.7), which also corresponds well with direct measurements for this cable type as reported by Reece (1998), Huisman and Bouten (1999) and Huisman et al. (2008).

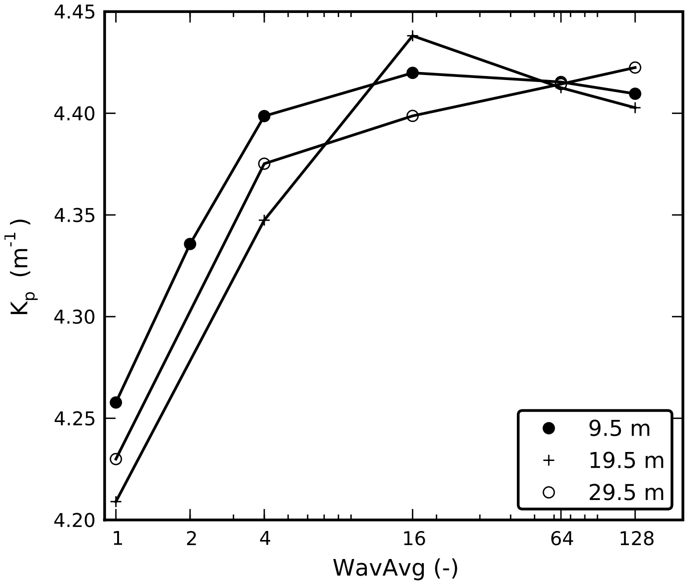

Figure C.4: Probe constant (K_p) as a function of waveform averages (WavAvg) for three different cable lengths (9.5, 19.5, and 29.5 m).

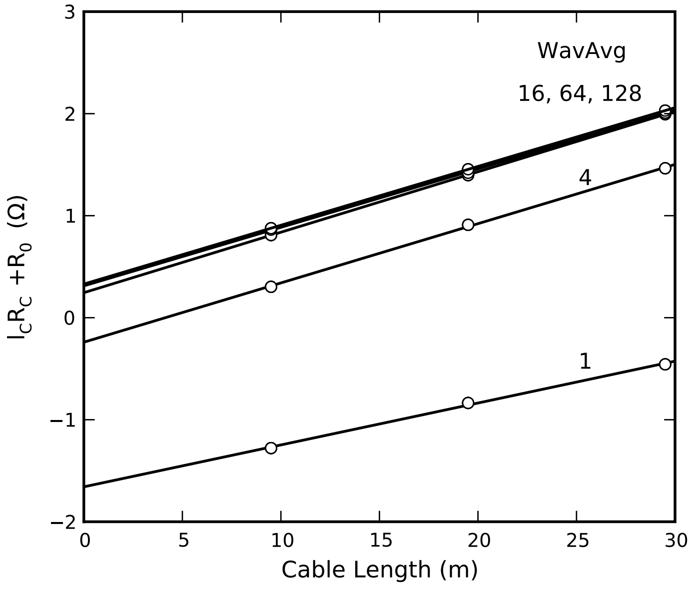

Figure C.5: Measured (markers) and modeled (lines) sum of cable resistance and remaining resistance ($l_C R_C$+R_0) as a function of cable length for five different numbers of waveform averages (WavAvg = 1, 4, 16, 64, and 128).

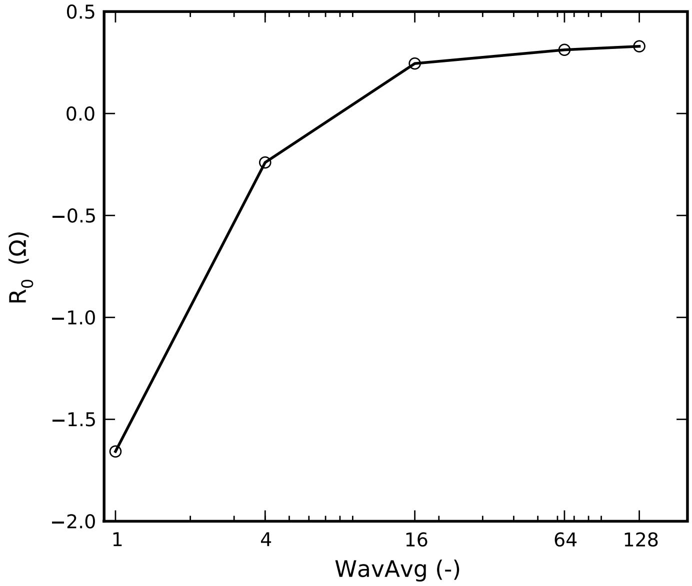

Figure C.6: Remaining resistance (R_0) as a function of waveform averages (WavAvg).

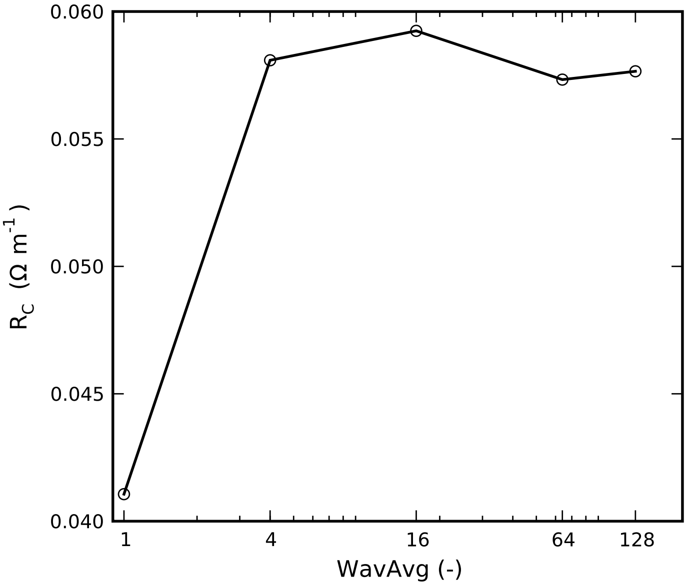

Figure C.7: Cable resistance (R_C) as a function of waveform averages (WavAvg).

To investigate the inaccurate reflection coefficients with low waveform averaging, we connected the TDR100 to a high speed oscilloscope (Tektronix TDS5034B with a bandwidth of 350 MHz and 5 GHz sampling speed). In a first step, we investigated the pulse train emitted by the TDR100. For this, it is important to know that for each point in the TDR waveform a pulse is emitted. We found that the pulse train consisted of two parts. The length of the first part of the pulse train was independent of the waveform acquisition parameters (number of points in TDR waveform and WavAvg), and, therefore, we refer to this part as the pre-train. The length of the second part of the pulse train did depend on the waveform acquisition parameters, and we refer to this part as the main pulse train. In addition, we found that the pulse width was 18 μs and the pulse period (pulse width + pause between two pulses) was 83 μs in the pre-train. In the main pulse train, the pulse width was identical but the pulse period was 100 μs. Using these pulse periods, it was determined that the pre-train consisted of about 7600 pulses, and that the number of pulses in the main train equaled 2 times the number of points in the TDR waveform multiplied with WavAvg. The TDR100 releases the pulses from a negative voltage level that is applied just before the start of the pulse train. In the pulse train the average voltage of a complete pulse period (pulse width and pulse pause) is not zero, i.e. the pulse train is not symmetric around zero voltage. Because the ratio between the pulse width and pulse period was lower in the main train, the average voltage observed with the oscilloscope was lower, as schematically indicated in Fig. C.8. It was also observed that no pulses were emitted between TDR measurements.

In a next step, we attached a coaxial cable terminated with a 2.5 Ω resistor, corresponding to the measured load resistance for the highest electrical conductivity (2.8 $\mathrm{Sm^{-1}}$, see Fig. C.3), to the cable tester and the oscilloscope. This termination was the simplest electrical analogue of a TDR measurement in a saline solution. However, it was observed that the reflection coefficient did not vary when WavAvg was changed for this type of termination. This indicates that the TDR100 works well in case of a high load that is purely resistive.

It is well established that electrical measurements in conductive media are affected by electrode polarization. A first approximate electrical analogue of a TDR measurement in a saline solution affected by electrode polarization is a resistor and a capacitor in series (Fig. C.8), which is also known as a RC circuit. Therefore, we attached a coaxial cable terminated with a 2.5 Ω resistor and a 1000 μF capacitor in series to the cable tester and the oscilloscope. With this termination, the reflection coefficient did vary when WavAvg was changed, as was observed for TDR measurements in saline solutions. The resulting average voltage in the pulse train with this termination is shown schematically at the bottom of Fig. C.8. Because of the charge transfer in the capacitor, the average voltage in the pulse train slowly increased to a steady level in the pre-train. Because the average voltage decreased between the

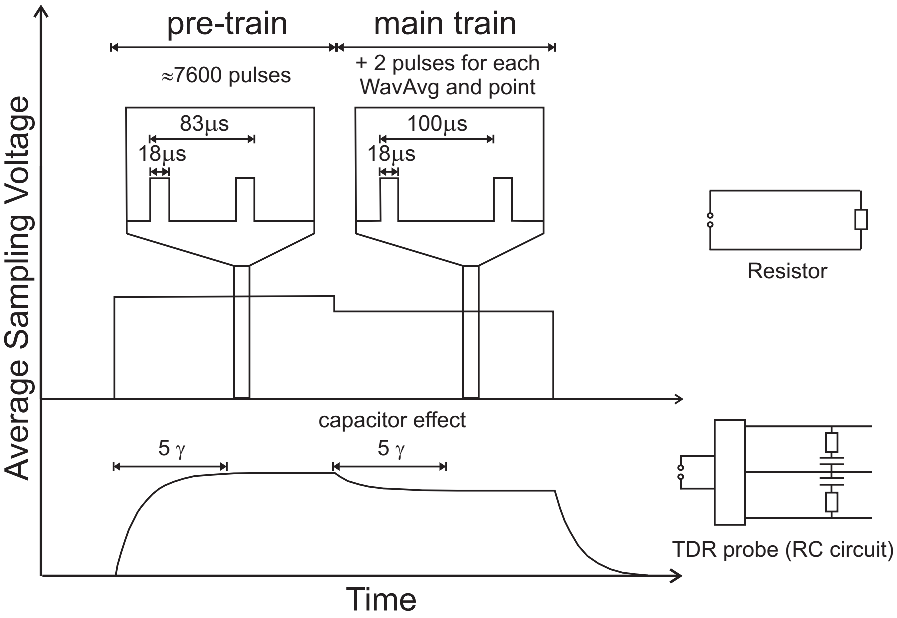

Figure C.8: Schematic illustration of the pulse train when connecting a resistor (top) and a TDR probe or an equivalent RC circuit (bottom). In the primary plot the sampling voltage is averaged over multiple pulse periods (pulse + pause). The individual pulses are illustrated in the two inlets.

pre-train and the main train because of the different pulse width to pulse period ratio, charge transfer occurred again in the capacitor and the average voltage slowly changed to a new level. The time constant (γ in s) of a resistor and capacitor in series is

$$\gamma = (R_{out} + R_L)\, C_{pol} \tag{C.8}$$

where C_{pol} is the capacitance (F). For the cable termination used above, this implies a charge time of 52.5 ms, which corresponded well with the charge time observed with the oscilloscope. The average voltage in the pulse train for a TDR measurement in a saline solution showed qualitatively the same behavior indicating the presence of a capacitance associated with electrode polarization. It is this capacitance that affects the voltage levels of the pulses used by the TDR100 to calculate the TDR waveforms. On first sight, one could argue that a capacitance due to electrode polarization is unlikely for the high frequency typically associated with the bulk electrical conductivity measured with TDR (kHz range). However, the pulse train is not symmetric around zero voltage, and it is the DC component of the pulse train (negative voltage) that causes the electrode polarization. This is also evident from the charge time of the capacitor, which is much longer than a single pulse.

Unfortunately, the exact signal processing procedure is not known for the TDR100, which makes it difficult to predict the impact of the time constant of the RC circuit on the acquired TDR waveforms. If we assume that 1) γ can be as high as 50 ms, 2) complete charging/discharging of the RC circuit takes about 5γ, and 3) the entire main train is used for TDR waveform acquisition, there are about 2500 affected pulses. Since the TDR measurements were clearly erroneous for low WavAvg, we assume that part of the affected pulses is used to construct a TDR measurement. Furthermore, it seems reasonable that a high WavAvg was required to remove or 'dilute' the effect of these first erroneous voltage measurements.

From a TDR cable tester design perspective, there are two possibilities to avoid these capacitive effects. First, it is possible to discard an appropriate part of the main pulse train before starting the acquisition of the actual TDR waveform. Second, the pulse period could be made identical in the pre-train and the main pulse train, which removes the change in average voltage that causes the capacitive effects in the main pulse train. It should be noted that both possibilities assume that the pre-train is not used in TDR waveform acquisition, which is not actually known.

The results presented here have implications for accurate electrical conductivity measurements using the TDR100. It was shown that the standard calibration approach (Eq. C.6) can correct for the incorrect load resistances obtained with a low value WavAvg (Fig. C.3 and Fig. C.9). However, the calibrated values of K_p, R_C and R_0 should be considered as empirical constants in such a case. We suggest to always using sufficiently high WavAvg values and a large number of points in the TDR waveform to assure that most points of the TDR waveform are taken when the main pulse train reached a stable voltage level. It should also be noted that automatic acquisition software typically acquires two separate TDR waveforms for water content and electrical conductivity determination. Because of the simplicity of the analysis procedure, it is tempting to reduce the number of points in a waveform used for electrical conductivity determination. However, reducing the amount of collected data points will result in less accurate electrical conductivity measurements because the first pulses are more affected by the capacitive effects due to electrode polarization.

It is also important not to change the amount of waveform averaging after calibration. For example, a calibration at high WavAvg values (e. g. 128, with the intention to perform a very accurate calibration) and a measurement at low WavAvg values (e. g. 1 or 4, to allow fast acquisition of TDR waveforms) leads to an overestimation of the bulk electrical conductivity (Fig. C.9). On the other hand, when WavAvg used in the field is higher than during calibration (e. g. to compensate for a noisy environment) the bulk electrical conductivity will be underestimated (Fig. C.9). As already mentioned above, relative differences in K_p can approach 5 %. Because of the quasi-linear relationship in the low conductivity range, this can cause errors of 5 % in the determination of the bulk electrical conductivity in low conductive soils (< 0.1 S m^{-1}). The error can be much higher when measuring in saline soils. For a bulk electrical conductivity of 1.4 S m^{-1} and with a cable length of 29.5 m, the error in measured bulk electrical conductivities can amount to 24 %

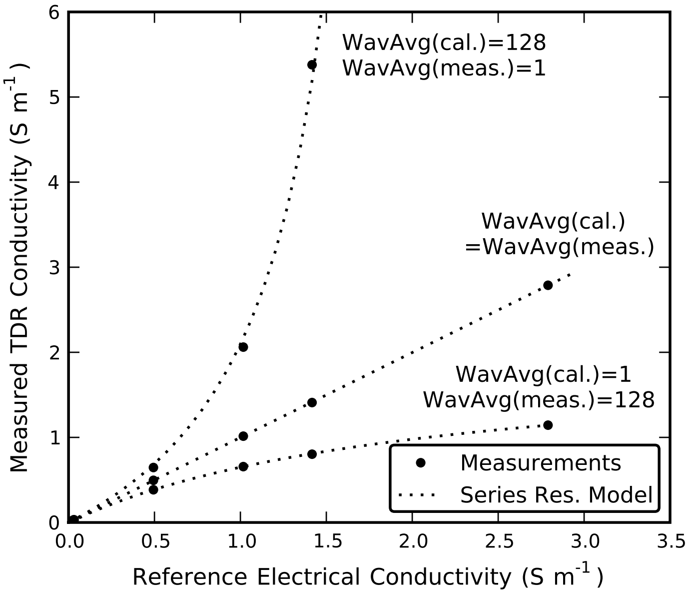

Figure C.9: Measured TDR conductivity calculated using the series resistor model as a function of reference electrical conductivity for different WavAvg values during calibration and measurement.

when calibrating with WavAvg = 128 and measuring with the default of WavAvg = 4, and up to 370 % when using WavAvg = 1 (Fig. C.9). It should be noted that the errors discussed above depend on the capacitance C_{pol}, which itself is a function the electrical conductivity, and the time constant γ of the RC circuit associated with electrode polarization. Therefore, the deviations presented in Fig. C.9 are only valid for the calibration measurements. For a given bulk electrical conductivity, the capacitance due to electrode polarization when a TDR probe is inserted in the soil is not identical to the capacitance associated with a TDR probe inserted in water, for example because of the varying ionic composition. This implies that the time constant γ might be different in soil and that the actual errors reported above are approximate only.

The results presented in this study are based on a single TDR probe and a single TDR100 cable tester. However, we have verified that similar behavior occurs for several other probes designs and TDR100 cable testers. Further, it is possible to identify the same error characteristics in one independent data set (Yu and Drnevich, 2004), in which the TDR100 cable tester was used (compare Fig. C.9 in this study with Figure 3 in Yu and Drnevich, 2004). Therefore, we can exclude that the results presented here are a consequence of using a specific TDR probe design or an individual TDR100 device.

C.4 Conclusions

A capacitance associated with electrode polarization in combination with a change in the pulse period of the pulse train when the TDR100 cable tester starts collecting data points led to an erroneous determination of the reflection coefficient at long times in saline media. This technical issue had a systematic effect on the calibration parameters K_p, R_C, and R_0. With increasing waveform averaging, the reflection coefficient as well as the calibration parameters K_p, R_C, and R_0 approached a maximum value. The maximum values corresponded well with independent estimates. Therefore, we suggest that a high number of WavAvg and a high number of data points provide the physically most reliable data. As a guideline, we propose to use a WavAvg value of at least 16 for accurate electrical conductivity measurements, instead of the default value of 4 currently recommended by the manufacturer. Furthermore, we advise not to reduce the number of data points in TDR waveform below a value of value of 251, even though this is tempting for waveforms that are solely used for bulk electrical conductivity estimation.

We showed that the technical issues reported here might have contributed to the discrepancies between calibrated and directly measured parameters of the series resistor model reported elsewhere. Using the recommendations by Lin et al. (2007; 2008) and Huisman et al. (2008) in addition to an appropriate level of waveform averaging resulted in a data set that was fully consistent with the series resistor model. If TDR100 users are not aware of the capacitive effects introduced by electrode polarization, it can cause significant errors in the determination of the bulk electrical conductivity. In practical applications, this can be 5 % for the low conductivity range (< 0.1 S m^{-1}) and up to 370 % in saline soils (1.4 S m^{-1}) when waveform averaging is changed after calibration. However, these errors are approximate only because the capacitance associated with electrode polarization might be different in soil.

Band / Volume 130
Development of Thin Film Oxygen Transport Membranes on Metallic Supports
Y. Xing (2012), iv, 117 pp.
ISBN: 978-3-89336-765-8

Band / Volume 131
Release of Inorganic Trace Elements from High-Temperature Gasification of Coal
M. Bläsing (2012), XVIII, 145 pp.
ISBN: 978-3-89336-772-6

Band / Volume 132
Rauchgasseitige Korrosion Nickelbasislegierungen für zukünftige 700°C-Dampfkraftwerke
F. Lüttschwager (2012), 145 pp.
ISBN: 978-3-89336-773-3

Band / Volume 133
In-Situ Raman Spectroscopy: A Method to Study and Control the Growth of Microcrystalline Silicon for Thin-Film Solar Cells
S. Muthmann (2012), x, 134 pp.
ISBN: 978-3-89336-774-0

Band / Volume 134
Remote sensing of sun-induced fluorescence for improved modeling of gross primary productivity in a heterogeneous agricultural area
A. Schickling (2012), xvi, 135 pp.
ISBN: 978-3-89336-775-7

Band / Volume 135
Untersuchung der Ladungsträgerkonzentration und -beweglichkeit in mikrokristallinen Siliziumlegierungen mit Hall-Effekt undThermokraft
C. Sellmer (2012), 159 pp.
ISBN: 978-3-89336-778-8

Band / Volume 136
Development of thin film inorganic membranes for oxygen separation
H. J. Moon (2012), XII, 118 pp.
ISBN: 978-3-89336-781-8

Band / Volume 137
Influence of Material and Testing Parameters on the Lifetime of TBC Systems with MCrAlY and NiPtAl Bondcoats
P. Song (2012), V, 126 pp.
ISBN: 978-3-89336-783-2

Band / Volume 138
Strömungsmechanische Modellierung eines Brenngaserzeugungssystems
F. Scharf (2012), vi, 223 pp.
ISBN: 978-3-89336-784-9

Band / Volume 139
Clouds and aerosol in infrared radiative transfer calculations for the analysis of satellite observations
S. Grießbach (2012), viii, 169 pp.
ISBN: 978-3-89336-785-6

Band / Volume 140
Untersuchung zum Thin Film Low Pressure Plasma Spraying (LPPS-TF) Prozess
A. Hospach (2012), 165 pp.
ISBN: 978-3-89336-787-0

Band / Volume 141
Development of thermal spray processes with liquid feedstocks
A. Guignard (2012), 128 pp.
ISBN: 978-3-89336-788-7

Band / Volume 142
Herstellung uranbasierter Keramiken mittels interner Gelierung zur Konversion trivalenter Actinoiden
H. Daniels (2012), 154 pp.
ISBN: 978-3-89336-794-8

Band / Volume 143
Experimental and numerical studies on solute transport in unsaturated heterogeneous porous media under evaporation conditions
M. Bechtold (2012), xviii, 131 pp.
ISBN: 978-3-89336-795-5

Weitere ***Schriften des Verlags im Forschungszentrum Jülich*** unter
http://wwwzb1.fz-juelich.de/verlagextern1/index.asp

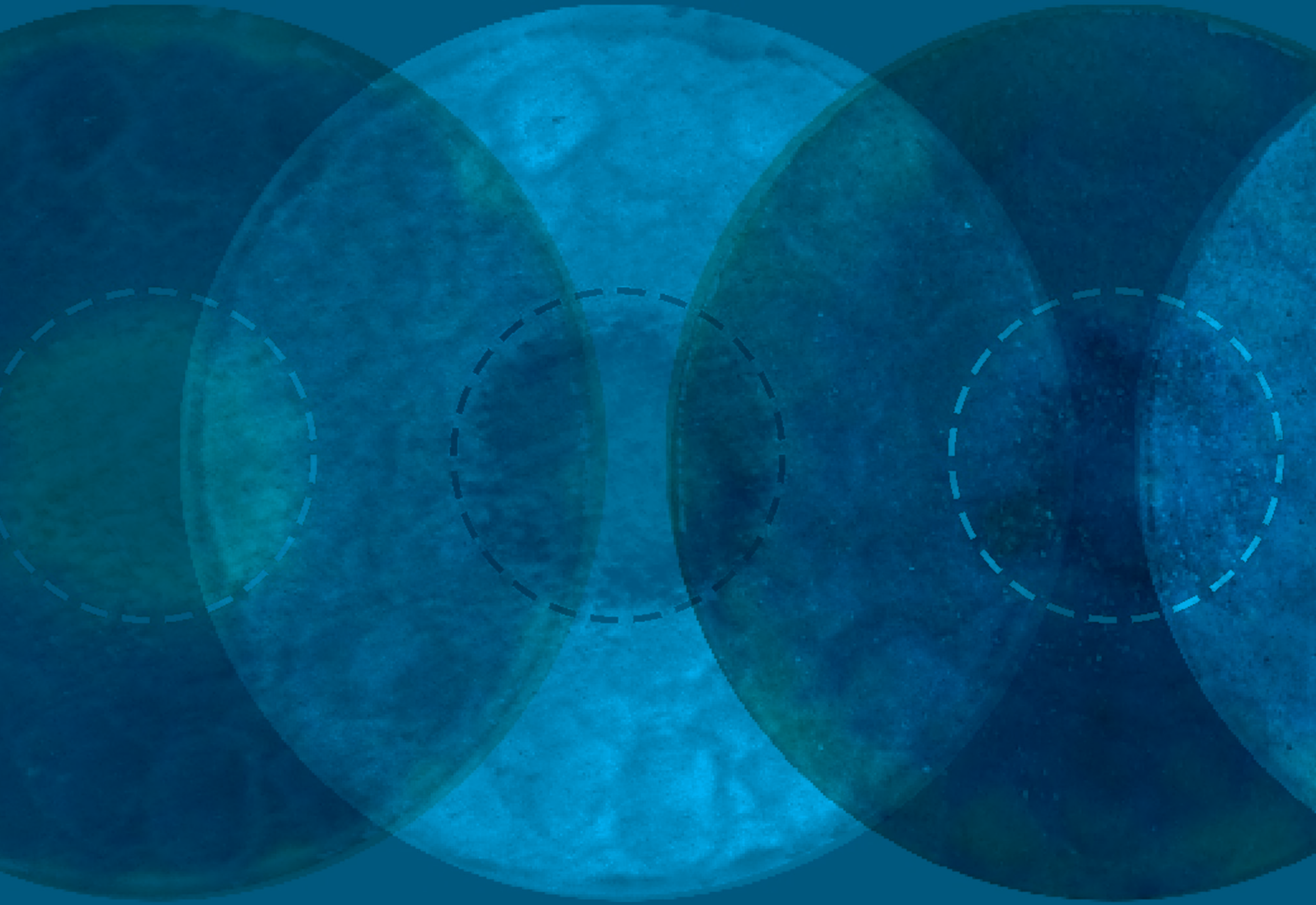

Energie & Umwelt / Energy & Environment
Band / Volume 143
ISBN 978-3-89336-795-5

JÜLICH
FORSCHUNGSZENTRUM